

# Microfluidics-Integrated Surface Acoustic Wave Biosensor

Master of Science thesis in the Master's Programme of Nanotechnology

ASTRID OLIVEFORS



MASTER'S THESIS IN NANOTECHNOLOGY

# Microfluidics-Integrated Surface Acoustic Wave Biosensor

ASTRID OLIVEFORS



**CHALMERS**  
UNIVERSITY OF TECHNOLOGY

Department of Chemistry and Chemical Engineering  
CHALMERS UNIVERSITY OF TECHNOLOGY  
Gothenburg, Sweden 2019

Microfluidics-Integrated Surface Acoustic Wave Biosensor  
ASTRID OLIVEFORS

© ASTRID OLIVEFORS, 2019.

Supervisor: Kiryl Kustanovich, Department of Chemistry and Chemical Engineering

Co-supervisor: Ventsislav Yantchev, Q-Arts Consulting and Department of Chemistry and Chemical Engineering

Examiner: Aldo Jesorka, Department of Chemistry and Chemical Engineering

Master's Thesis 2019

Department of Chemistry and Chemical Engineering

Chalmers University of Technology

SE-412 96 Gothenburg

Telephone +46 (0)31 772 1000

Cover: Schematic visualisation and photograph of a microfluidics-integrated surface acoustic wave sensor.

Typeset in L<sup>A</sup>T<sub>E</sub>X

Printed by Teknologtryck

Gothenburg, Sweden 2019

Microfluidics-Integrated Surface Acoustic Wave Biosensor  
ASTRID OLIVEFORS  
Department of Chemistry and Chemical Engineering  
Chalmers University of Technology

## Abstract

The miniaturisation of analytical devices is a field that has gained much attention during the past decades. To make hand-held devices capable of performing chemical analysis of liquid samples, so-called lab-on-a-chips, is the objective of much of this research. Scaling down analytical platforms will make them cheaper, faster, require less reagent and sample as well as opening for possibilities such as incorporating sensor arrays or to parallelize several sensors in the same device. These devices require sensors to be combined with a microfluidic sample delivery system. Acoustic wave-based sensors are an interesting option for the sensor system. In addition to be able to function as sensors, the acoustic waves can be used to manipulate sample, fluids and particles. However, many existing acoustic wave sensors are severely damped when used with in-liquid samples which impair their sensitivity. By employing shear-horizontal surface acoustic waves (SH-SAW) based sensors, some of the problems caused by damping are circumvented. Employing a SAW resonator as the sensing device improves the sensitivity further. Y-cut X-propagating LiNbO<sub>3</sub> was chosen as the substrate material. In addition to the surface acoustic wave used for sensing this crystal cut supports a different surface acoustic wave, Rayleigh SAW (RSAW). RSAW can be used to manipulate sample, which makes for an interesting option of combining sample preparation with sensing.

A microfluidic-integrated shear-horizontal surface acoustic wave sensor system was designed, fabricated and characterised. It consists of a one-port system with a resonance frequency around 185 MHz. The sensor device has been used to detect changes in the viscoelastic properties of the sample. Mass deposition on the sensor was also detected, by using a supported lipid bilayer (SLB) which functions as a model system for biological membranes.

Keywords: surface acoustic wave, microfluidic, SH-SAW, sensor, integration, PDMS, LiNbO<sub>3</sub>, bio-chemical



## Acknowledgements

First of all, I would like to thank my supervisor Kiryl Kustanovich for all help, in the lab and with the report, even when being very busy. Great thanks to my examiner Prof. Aldo Jesorka for giving me the opportunity to do my thesis project in this group, and for teaching me so many things. I would also like to thank my co-supervisor Dr. Ventsislav Yantchev. Furthermore, thank you to everyone in the Biophysical Technology Lab, for all help and company. I would also like to thank the other master's thesis students who passed through the corner room in the lab in MC2, you were all great office mates. Finally, a big thank you to my family and to my friends (ingen nämnd, ingen glömd) for making these years at Chalmers so much fun.

Astrid Olivefors, Gothenburg, June 2019



# Contents

<b>List of Figures</b>	<b>xi</b>
<b>List of Tables</b>	<b>xv</b>
<b>1 Introduction</b>	<b>1</b>
<b>2 Elastic Waves in Solids</b>	<b>5</b>
2.1 Fundamental Wave Physics . . . . .	6
2.2 Piezoelectricity . . . . .	6
2.2.1 The electromechanical coupling coefficient . . . . .	7
2.3 Interdigital transducers . . . . .	8
2.4 Quality factor . . . . .	9
2.5 Bandwidth . . . . .	9
2.6 Piezoelectric substrate materials . . . . .	10
2.7 Different types of acoustic waves . . . . .	11
2.7.1 Bulk acoustic waves (BAW) . . . . .	11
2.7.2 Surface acoustic waves (SAW) . . . . .	12
2.7.2.1 Rayleigh waves . . . . .	13
2.7.2.2 SH-SAW . . . . .	13
2.7.2.3 Love waves . . . . .	14
2.7.2.4 Leaky SAW . . . . .	14
<b>3 Microfluidics</b>	<b>15</b>
3.1 Scaling laws . . . . .	15
3.2 Equations governing the fluid flow . . . . .	17
3.2.1 Navier-Stokes equations . . . . .	17
3.2.2 Hagen-Poiseuille equation . . . . .	19
3.2.3 Hagen-Poiseuille equation and Ohm's law . . . . .	19
3.2.4 Mass transport . . . . .	20
3.3 Applications . . . . .	21
3.3.1 Lab-on-a-chip . . . . .	22
3.3.2 Mixers . . . . .	23
3.3.3 Particle gates . . . . .	24
<b>4 Sensors</b>	<b>27</b>
4.1 Overview . . . . .	27
4.2 Noise . . . . .	28

4.3	Biosensors . . . . .	29
4.4	Surface acoustic wave sensors . . . . .	29
4.4.1	Different SAW sensor configurations . . . . .	30
4.4.1.1	Delay line . . . . .	30
4.4.1.2	SAW Resonator . . . . .	31
4.4.1.3	One-port and two-port SAW resonators . . . . .	31
4.4.2	Detection mechanisms . . . . .	31
4.4.2.1	Mass loading . . . . .	31
4.4.2.2	Viscoelastic properties . . . . .	33
4.4.3	Read-outs . . . . .	33
<b>5</b>	<b>Method</b>	<b>35</b>
5.1	Design . . . . .	36
5.1.1	Simulation . . . . .	36
5.1.2	Drawing . . . . .	36
5.2	Device fabrication . . . . .	37
5.2.1	Lift-off lithography . . . . .	38
5.2.2	Photolithography . . . . .	41
5.3	Soft lithography . . . . .	43
5.3.1	Bonding . . . . .	44
5.3.1.1	Plasma bonding . . . . .	44
5.3.1.2	Adhesive bonding . . . . .	45
5.4	Lipid membrane . . . . .	46
5.4.1	Background . . . . .	47
5.4.2	Lipid prep . . . . .	48
5.5	Sensor characterisation . . . . .	48
<b>6</b>	<b>Results and Discussion</b>	<b>53</b>
6.1	Results . . . . .	53
6.1.1	Sensors . . . . .	53
6.1.1.1	Results of experiments: Sensor without LEC . . . . .	56
6.1.1.2	Results of experiments: Sensor with LEC . . . . .	59
6.1.2	Adhesive bonding . . . . .	62
6.2	Discussion . . . . .	64
6.2.1	Sensors . . . . .	64
6.2.2	Adhesive bonding . . . . .	66
<b>7</b>	<b>Conclusion and Outlook</b>	<b>67</b>
	<b>Bibliography</b>	<b>69</b>
	<b>A Paper I</b>	<b>I</b>

# List of Figures

1.1	A Rochelle salt (potassium sodium tartrate tetrahydrate) crystal, another naturally occurring piezoelectric crystal, in a holder to measure its piezoelectric properties. Image from (with permission) . . . . .	1
1.2	A typical delay line surface acoustic wave device. . . . .	2
1.3	Two quartz crystal resonators (QCMs). Image from (CC-BY-3.0). . . . .	3
2.1	Schematic of a sinusoidal wave with the wave length $\lambda$ , amplitude $A$ , and period $T$ . . . . .	6
2.2	(a) The symmetry axis in an unstressed crystal, where the arrows represents the dipole moments in the crystal. The total dipole moment in each crystal cell is zero. (b) When a stress is applied, a polarization $\mathbf{P}$ is developed and the sum of the dipole moments is no longer zero. . . . .	7
2.3	A diagram of an IDT. The <i>aperture</i> is the acoustic aperture of the IDT, $\mathbf{d}$ is the grating pitch, $2\mathbf{d}$ the period, $\mathbf{w}$ the width of the electrode, and $\mathbf{g}$ the electrode gap. . . . .	8
2.4	Schematic of longitudinal and shear bulk acoustic waves. . . . .	12
2.5	Schematic of several different surface acoustic waves. . . . .	13
3.1	Six microchemostats in parallel, via . . . . .	15
3.2	The geometric scaling of a cube. The side length of the larger cube is $2\ell$ , twice as long as the side length of the smaller cube $\ell$ . It can be seen that the larger cube has a bottom area which is four times as large as the bottom area of the smaller cube, and the larger volume is eight times larger than that of the smaller cube. . . . .	16
3.3	The difference between turbulent and laminar flow regimes. The bottom image illustrates the laminar flow regime. The top image illustrates a flow that starts out as laminar and becomes turbulent. The regime between the fully laminar and the fully turbulent flows is called transitional. . . . .	18
3.4	An electrical circuit (a) and its fluidic equivalent (b). The main difference between them is how the resistors are constructed. . . . .	20
3.5	Some examples of microfluidic mixers. Passive mixers a-c: a. diffusive mixer, b. zigzag mixer, c. herringbone mixer. Active mixers d-e: d. pulsed pressure mixer, e. mixing by acoustic streaming. . . . .	23
3.6	Rayleigh SAW used to manipulate the fluid flow or particles in a microfluidic channels by acoustic streaming . . . . .	24

---

4.1	Schematic of the general components of a sensor. . . . .	27
4.2	Image of a typical delay line SAW sensor system . . . . .	30
4.3	An illustration of the principle mass loading on a delay line SAW-sensor. To top image shows a (functionalised) lipid bilayer deposited on the SAW-device with functionalised nanoparticles binding to the lipid bilayer. The bottom image shows how the SAW is affected by the mass loading caused by the deposited materials: the blue wave is before mass deposition, and the red wave after the mass deposition where the frequency and phase of the wave has been shifted. . . . .	32
4.4	Incident and reflected signals and scattering parameters in linear two-port circuit. . . . .	33
5.1	The steps in the complete SAW device fabrication process. . . . .	35
5.2	A COMSOL simulation image of shear displacement.a) LSAW on a free surface, b) SH-SAW on a surface guided by a periodic gold grating. . . . .	36
5.3	A portion of an AutoCAD drawing of particle concentration devices placed on a wafer, including all parts of the devices. The different colours denotes different layers in the drawing, and also different parts of the design. . . . .	37
5.4	The process steps in a standard lift-off fabrication process. . . . .	38
5.5	Schematic of the lift-off lithography based process . . . . .	39
5.6	Schematic of the photolithography process and, in the last three steps, a rough outline of the fabrication of microfluidic PDMS structures. . . . .	42
5.7	PDMS chemical structure and oxygen plasma bonding chemistry . . . . .	44
5.8	Schematic of lipids, vesicles and lipid bilayers. . . . .	46
5.9	Schematic and photograph of the finished device. . . . .	49
5.10	Photograph of the measurement setup. The setup is placed under a fluorescence microscope on a temperature controlled stage. The SAW sensor device is connected to the VNA by Picoprobes. . . . .	50
6.1	Schematic of a one-port SAR microfluidics-integrated device, from . . . . .	53
6.2	FEM simulation of the SAW shear displacement on different substrates. Darker colours indicate larger displacements, with red and blue for positive and negative displacements respectively. <b>(a)</b> LSAW on a free surface on $\text{LiNbO}_3$ , <b>(b)</b> SH-SAW guided by a periodic Au grating on $\text{LiNbO}_3$ . . . . .	54
6.3	Optical microscopy image of the SAR sensor without the lateral energy confinement design. The SAR sensor is made out of a SAW resonator which has been bonded to the PDMS sample delivery system. The PDMS system has two containers for sample over the resonator and an air cavity about the IDT to protect it from any liquid . . . . .	55
6.4	Simulations of the normalized displacement distributions of SH-SAW at <b>(a)</b> resonance and <b>(b)</b> anti-resonance for $m=0.5$ . A schematic illustrating where the microfluidic cavities are placed in relation to the the SH-SAW displacements is placed at the bottom of the graph. . . . .	55

6.5	Schematic combining a FEM simulation of the displacement magnitude of the SH-SAW resonator at resonance and one-half of the SAR-sensor cross section. . . . .	56
6.6	Optical microscopy image of SAR sensor with <i>lateral energy confinement</i> (LEC) reflector topology. The PDMS sample delivery system is not pictured, but the air cavity is outlined in red and the containers are outlined in blue. . . . .	56
6.7	Simulations of the normalised SH-SAW displacements at <b>(a)</b> resonance and <b>(b)</b> anti-resonance for $m=0.4$ , i.e. in the LEC overlaid with the layout of the SAR sensor. . . . .	57
6.8	The top section shows a schematic of part of the delivery system of the SAR-sensor, while the bottom section shows how the metallization ratio varies over the device . . . . .	58
6.9	The phase (dashed graphs) and the conductance (solid graphs) of the SAR-sensor when the microfluidic containers are filled with air (black graphs) or MilliQ-water (MQW) (red graphs). . . . .	59
6.10	Schematic of the assay consisting of a supported lipid bilayer with biotin and neutravidin-coated nanoparticles . . . . .	59
6.11	<b>(a)-(b)</b> Fluorescent microscopy images (ATTO-488) of the sensor loaded with MLV solution before washing <b>(a)</b> and after washing <b>(b)</b> . The fluorescence after washing is weak but its presence indicates that the SLB has spread on the sensor surface. <b>(c)-(d)</b> Fluorescence microscopy images (Nile red) of the sensor loaded with NP solution before washing <b>(c)</b> and after washing <b>(d)</b> , indicating the presence of NPs. The scale bar is 100 $\mu\text{m}$ . . . . .	60
6.12	The performance of the SAR-sensor with LEC under a water load. The admittance (conductance) (red) is measured at resonance and the resistance (blue) at anti-resonance. . . . .	61
6.13	The performance of the SAR-sensor with LEC under a viscous load. . . . .	62
6.14	The time-resolved response of the SAR-sensor with LEC for varying viscous loads. The different $\rho\eta$ values were obtained by varying the glycerol content in MilliQ. Frequency shifts between the different loads are indicated in red. . . . .	63
6.15	Time-resolved responses of frequency shift <b>(a)</b> and the peak conductance magnitude shift <b>(b)</b> for the SAR-sensor with LEC for the SLB-deposition and the SLB-NP biotin-neutravidin affinity-assay reaction. . . . .	64
6.16	The time-resolved sensor response of when the SLB is exposed to $\text{Ca}^{2+}$ . <b>(a)</b> the frequency shift and <b>(b)</b> peak conductance magnitude shift. . . . .	64



# List of Tables

6.1	SAR sensitivity for different viscous loads, achieved by varying the sucrose-PBS concentrations. . . . .	57
6.2	SAR sensitivity to deposition of an SLB and NPs. . . . .	60
6.3	SAR device sensitivity for different loads of SLB and NPs. Note that the buffer used here was HEPES. . . . .	60
6.4	SAR sensitivity for different viscous loads for the SAR-sensor with LEC . . . . .	61
6.5	Mass and conductance sensitivity for different loads in the SLB-NP biotin-neutravidin affinity assay. Note that the buffer used was HEPES, not PBS. . . . .	62
6.6	The sensitivity of the SAR sensor with and without LEC. . . . .	65
6.7	SAR-sensor sensitivity for SLB-NPs reactions in HEPES . . . . .	65



# 1

## Introduction

Piezoelectric crystals, such as quartz, topaz, and sucrose, are a class of materials which have found applications in a variety of technological fields, due to the special properties of piezoelectric materials: when subjected to a mechanical stress, the electric polarization in these materials change, and vice versa [2]. Synthetic piezoelectric crystals, such as aluminium nitride, lithium niobate, lithium tantalate, and gallium phosphate, have higher degrees of piezoelectricity than the naturally occurring crystals [3]. A main application for this type of materials has been in filters in the radio frequency (RF) range [4]. These filters are often based on surface acoustic waves (SAW), which are excited on the surface of the piezoelectric substrate by an applied electric voltage. SAW are confined on, or close to, the surface of the substrate, with the majority of the wave's energy concentrated within a few wavelengths into the material [4]. One advantage of using RF SAW filters is that the high frequency of the SAW makes it possible to drastically reduce the size of the filters, making them ideal to use in portable applications as well as lowering the cost of these devices.

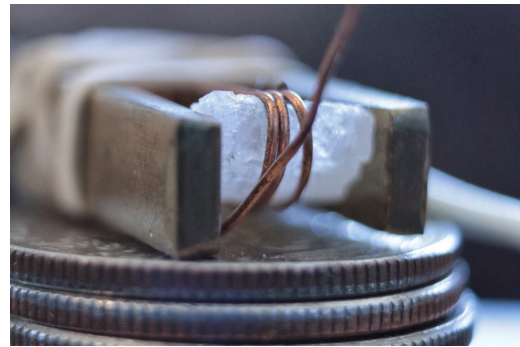


**Figure 1.1:** A Rochelle salt (*potassium sodium tartrate tetrahydrate*) crystal, another naturally occurring piezoelectric crystal, in a holder to measure its piezoelectric properties. Image from [1]

SAW devices typically function in the following way, an electric input signal is converted to a surface acoustic wave by an interdigital transducer (IDT) on the piezoelectric substrate. The wave then propagates on the substrate to the receiving IDT, where it is converted to an electric output signal [4]. In a SAW filter, the unfiltered input signal reaches the input IDT, where only the desired parts of the signal are converted into SAW, which then travels to the output IDT. For this type of SAW device, what is valued is the reduction of off-resonance signals, as well as low transfer losses of desired band resonance signals. Additionally, there should be no external influence on the piezoelectric substrate in SAW filters as to limit the effect of the environment on the filter.

Another type of SAW devices are SAW resonators. They operate on the resonant frequency of the device. The factor which gives information on how underdamped the resonator is as well as describing the relationship between the resonant frequency

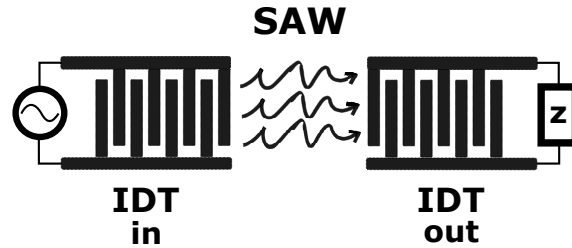


**Figure 1.2:** A typical delay line surface acoustic wave device.

and the bandwidth of the device is the quality factor (Q-factor). Most importantly, the Q-factor is an indication on how well the system retain energy: a high Q-value means only very little, or no, energy is lost, while a low Q-value indicates that more energy is lost in the system. Naturally, a high Q-value is desired for the absolute majority of SAW devices.

In filters it is important to limit the effect of the external environment on the filter. However, how the external environment affect the propagation of the SAW can also be interesting. That information can be used for analytical purposes, as is done in the case of SAW sensors. Changes in SAW frequencies and other signal characteristics resulting from the interactions of the analyte with the sensor are measured and analysed, forming the basis of a sensor.

It is possible to use much of the SAW RF filter technology for sensing applications. Just as is the case for SAW filters, a high transfer efficiency is still desired in SAW sensors, but the losses are significant and the external interaction are necessary for the device to function.

The phenomenon that is most commonly used in SAW sensors to detect analytes is mass loading, where the deposition of some mass on the surface of the sensors damps the SAW and causes a shift in frequency, phase, or amplitude which then can be detected [5,6]. This is also known as gravimetric sensing. The surface of the sensor can be functionalised to bind to an analyte of interest. This opens up for the possibility of using SAW sensors in a variety of fields, including in life-science for biological or bio-chemical measurements.

The most important practical application of piezoelectric-based acoustic-wave sensors in life science is still the quartz crystal microbalance (QCM). QCMs measure the deposition of mass on its surface based on the frequency-shift caused by the mass deposition, using a type of bulk acoustic waves. It can be used under vacuum, in gas or liquid and has found many laboratory applications. The QCM operates as a simple large area resonator on low frequencies, which might be problematic for some types of measurements, as the large area means the sensor requires large sample quantities to accurately measure. In addition, the large size of the low frequency resonator makes integration difficult.

SAW sensors, can be made smaller, on account of the high frequency they operate at

which also opens the possibility of creating sensor arrays, and devices that integrate sample preparation with sensing, such as lab-on-a-chips.



**Figure 1.3:** *Two quartz crystal resonators (QCMs). Image from [7] (CC-BY-3.0).*

Although SAW sensors have been in existence for decades, they have only found limited commercial application due to issues arising from complicated fabrication routes, poor performance, and lack of integration options. In this thesis, some of these issues are addressed. The fabrication processes and materials used are already commercially viable, due to their use in the semiconductor industry, and the SAW sensor can easily be integrated with a soft lithography PDMS device for sample delivery and preparation, forming a lab-on-a-chip device.

Within the frame of this project, a high quality one-port SAW in-liquid sensor was developed and fabricated. It has a sensitivity close to the theoretical sensitivity limit. The complete sensor system has a small footprint and requires only very small amounts of sample. On account of the straightforward fabrication process, in which several well-established methods are used, the sensor is mass production ready. The one-port electronic interface is easy to integrate in other structures. In addition, it is more robust for measurements than a two-port setup and by using a one-port setup it is also possible to eliminate some of the signal processing that is often required when using a two-port setup [8]. As mentioned earlier, this sensor is also easily integrated into a microfluidic sample delivery system.

This thesis is structured in the following way, the theoretical background for SAWs is introduced in Chapter 2, for the sample delivery system and microfluidics in Chapter 3, and for sensors in Chapter 4. Details on how the devices were designed, fabricated, and characterised are presented in Chapter 5. The outcome of the sensor characterisation is found in Chapter 6 and the conclusions from this, together with a brief outlook on further research are summarised in Chapter 7.



# 2

## Elastic Waves in Solids

Acoustic waves are mechanical waves that propagate in elastic solids and are also known as elastic waves [3]. They might propagate in the bulk of the material, along the surface, or by in mixture of the two [9]. The energy of the surface acoustic waves (SAWs) is strongly confined close to the surface of the material [4, 6, 9, 10], unlike that of the bulk acoustic waves (BAWs). The confinement of the energy in SAW have made them useful in applications in several different fields.

IDTs are made from metal thin-films and are therefore comparatively easy to fabricate using already existing techniques from the semi-conductor industry. SAW devices have subsequently found applications in a range of different areas, including telecommunications [4, 11], microfluidics [12], and as sensors [5, 13, 14].

To use SAW sensor in biochemical applications, the waves' behaviour in fluid environment need to be taken into account. Some SAW modes will radiate into the liquid, making it difficult to use them for sensing. For that reason, transverse-shear SAW modes need to be used for in-liquid SAW sensors [8].

The energy of the SAW are concentrated on the substrate surface, making them sensitive to perturbations on the surface. This makes them ideal to use in gravimetric sensing applications. SAW sensors are highly sensitive and can be used to detect small quantities of analyte (even in low-concentration solutions). In addition, SAW sensors are used to label-free detection, eliminating the need for chemical labels in the sample.

## 2.1 Fundamental Wave Physics

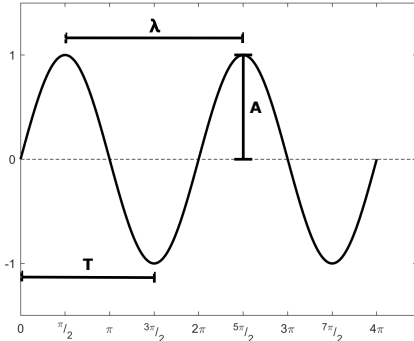


**Figure 2.1:** Schematic of a sinusoidal wave with the wave length  $\lambda$ , amplitude  $A$ , and period  $T$ .

Some fundamental definitions are useful when dealing with waves (these are found in, for instance in [15]). Some of these definitions are illustrated in Figure 2.1. The *wavelength*  $\lambda$  is the distance between, for instance, two maxima in the same wave. The *amplitude*  $A$  is here defined as the peak amplitude, the amplitude above and below a reference value. The *frequency*  $f$  (or  $\nu$ ) is defined as  $f = \frac{v}{\lambda}$ , with  $v$  as the velocity, or as  $f = \frac{1}{T}$ , with  $T$  as the *period* or the time it takes for a full cycle of oscillation to occur. The *angular frequency*  $\omega$  is the angular displacement in radians per time unit  $\omega = 2\pi f = \frac{2\pi}{T}$ . The (angular) *wavenumber*  $k$  (or  $\beta$ ) is the spatial frequency of the wave

and defined as  $k = \frac{2\pi}{\lambda}$ .

The propagation of waves in a medium can be affected by the medium. Typically, the velocity of a wave in a medium depend on the frequency of the frequency of a wave [15]. This dependency is called *dispersion* and the medium a *dispersive medium* [15].

In the absolute majority of the time there is not just one wave travelling through space, but a group of waves which superposition into one modulated wave. The *phase velocity* of this modulated wave is defined as  $v = \frac{\omega}{k}$  [15, 16], because the points on the modulated wave with the same phase travels with this velocity [16]. The overall velocity of the modulation of waves, the group of waves, is called *group velocity* and defined as  $v_g = \frac{d\omega}{dk}$  [15, 16]. The phase and group velocities are typically the same for non-dispersive waves [16].

## 2.2 Piezoelectricity

SAW are excited on the substrate surface as a result of piezoelectricity: when subjected to a mechanical stress, the electric polarization of the materials change and vice versa<sup>1</sup> [2, 6, 9]. This effect is utilised by sending an electric signal to the IDTs on the piezoelectric surface, which then causes a mechanical stress on the substrate, which in turn produce surface acoustic waves.

<sup>1</sup>Technically, the (direct) piezoelectric effect is the change from mechanical to electrical quantities, the other way around (electric signal to mechanical deformation) is known as the indirect piezoelectric effect [17].

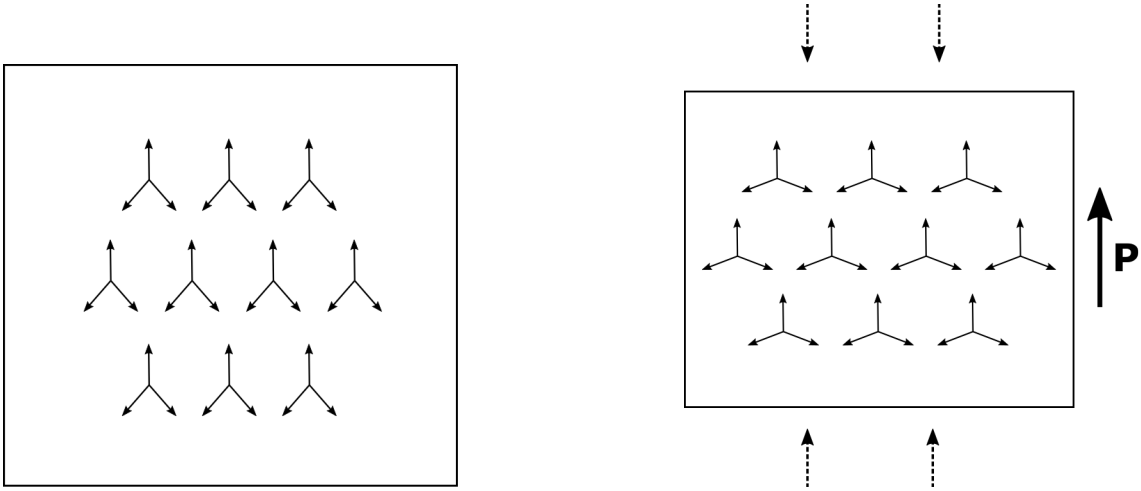


**Figure 2.2:** (a) The symmetry axis in an unstressed crystal, where the arrows represents the dipole moments in the crystal. The total dipole moment in each crystal cell is zero. (b) When a stress is applied, a polarization  $\mathbf{P}$  is developed and the sum of the dipole moments is no longer zero.

The crystal structure of a material is an important factor that determines whether a material is piezoelectric or not. If the crystal lacks an inversion centre (centre of symmetry), an applied strain will change the charge distribution within the crystal in such a way that there will be a net dipole moment in the crystal as a whole [6, 18]. This process is illustrated in Figure 2.2.

The mathematical description of piezoelectricity is presented in the following Equation 2.1 and 2.2, which both are from [9]. In these equations,  $\vec{D}$  is the electric flux density,  $\vec{S}$  the strain,  $\vec{E}$  the electric field, and  $\vec{T}$  the stress.  $\vec{e}$  is the piezoelectric constant,  $\vec{\epsilon}$  is the dielectric constant and  $\vec{c}$  is the stiffness constant.

$$\vec{D} = \vec{e}\vec{S} + \vec{\epsilon}\vec{E}, \quad (2.1)$$

and

$$\vec{T} = \vec{c}^E\vec{S} - \vec{e}^t\vec{E}. \quad (2.2)$$

The superscripts S and E indicates that the constants are determined under constant strain or under a constant electric field. The superscript  $t$  over the piezoelectric constant is an indicator that it is the transpose of the piezoelectric constant matrix.  $\vec{D}$  will in this case be 0, as Equation 2.1 is constant.

### 2.2.1 The electromechanical coupling coefficient

The degree of conversion between mechanical and electrical energy, i.e. the degree of piezoelectricity, can be characterised by the electromechanical coupling factor

$K^2$  [4]. This property can be defined either for the substrate material on its own or for the device as a whole. The difference between these definitions lie in whether  $K^2$  is defined using the wave velocities on free surfaces (the substrate material) or the wave velocities on metallized surfaces (the device). If the SAW velocities are adequately smaller than the BAW velocities, the electromechanical coupling factor can be expressed in the following equation from [9]:

$$K^2 = \frac{V_{Sf}^2 - V_{Sm}^2}{V_{Sf}^2} \cong 2 \frac{V_{Sf} - V_{Sm}}{V_{Sf}} \equiv 2 \frac{\Delta V}{V}. \quad (2.3)$$

$V$  denotes SAW velocity, the subscripts denotes whether the velocity is from the wave on the free surface ( $Sf$ ) or the metallized surface ( $Sm$ ). The expression in Equation 2.3 is valid for Rayleigh SAW.

### 2.3 Interdigital transducers

SAW are generated by sending electrical signals to an interdigital transducer (IDT) on top the piezoelectric substrate material. The IDT is made up from metal thin film electrodes on the substrate [19]. The IDTs can be designed to generate SAW in specific patterns suited for different applications.

IDTs consist of several comb-like structures fabricated from thin metal films on top of the substrate [9, 19]. As a result of the piezoelectric effect, when electric voltage of a certain frequency is applied to the IDT, the resulting electric field will cause mechanical strain on the substrate [19]. The mechanical strain will in turn cause waves to spread on the surface.

The IDTs are made up from several metallic strips that are attached to perpendicular metallic strips (busbars), as is illustrated in Figure 2.3. The width of the metallic strips ( $w$ ) as well as the gap between them (the *electrode gap*  $g$ ) are factors affecting the resulting wave. Two metallic strips attached to opposite busbars together form a *finger-pair*. [19]

The IDT functions most efficiently when the *period*  $2d$  is matched to the desired wave frequency  $\lambda$ . This will happen when the IDT is excited at the (synchronous) frequency  $f_0 = \frac{v_0}{d}$ , where  $v_0$  is the velocity of the SAW [6]. The geometry of the IDT also determines the acoustic aperture of the device [9, 20], see Figure 2.3. The acoustic aperture is the area where the waves can propagate. This is where potential resonances can happen, such as overtones and spurious responses. The apertures can be designed to suppress these by breaking up the symmetry in the aperture [21].

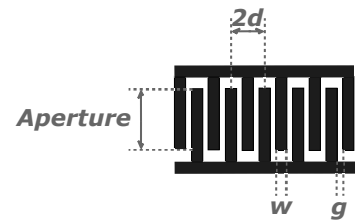


**Figure 2.3:** A diagram of an IDT. The aperture is the acoustic aperture of the IDT,  $d$  is the grating pitch,  $2d$  the period,  $w$  the width of the electrode, and  $g$  the electrode gap.

IDTs can be designed to function as for instance filters, possibly in delay-line configurations or as either one-port or two-port resonators.

The most important factors determining the IDT characteristics are the finger geometry in the period, the overall number of finger pairs, and the substrate material [9].

The fabrication of IDTs is mainly done using well established techniques commonly used in MEMS (microelectromechanical systems) industries [19].

## 2.4 Quality factor

The quality factor  $Q$  of a resonator is defined as the ratio between the stored and dissipated energy for one wave cycle [9, 15, 20]. It is one of the most important variables used to characterise resonators [20]. The definition can be expressed in the following way [20]:

$$Q = \omega \frac{\text{Energy stored}}{\text{Power dissipated per one cycle}}. \quad (2.4)$$

## 2.5 Bandwidth

The bandwidth of a device is the range of frequencies the device will work on [22]. SAW devices can be constructed for different bandwidths, depending on the intended use of the device.

A narrow bandwidth is desired for SAW devices such as filters, where it is desired to only let a narrow range of frequencies pass. This is achieved by use of an IDT which confines the majority of the wave energy close to the wave source. Reflectors can be placed on either side of the IDT to confine the energy further. These types of SAW devices are typically quite bulky, as the IDTs required needs many electrodes to confine the wave energy.

SAW devices such as sensors are constructed from IDTs with wide bandwidths. The energy in these types of devices is not as concentrated in the IDT as is the case for narrowband devices, but spread out from the IDT. Similar to what is done in filters, it is possible to confine the energy by placing reflectors on either side of the IDT. In sensor devices the spreading energy is confined over a larger area to be used as the sensor area. This application also requires substrate materials with a high electromechanical coupling factor.

## 2.6 Piezoelectric substrate materials

As was described in Section 2.2, the substrates used for SAW devices need to be piezoelectric. As all piezoelectric materials are anisotropic, the material properties are not only dependent on the material itself but also on the cut angle and the SAW propagation direction [3, 9]. Different crystal cuts (lattice directions) favour different waves [3, 4]. Commonly used substrate materials include quartz, LiTaO<sub>3</sub>, and LiNbO<sub>3</sub> [23].

Three important material parameters for designing SAW devices are the SAW velocity  $v$ ,  $K^2$ , and the temperature stability [4, 9]. The temperature stability is often characterised using the temperature coefficient of frequency (TCF) [4, 9, 19].

The SAW velocity ( $v$ ) determines the resonant frequency of the device [9]. The SAW  $v$  is dependent on the elastic properties and density of the substrate material. The velocity  $v$  is also affected by temperature, since the material properties are dependent on the temperature [4].

The electromechanical coupling factor is, as was mentioned above, a measure of how efficient the material is at converting between electrical and mechanical energy [4]. Depending on the intended application of the SAW device, materials with different  $K^2$  are desired. Materials with a high electromechanical coupling factor are very sensitive to mechanical perturbations, making them ideal to be used in sensor applications. However, the high degree of piezoelectricity these material possesses also make them harder to use and fabricate compared to materials with lower electromechanical coupling factors. Materials with high  $K^2$  are also more sensitive to temperature than materials with lower  $K^2$ , often causing them to have worse TCF values [9]. For SAW devices other than sensors, materials with low  $K^2$  are often used, since the higher sensitivity to perturbations is not needed [4].

One specific crystal cut which is often used in SAW devices is the Y-cut X-propagating LiNbO<sub>3</sub>. It is a synthetic ferroelectric crystal that possesses a very large dielectric constant and piezoelectricity ( $K^2$ ) [9]. In addition to this, it also has a large pyroelectricity and electro-optic effect [9].  $K^2$  for Y-cut LiNbO<sub>3</sub> can for some rotation angles be as high as 25 %. The high degree of piezoelectricity of the LiNbO<sub>3</sub> makes it very sensitive towards variations on its surface. For the same rotational angle, the propagation velocity of leaky SAW is about 4200 m/s. The temperature stability on this specific crystal cut, measured as the temperature coefficient of velocity (TCV)<sup>2</sup>, is about  $-75$  ppm/°C [9]. It is a well-studied material and many different cuts of LiNbO<sub>3</sub> are commercially available [20].

---

<sup>2</sup> TCV and TCF are different parameters that both measures the temperature stability of different materials. TCF can be calculated from TCV, see [9].

## 2.7 Different types of acoustic waves

As already mentioned, acoustic waves need some kind of medium to propagate in. Different acoustic waves can propagate in different ways. There is no clear difference in the physics describing the acoustic waves propagating in the bulk or on the surface of a material. Depending on their propagation, different types of acoustic waves can exist in elastic solids. Some of these types will be outlined in this section.

### 2.7.1 Bulk acoustic waves (BAW)

Bulk acoustic waves (BAW) are a class of acoustic elastic waves propagating in solids [6, 9]. BAW are thought to propagate in bulk solids, which have no boundaries [6].

There are two main classes of BAW, depending on their polarization: longitudinal BAW and transverse, or shear, BAW. Longitudinal BAW (L-BAW), illustrated in Figure 2.4a, have a polarization which is parallel to the propagation direction [9]. Shear BAW, as are illustrated in Figure 2.4b and 2.4c, have a polarization perpendicular to the propagation direction [9]. This group can be further categorised into shear vertical BAW (SV-BAW), illustrated in Figure 2.4b, and shear horizontal BAW (SH-BAW), Figure 2.4c.

The phase velocities of the longitudinal and shear waves are different for the two different polarizations and are also dependent on the material the waves are propagating in. The phase velocities are calculated according to [9].

$$V_l = \sqrt{\frac{c_{11}}{\rho}},$$

$$V_s = \sqrt{\frac{c_{44}}{\rho}},$$

With  $\rho$  being the density of the material and  $c_{ij}$  is the stiffness constant of the piezoelectric material.  $V_l$  and  $V_s$  are the stiffened and the non-stiffened velocities respectively.

For each propagation direction, there are three different acoustic waves: one *quasi-longitudinal* and two *quasi-shear* [18]. The anisotropy in the piezoelectric material causes their propagation direction not to be purely longitudinal or purely shear [18]. The three quasi-waves have different velocities, with the quasi-longitudinal as the fastest. The quasi-shear waves are further classified as fast-shear or slow-shear depending on their velocities [20]. The different quasi-waves couple together and form new waves. If these are in the proximity of a surface, this will give rise to surface acoustic waves.

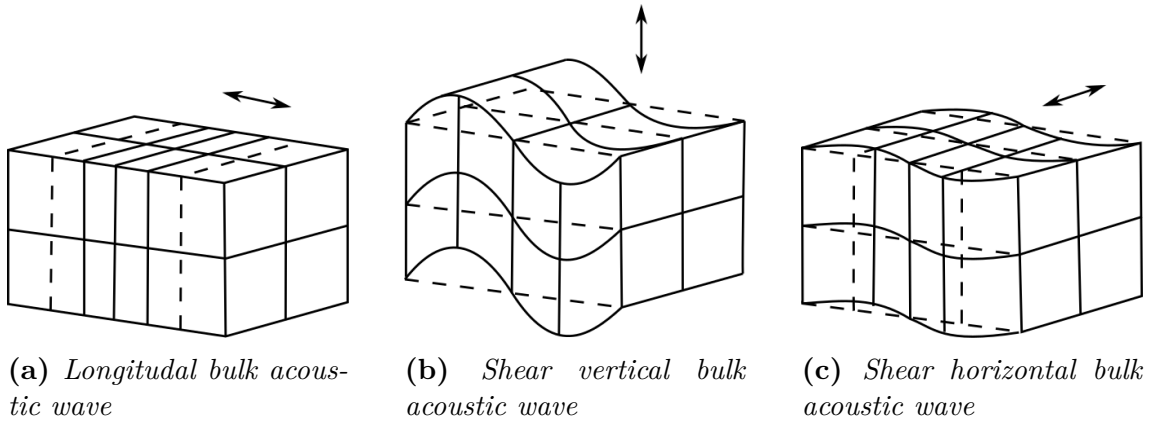


**Figure 2.4:** Schematic of longitudinal and shear bulk acoustic waves.

Elastic waves are attenuated as they propagate, meaning their amplitude is decreased. There are three main reasons for the attenuation of these waves [9]:

1. Inhomogeneities in the propagation medium can cause scattering losses in the waves. This property is dependent on the material and therefore mostly temperature independent.
2. Scattering loss as a result of thermal lattice vibrations in the crystal structure of the propagation material.
3. Thermal diffusion of energy from the wave causing volume change in the material to compensate temperature variation in the material. Since shear waves do not cause volume change, this only affects longitudinal BAW.

### 2.7.2 Surface acoustic waves (SAW)

Surface acoustic waves (SAW) form when the acoustic waves in a bulk material encounters the surface of the material. They are formed as a way for the acoustic wave in the bulk material to satisfy the boundary conditions at the surface [10, 19]. They are often formed by coupling between the *quasi-longitudinal* (LV-type BAW) and the *quasi-shear* (SV-type and SH-type BAW) acoustic waves. The quasi-waves can also couple with the electric potential  $\Phi$  [9].

The displacement profile,  $\vec{u}(y)$  of a generalised Rayleigh surface acoustic wave can be described in the following way [6]:

$$u(\vec{r}, t) = \left( u_x(y)e^{j\phi_1\hat{x}} + u_y(y)e^{j\phi_2\hat{y}} + u_z(y)e^{j\phi_3\hat{z}} \right) e^{j\omega t - \gamma z}. \quad (2.5)$$

This wave propagates in the  $z$ -direction, and  $y$  is the depth into the crystal (substrate),  $\omega$  the angular frequency,  $\gamma$  the complex propagation factor,  $\phi_i$  is the phase of the different displacement components with respect to  $u_z$ .

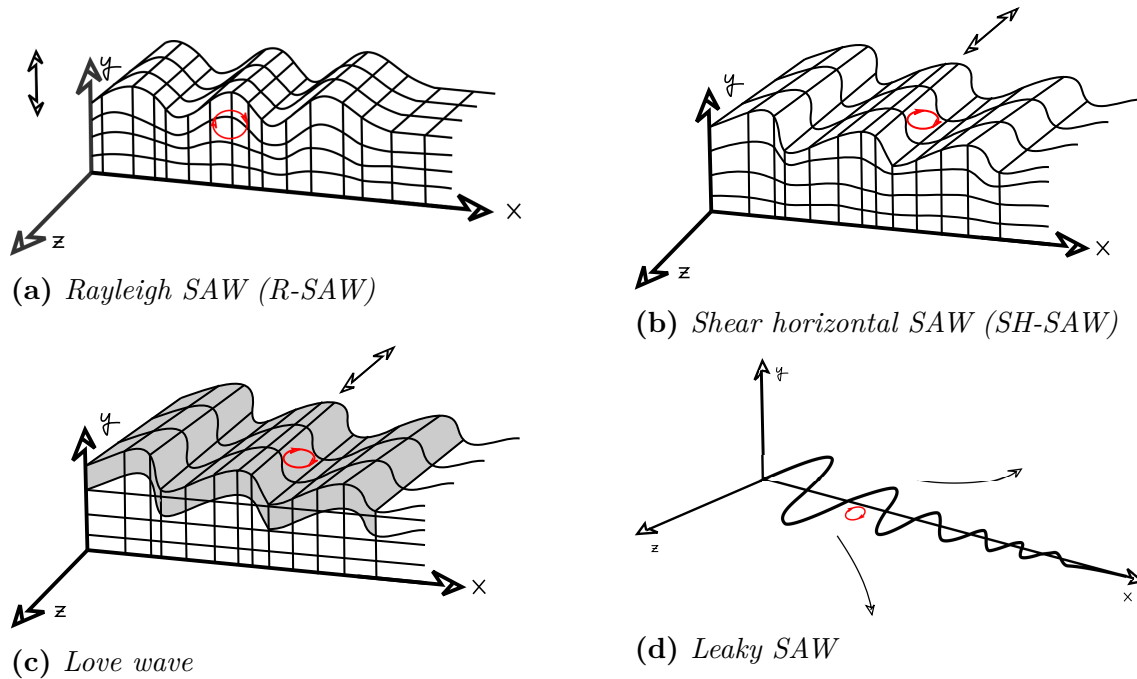


**Figure 2.5:** Schematic of several different surface acoustic waves.

The SH-type BAW component can satisfy the boundary condition at the surface on its own [19]. In that case, it will propagate as a surface skimming bulk wave (SSBW) [24].

There are several different types of SAW. Some of these will be described in more detail in the following sections.

### 2.7.2.1 Rayleigh waves

Rayleigh SAW (RSAW) is illustrated in Figure 2.5a. RSAW is a result of the coupling of the L- and SV-type BAW components (the *quasi-longitudinal* and one of the *quasi-shear* waves described earlier) [9] described in Section 2.7.1, close to the surface of the material. The phase velocity of the RSAW is slower than that of the SV-type BAW [20], meaning most of the wave energy is concentrated at the surface.

A result of the polarization of the RSAW, they will radiate into liquids placed on them [5], making them unsuitable for use in fluid environments. RSAW sensors are commonly used for gas sensor applications [25, 26].

### 2.7.2.2 SH-SAW

SH-SAW are surface acoustic waves with a shear-horizontal polarization, an illustration is found in Figure 2.5b. SH-SAW are formed from SH-type BAW if the boundary condition on the surface causes a slowing down effect [20]. The velocity

of the SH-SAW are typically slower than of the SH-type BAW, indicating that  $K^2$  is stronger closer to the surface [9].

The shear polarization of the SH-SAW make them less prone to radiate into liquids placed on top of the substrate as RSAW [5], making it possible to use SH-SAW in fluid environments with only little damping. The confinement of the energy of the SH-SAW close to the surface makes it able to detect properties of solids or fluids in contact with the substrate surface [5, 25]

On surfaces with specific crystallographic symmetries, a pure SH-SAW can couple with  $\Phi$  and form Bleustein-Gulyaev waves (BG-waves) [9]. The BG-waves have a large  $K_2$  than what R-SAWs have [23], indicating that they are more strongly confined to the substrate surface.

### 2.7.2.3 Love waves

SH-SAWs that exist in guiding layers are called Love waves [9]. These waves are illustrated in Figure 2.5c. The guiding layers are made from materials with a lower shear wave velocity than the bulk material [23].

### 2.7.2.4 Leaky SAW

Leaky surface acoustic waves (LSAW) have velocities higher than the slowest shear wave [18]. Usually, LSAW are a type of SH-type waves with elastic displacement normal to the sagittal plane [18]. They are technically not a surface wave [18], but rather a SH-type SAW propagating accompanied by a slow shear bulk wave radiating into the substrate [20]. This causes some of the energy in the LSAW to "leak" into the substrate, as is illustrated in Figure 2.5d. The surface amplitude of the LSAW will decay according to  $e^{-\alpha X}$  ( $\alpha$  is the attenuation constant and  $X$  a crystallographic axis of the substrate) [27].

# 3

## Microfluidics

Microfluidics is the science and technology concerning the manipulation of fluid streams on the micrometer scale [30, 31], with volumes around  $10^{-9}$  to  $10^{-12}$  litres.

Fluid volume on this scale will behave differently than on the macroscale. Phenomena that are unusual on the macroscale will be commonly occurring on this size scale. One of the most important of these is the laminar flow. These phenomena lead to new challenges, but also to new possibilities.

The potential offered by microfluidic platforms of combining fluid handling with other types of technologies opens up for new kinds of applications, where the functionality of a complete lab is combined into one microfluidic chip, forming a lab-on-a-chip (also known as micro total analysis system,  $\mu$ TAS) [32]. For many purposes, the ideal lab-on-a-chip would be able to handle a sample-in answer-out scenario [33]. This type of device could be used in a variety of applications, including health and environmental monitoring [30].

One option in health monitoring which is investigated presently, is so-called point-of-care testing applications: sensing devices to be used at the point of treatment, providing fast and accurate test results, circumventing the need to lengthy laboratory procedures [34].

Using microfluidics in different types of applications have a range of advantages from the miniaturisation itself, such as lowered reagent consumption, smaller devices, faster read-out times, cost reduction, and a reduction of waste [33, 35, 36].

### 3.1 Scaling laws

In all types of nano- and microtechnology, it is the size or length scale that is the defining factor. For this reason, it is useful to introduce the concept of scaling laws.

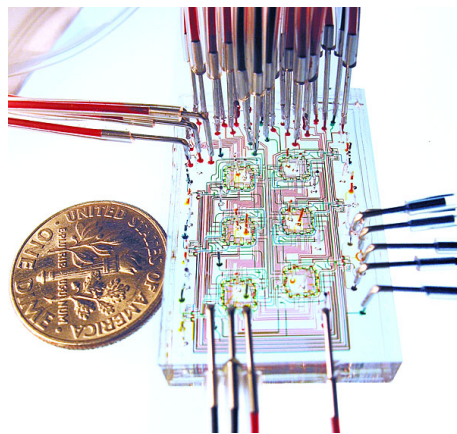


**Figure 3.1:** *Six microchemostats in parallel, [28] via [29].*

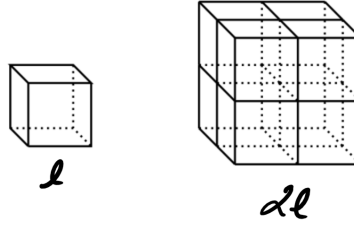


**Figure 3.2:** *The geometric scaling of a cube. The side length of the larger cube is  $2\ell$ , twice as long as the side length of the smaller cube  $\ell$ . It can be seen that the larger cube has a bottom area which is four times as large as the bottom area of the smaller cube, and the larger volume is eight times larger than that of the smaller cube.*

According to Bruuns [37], a scaling law describes how changes in the characteristic length  $\ell$  of a system affect different physical quantities of interest. Essentially, this is a way to determine how much different quantities will be affected by a change in length scale, such as from the macroscale into the microscale.

If scaling laws are applied to the geometry of an object, it will become clear that any change in the characteristic length of this object will affect different properties differently. For instance, take a cube with the side length  $\ell$ . In this case  $\ell$  is the characteristic length of the cube. The area of the cube's bottom surface will be  $\ell^2$  and the cube's volume will be  $\ell^3$ . If the characteristic length is halved to  $\frac{\ell}{2}$ , the area will become  $(\frac{\ell}{2})^2 = \frac{\ell^2}{4}$  and the volume  $(\frac{\ell}{2})^3 = \frac{\ell^3}{8}$ . Comparing the values of the side length, bottom area, and volume before and after the characteristic length was halved, the new values illustrate how much faster the area is decreasing than the length, and how much faster the volume than the area [38]. This implies that the stronger the dependence is on the characteristic length is, the faster will the property of the system decrease with a decreased length scale.

For this reason, volume forces (such as gravity and inertia) will be more affected by a change in characteristic length than surface forces (viscosity and surface tension) [37], as they depend more strongly on the characteristic length. A basic scaling law for this is expressed below:

$$\frac{\text{surface forces}}{\text{volume forces}} \propto \frac{\ell^2}{\ell^3} = \ell^{-1}. \quad (3.1)$$

Equation 3.1 shows that as  $\ell$  decreases, especially in the way it does when scaling down to the microscale where the characteristic length becomes about  $10^6$  times smaller, volume forces will no longer dominate the different phenomena that are occurring, but rather the surface forces. [37].

## 3.2 Equations governing the fluid flow

Since microfluidics deals with different types of fluid flows on the microscale, being able to describe these fluid flows is critical. In this part, the most important equations governing the fluid flows are introduced and briefly explained. These equations describe the fluids' motion, pressure, and how mass is transported within them.

The formulations of Equations 3.3, and 3.6 are taken from [39]. Equation 3.7 is from [37] and Equation 3.11 is from [40]

### 3.2.1 Navier-Stokes equations

The Navier-Stokes is used to describe the flow of a Newtonian fluid and it is essentially a description of the conservation of momentum in the flow. A basis for the Navier-Stokes is the continuity equation,

$$\frac{\partial \rho}{\partial t} + \nabla \cdot (\rho \mathbf{v}) = 0, \quad (3.2)$$

where  $\rho$  is the density,  $t$  the time, and  $\mathbf{v}$  is the velocity of the flow. The first term on the left-hand side in Equation 3.2 describes the accumulation of mass within an infinitesimal volume element in the fluid, and the second term the difference between the flow in and out of the volume element. The continuity equation describes the conservation of mass in the flow, in the same way as the Navier-Stokes equation describes the conservation of momentum. For the Navier-Stokes equation, the fluid is assumed to behave as a continuum and to be incompressible (that is,  $\nabla \cdot \mathbf{v} = 0$ ):

$$\rho \underbrace{\left( \frac{\partial \mathbf{v}}{\partial t} + \mathbf{v} \cdot \nabla \mathbf{v} \right)}_I = \underbrace{\rho \mathbf{g}}_{II} - \underbrace{\nabla P}_{III} + \underbrace{\mu \nabla^2 \mathbf{v}}_{IV}. \quad (3.3)$$

In this equation,  $\rho$  is the density,  $\mathbf{v}$  the velocity vector,  $\mathbf{g}$  the acceleration due to gravitation,  $P$  the pressure, and  $\mu$  the viscosity of the fluid. Moreover, the different parts of the Navier-Stokes equation can be understood in the following way:

- I:** The change in momentum over time.
- II:** the gravitational force acting on the volume element.
- III:** the pressure acting on the volume element.
- IV:** the viscous forces causing eg. shear strain<sup>1</sup>.

For most systems the full Navier-Stokes equation cannot be solved analytically. Due to the specific conditions in microfluidics, simplifications can be made so that it is rarely necessary to use the full Navier-Stokes equation. The easiest way to illustrate this is the rearrange the Navier-Stokes equation to its dimensionless form (for details, see [19, 41]):

<sup>1</sup>A full derivation of the Navier-Stokes equation can be found in for instance [39]

$$\underbrace{\frac{\rho v \ell}{\mu}}_{Re} \left( \frac{\partial \tilde{\mathbf{v}}}{\partial \tilde{t}} + \tilde{\mathbf{v}} \cdot \tilde{\nabla} \tilde{\mathbf{v}} \right) = -\nabla \tilde{P} + \tilde{\nabla}^2 \tilde{\mathbf{v}}. \quad (3.4)$$

It is clear from this form of the Navier-Stokes equation there is just one scaling parameter, the Reynolds number ( $Re$ ). The Reynolds number is defined as:

$$Re = \frac{\rho v \ell}{\mu} = \frac{\text{inertial force}}{\text{viscous force}}, \quad (3.5)$$

and is the ratio of inertial forces to viscous forces in the fluid flow. It is used to characterise fluid flows as to whether the flow is chaotic (turbulent) or ordered (laminar). In the laminar regime closed streamlines cannot exist, meaning that for instance vortices cannot happen [40]. For this reason, a laminar flow will appear to flow as parallel layers, as is illustrated in Figure 3.3.

When  $Re$  is large ( $Re \gg 1$ ), the inertial forces in the flow dominates, making the flow pattern chaotic, or turbulent. For lower  $Re$  numbers on the other hand ( $Re \ll 1$ ), the viscous forces and pressure dominate, making the flow ordered, or laminar. Both flow regimes are illustrated in Figure 3.3.

One of the phenomena specific to fluids on the microscale is that the fluid flows are laminar. The Reynolds number for fluid flows on the microscale is typically in the laminar range,  $Re \ll 1$ . Putting a Reynolds number typical for laminar flow into Equation 3.4 leads to that the entire left-hand side can be neglected, leading to:

$$\nabla P = \mu \nabla^2 \mathbf{v}, \quad (3.6)$$

which is the Stoke's equation. Unlike the Navier-Stokes equation, the Stoke's equation is easier to solve analytically.

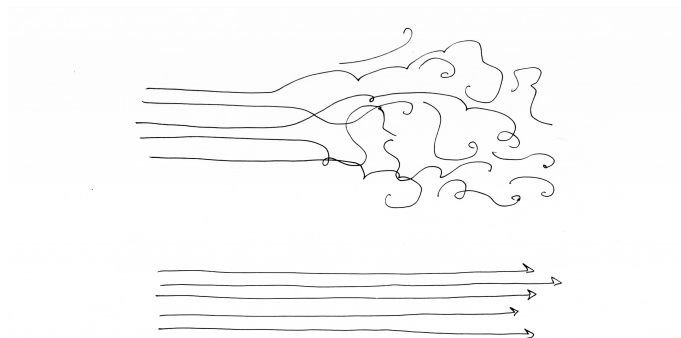


**Figure 3.3:** *The difference between turbulent and laminar flow regimes. The bottom image illustrates the laminar flow regime. The top image illustrates a flow that starts out as laminar and becomes turbulent. The regime between the fully laminar and the fully turbulent flows is called transitional.*

### 3.2.2 Hagen-Poiseuille equation

The Hagen-Poiseuille equation describes the pressure drop in the fluid as it flows through a channel. This equation is based on a few assumptions, and all of these need to be fulfilled for the equation to be valid: the fluid needs to be Newtonian, behave like a continuum and be incompressible, while the flow needs to be laminar, steady-state and fully developed. The Hagen-Poiseuille equation is then formulated in the following way,

$$\Delta P = R_H Q, \quad (3.7)$$

where  $P$  is the pressure [ $Pa$ ],  $R_H$  hydraulic resistance [ $\frac{Pa \cdot s}{m^3}$ ], and  $Q$  the flow rate [ $\frac{m^3}{s}$ ]. The hydraulic resistance is the resistance against flow in the channel itself, which is a combination of the resistance against flow in the channel geometry and the resistance resulting from the fluid itself. The exact value of the hydraulic resistance is dependent on the dynamic viscosity of the fluid and on the channel geometry.

There are expressions for the hydraulic resistance for straight channels with different cross sections. The two most important are the ones for channels with a rectangular cross section or a square cross section. The hydraulic resistance for a straight channel with a rectangular cross section is calculated according to the following expression:

$$R_H = \frac{12\eta L}{1 - 0.63(h/w)} \frac{1}{h^3 w}, \quad (3.8)$$

where  $\eta$  is the (dynamic) viscosity of the fluid,  $L$  the length of the channel,  $h$  the height of the channel, and  $w$  the width of the channel. For square channels, where the channel width is the same as the channel height  $w = h$ , the expression can be simplified to the following expression:

$$R_H = 28.4\eta L \frac{1}{h^4}. \quad (3.9)$$

The expressions in Equation 3.8 and 3.9 are taken from [37].

### 3.2.3 Hagen-Poiseuille equation and Ohm's law

Something which is useful when designing fluidic circuits is the analogy between the Hagen-Poiseuille equation and Ohm's law [37, 40],

$$\Delta V = RI. \quad (3.10)$$

As can be seen by comparing Equations 3.7 and 3.10, the pressure in the Hagen-Poiseuille equation corresponds to voltage, fluid flow to current, and hydraulic resistance is equivalent to resistance. This means that it is possible to use the more well-known theoretical approaches from electrical circuit theory to design microfluidic networks.

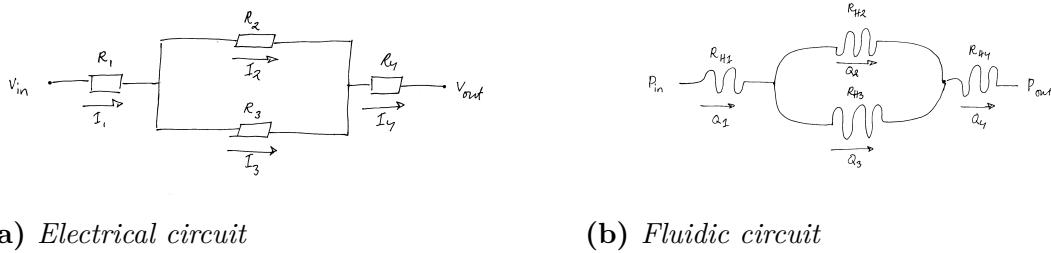


**Figure 3.4:** An electrical circuit (a) and its fluidic equivalent (b). The main difference between them is how the resistors are constructed.

A consequence of the analogy is that Kirchoff's laws are valid for fluidic circuits [37, 40]:

- The sum of the fluid flows  $Q$  meeting in a node must be zero,  $\sum_{k=1}^n Q_k = 0$ . This corresponds to Kirchoff's current law.
- The sum of the total pressure differences in a closed loop must be zero, corresponding to Kirchoff's voltage law. This is not crucial when open loops are concerned.

The hydraulic resistance is, as mentioned earlier, an equivalent to resistance in electric circuits. As a result of this, it is possible to construct fluidic resistors of sorts to increase the hydraulic resistance in a fluidic circuit, in much the same way as electrical resistors are used in electronic circuits, as is seen in Figure 3.4. This is done to, for instance, make sure that the total pressure differences in the fluidic circuit are zero. In addition, the hydraulic resistance in series and parallel can be calculated in exactly the same way as electronic resistance is.

### 3.2.4 Mass transport

To be able to fully describe the dynamics of fluids in microfluidics, more than just the Navier-Stokes equations are needed. In fluid flows with more than one component (such as particles or different fluids), the different components will mix with each other. The transport of these different components in a flow will be the focus of this section.

Mass transport in fluid flows is caused by a combination of two different phenomena: convection and diffusion. Convection is transport as a result of the movement of the fluid, while diffusion is transport resulting from the presence of a concentration gradient in the fluid. In microfluidic flows, mass transport by diffusion will be a more important transport phenomenon than on the macroscale. This is a result of the shorter lengths, lower velocities, and the laminar flow. Convection also matters if the velocity of the fluid flow is non-zero [37].

The most important equation used to describe the mass transport on the microscale

is the so-called convection-diffusion equation<sup>2</sup>, which can be considered as the mass transport analogue to the Navier-Stokes equation:

$$\underbrace{\frac{\partial c}{\partial t}}_I = \underbrace{D\nabla^2 c}_{II} - \underbrace{\mathbf{v} \cdot \nabla c}_{III}, \quad (3.11)$$

where  $c$  is the concentration of the solute in the solution,  $t$  the time,  $D$  the diffusion coefficient for this particular solute-solvent pair, and  $\mathbf{v}$  is the velocity.

**I:** the change in concentration of the solute over time

**II:** the diffusive transport term, where  $D$  is the diffusion coefficient, which is dependent on both the solvents and the solutes,

**III:** the convective transport term, i.e. transport caused by the flow of the solution. In analogue to the Navier-Stokes equation, the convection-diffusion equation may similarly be converted to a dimensionless form<sup>3</sup>, which yields two scaling parameters similar to the Re number in the dimensionless Navier-Stokes equation: the Pe (Péclet number) and the St (Strouhal number).

$$St \frac{\partial \tilde{c}}{\partial \tilde{t}} = \frac{1}{Pe} \tilde{\nabla}^2 \tilde{c} - \tilde{\mathbf{v}} \cdot \tilde{\nabla} \tilde{c} \quad (3.12)$$

The St number is a measure of unsteadiness in the flow. Pe can be considered as a direct analogue to the Re number with,

$$Pe = \frac{\ell v}{D} = \frac{\text{convection}}{\text{diffusion}}, \quad (3.13)$$

which is the ratio between convective and diffusive mass transport, where  $v$  is the (characteristic) flow velocity,  $\ell$  the (characteristic) length, and  $D$  the diffusion coefficient. Pe can be used to determine whether convective or diffusive mass transport dominate.

### 3.3 Applications

The focus of this chapter until this point has been the theoretical background to microfluidics, not any of the different applications of microfluidics. Some of these will be the focus of this section.

As has been mentioned earlier in this chapter, microfluidics utilizes scaled-down fluidic circuits and therefore almost any application involving liquids can be scaled down. Often this means that different chemical or biological applications are scaled

<sup>2</sup>A full derivation of the convection-diffusion equation can be found in [37] or in [40]

<sup>3</sup>For derivation see [41]

down, as these tend to be done in fluid environments. The special phenomena occurring on the microscale, such as laminar flow, opens possibilities for things that are not possible on the macroscale.

Some of the many examples of microfluidic technology include complete devices such as lab-on-a-chips, or components such as droplet generators and manipulators, valves, mixers, sorters, and concentrators.

However, some of the characteristics that are unique for fluids on the microscale can also introduce problems which do not need to be considered on the macroscale. These problems require new solutions. For instance, the laminar flow common on the microscale leads to that very fundamental operations on the macroscale, such as mixing, becomes challenging on the microscale.

In general, planar microfluidic devices consist of a minimum of two layers: a polymer microfluidic device with channels and another one to seal the channels. Creating devices with more layers is possible, as are creating 3D structures. The sealing layer can of course be functionalised in some way and be used to combine more functionalities on the same device, making this a very flexible type of technology.

SAW are described in chapter 2 and how the SAW can be used for sensing purposes is described chapter 4. In addition to this, SAW can also be used in combination with microfluidics to manipulate fluid flows in different ways, or also to manipulate particles, cells, and droplets in these fluid flows.

#### 3.3.1 Lab-on-a-chip

Lab-on-a-chips are, as stated in the beginning of this chapter, a class of microfluidic devices constructed with the aim of containing the same functionality as a macro-sized lab, and will therefore contain a mix of microfluidic and miniaturised non-fluidic components [31].

As is the case in a "real" lab, the lab-on-a-chip needs to be able to do more than just the analysis, it needs to prepare the sample for analysis, do the analysis, and deliver the result in some way. The sample preparation can consist of several steps, and different microfluidic components might be needed for all of them. Typical sample preparation steps include dilution, separation, concentration, mixing, and transportation, to mention just a few. For the analysis, it is very likely that some type of non-fluidic parts needs to be integrated on the lab-on-a-chip. The non-fluidic components may or may not be compatible with fluid environments, which need to be taken into account.

In addition to all of this, the lab-on-a-chip also needs to communicate the result of the analysis to the outside (*chip-to-world*) by some type of electronic integration. Ideally, it should also be possible to load the sample to the lab-on-a-chip in an easy

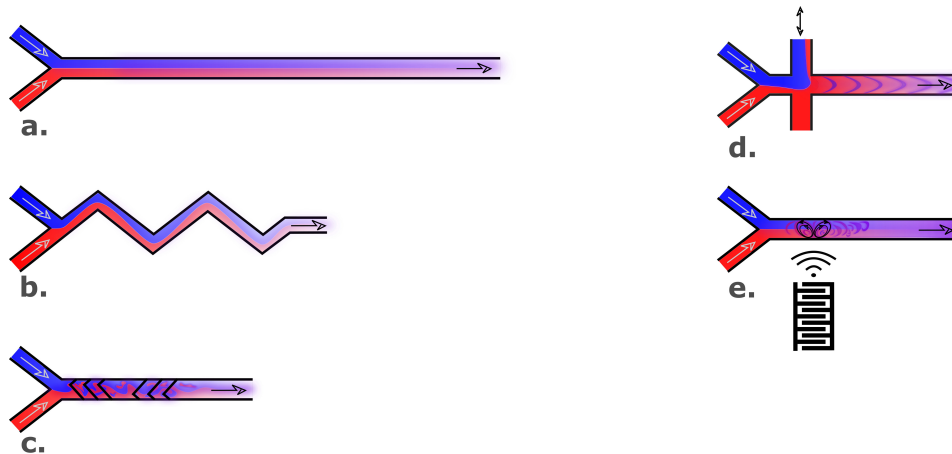


**Figure 3.5:** *Some examples of microfluidic mixers. Passive mixers a-c: a. diffusive mixer, b. zigzag mixer, c. herringbone mixer. Active mixers d-e: d. pulsed pressure mixer, e. mixing by acoustic streaming.*

way. Additionally, the aim with many lab-on-a-chip devices are that they should also be portable, to facilitate testing in situations where it would be difficult to bring the sample to a lab, instead bringing the lab to the sample [36]. Needless to say, there are many challenges to overcome to have a functioning lab-on-a-chip which needs to be considered at an early stage [35].

Typical applications for lab-on-a-chips includes point-of-care sensors to be used in health care [33, 34, 42] and to a lesser degree in environmental sensors that can be brought into the field [36].

### 3.3.2 Mixers

One of the challenges in microfluidics in general is how to mix different fluids, as this will mainly happen through diffusion when the flows are laminar and it will take longer time than on the macroscale. In integrated lab-on-a-chip systems, mixing is a critical step which needs to be performed in connection to the other operations in the circuit. As a consequence of this, some type of mixers are needed. Mixers can be either active, where some type of external forces are used, or passive, where the contact area of the species to be mixed is increased only by changes in the channel design [43].

Some different examples of passive and active mixers are illustrated in Figure 3.5. Mixers a-c are various types of passive mixers: a. is a pure diffusive mixer and the channel length needed for mixing the two fluid flows are very long, in b. and c. the channels are designed to increase the turbulence in the fluid flow and, as a direct consequence, also increase the mixing between the two fluid flows. This is done by increasing the contact area between the two flows [43]. Both mixers b. and c. need less channel length for achieve mixing as a result of this compared to a.

Active mixers, such as the examples d. and e. in Figure 3.5 require more components

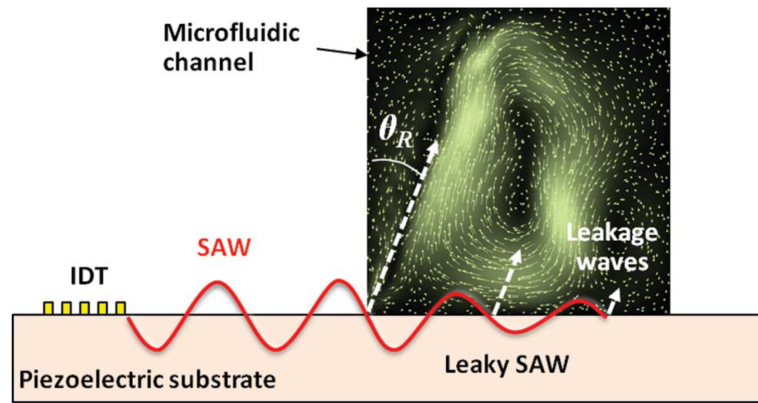


**Figure 3.6:** Rayleigh SAW used to manipulate the fluid flow or particles in a microfluidic channels by acoustic streaming [12].

than the passive mixers, making the fabrication of them more complex. The main advantage of using active mixers is that the channel length required for complete mixing is typically shorter than for the passive mixers [43]. The mixing can also often be turned on or off. There exist several different approaches for how to construct active microfluidic mixers, but only two of them will be mentioned here. The first is mixer d. in Figure 3.5, a pulsed pressure mixer [44] where the mixing is done by stirring the fluid flows in the main channel by pressure pulses from the side channels. The second option illustrated here is to use SAW to induce acoustic streaming, which in turn creates turbulence, and as a result, mixing [45, 46]. Acoustic streaming is often seen as an unwanted side effect in microfluidic applications where SAW are involved, but as is seen here, it can also be utilised in different ways [46].

### 3.3.3 Particle gates

Here, *particle gates* refers to an acoustofluidic device capable of trapping particles in a fluid flow by use of SAW. This makes it possible to, for instance use them to increase the concentration of particles in the solution.

SAW and microfluidics can be combined for use in different microfluidic applications. SAW to induce acoustic streaming in a flow for mixing has already been mentioned. Other ways of combining these two disciplines include using the SAW to manipulate particles or cells, droplets, and fluid in continuous or stagnant flows. For instance SAW can be used to sort particles and droplets, fluid translation, or focus particles in a stream, or to trap particles [12].

The trapping of particles, droplets, cells, and other objects by SAW works by using the energy that radiates from Rayleigh SAW (RSAW) into the fluid as they are propagating over the surface of the substrate. This is illustrated in Figure 3.6. RSAW are typically not used in fluid sensor applications, because of their tendency to radiate into the bulk fluid.

In order to be able to manipulate objects in fluid flows, an acoustic radiation force  $F^{rad}$  is needed [47]. This force arise from standing waves in the microfluidic channel. The acoustic radiation force is related to the acoustic potential  $U^{rad}$  [48]:

$$F^{rad} = -\nabla U^{rad}. \quad (3.14)$$

The acoustic potential  $U^{rad}$  is a function of the radius of the object (the object is assumed to be spherical), the compressibilities and densities of the fluid and the particle [48].

The objects will move either to the points of minimum or maximum acoustic potential in the standing wave. Whether the objects will move to the minimum or maximum points is dependent on the density and compressibility of the object and fluid [47].

In order to trap objects against the flow, and not just move them between flow paths (acoustophoresis), the local  $U^{rad}$  need a high gradient at the point of capture [47].

The acoustic force can also be thought of as acoustic pressure. An easy way to produce standing waves is to let two wave fronts interact with one another at resonance. The wave fronts are created by IDTs. The waves will have an one-dimensional interference pattern. The interference pattern is related to the acoustic force, and there will subsequently be a one-dimensional pattern of acoustic pressure nodes (points of minimum acoustic potential) and anti-nodes (points of maximal acoustic potential). By designing the interference pattern it is possible to decide where the objects should be trapped.

The size of the objects needs to be of a comparable size to the wavelength of the standing wave. This makes it possible to design the system after what objects are to be trapped, by choosing wavelengths to be used. This opens for the option of using acoustic traps for size-based sorting of particles.



# 4

## Sensors

Sensors are devices which are used to quantify their surroundings. Naturally, this makes them highly fundamental in many fields, from simple thermometers to complex bio-chemical sensing systems. Different fields have different requirements on the sensors, such as to what changes in their environment they need to be sensitive to and how sensitive they need to be to these changes. In this chapter, some of the different figures of merit which are used to characterise sensors will be presented, along with how it is possible to use SAW to detect changes in their environment.

### 4.1 Overview

There are some principal building blocks that need to be present in sensor systems: the sensor itself, a transducer, and an actuator. These terms are general, and the definitions will also be general.

**Sensor:** a device that produce an output signal in response to some input quantity [6] or, a device that responds to some type of physical stimulus [49].

**Transducer:** converts one type of energy into another [49, 50].

A further classification of sensors has to do with how the device interacts with an outside energy source: *active* devices consume power, while *passive* devices interacts with the power in the circuit without consuming it [6].

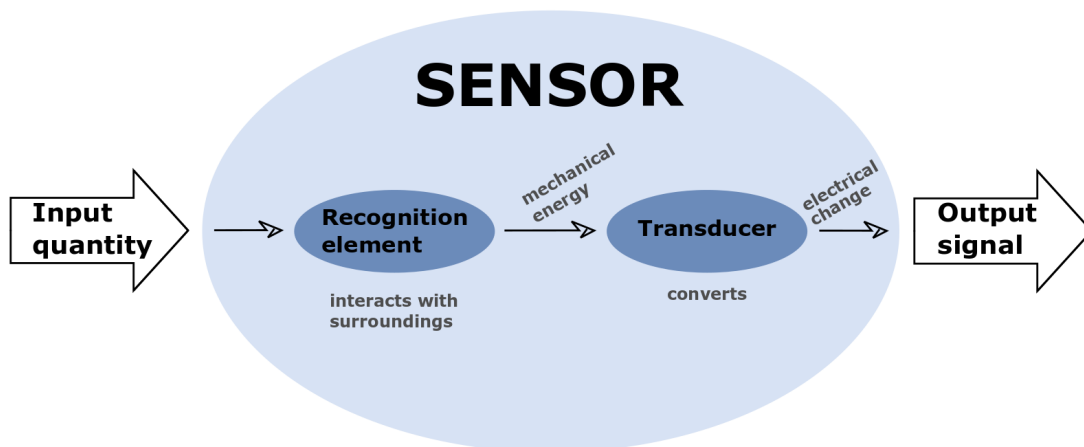


Figure 4.1: Schematic of the general components of a sensor.

Characterisation of the performance of sensors can be done depending on the performance of some different parameters, some of which are listed below:

**Sensitivity** is defined as the change in the output of a device per unit change in the input [6, 22], or as the ratio of the variation in output signal and the variation of the measured variable [40].

**Bandwidth** is the frequency range of input signals the sensor functions at [6, 49, 50].

**Noise** is unwanted electrical signals within electronic devices that causes spurious responses [22].

**Limit of detection (LOD)** is the smallest value the parameter of interest can take and still be detected by the sensor. This translates to  $3\sigma$  of the noise level, where  $\sigma$  is the standard deviation. [6, 51]

**Hysteresis** is a memory effect within the system, where the response is dependent on the previous history of the system [6, 49].

**Resolution** is the minimum change of input quantity that a sensor is able to detect [6].

**Dynamic range** can be seen as the range of possible input values the sensor can produce valid output signals for [22]. The lower end of the dynamic range is the LOD and the upper is the saturation level [6].

**Linearity:** a sensor might be considered to be either linear or non-linear depending on the size of the maximal deviation between an imagined linear relationship between the input and output signals, i.e. the deviation from a linear transfer function [19, 49, 50].

**Accuracy** is the closeness between the true and the measured value in a specific measurement [50, 52, 53, 54]. In other words, a measurement made with good accuracy means that the errors in this particular measurement is below an acceptable level.

**Selectivity** is how well the sensor can distinguish one (or a small group) of analytes as input from the rest of the sample [6, 53]. This is especially important for chemical and bio-chemical sensors.

## 4.2 Noise

The presence of noise in the measurements makes it important to have methods to discern between the signal of interest and the noise. A measurement that is often used for this purpose is the signal-to-noise ratio. When this ratio is deemed to be high enough, the signal is deemed to exceed the noise level.

The standard deviation  $\sigma$  is often used to estimate the noise level in a measurement. For instance, this is the case when the signal-to-noise ratio coincides with the LOD,  $3\sigma$ . The standard deviation is especially useful to estimate white noise in measurements. In some measurements, however, there are other types of noise which can be difficult to estimate using the standard deviation. One such case is measurements of an oscillator's frequency instability [55], where the Allan deviation  $\sigma_y(\tau)$  (also known as the two-sample deviation) is used instead of the standard deviation.

The idea when using the Allan deviation is to compare two consecutive frequency measurements sampled over a set time period  $\tau$ . If the measurement is stable, the difference between these values will be small over the sampling period, resulting in a low Allan deviation.

### 4.3 Biosensors

According to the International Union of Pure and Applied Chemistry (IUPAC), a biosensor is a chemical sensor which transform chemical information into an analytically useful signal, utilizing a bio-chemical mechanism [56,57]. A biosensor contains a biologically derived element as part of the transduction process [54, 58, 59] which therefore respond to biochemical changes. This definition means that a lot of sensors can be used for biological or bio-chemical measurements without being biosensors.

Biosensors can be found in many different places, and in a variety of applications, in much the same way as sensors in general. However, applications in research and healthcare tend to dominate. The classic examples of biosensors are the blood glucose sensors used by diabetes patients and at-home pregnancy test [58, 59]. These two classes of sensors are also examples of so called point-of-care sensors, intended for use close at the point where care is administered, allowing for testing and patient diagnoses to be made faster and more efficiently as the customary laboratory step is eliminated [60].

### 4.4 Surface acoustic wave sensors

If all of the concepts which already have been introduced (acoustic waves, microfluidics, and sensors) are combined, they can make up a type of microfluidic integrated surface acoustic wave sensor, as will be described in this section.

Simply put, the basis of a SAW sensor is that the waves, generated on the device surface, are strongly dependant on their environment, from which it follows that if there are changes in the environment, there will also be changes in the mechanical waves, and these changes can be monitored [61].

As a result of the concentration of SAW energy close to the substrate surface, SAW devices are very sensitive to mass changes on their surface. This makes them ideal to use as sensors which measures different types of changes on the surface of the device.

To be able to use a SAW device in a sensor system, more parts are normally required than just the SAW device. If the sensor will be used for chemical or bio-chemical measurements, which mostly are made in-liquid, some type of delivery system is required to deliver the analyte to the sensor, i.e. a microfluidic circuit. For the sensor to be selective to the analyte of interest, it will need to be coated with some sort of functionalised sensing layer, as the SAW sensor is not inherently reactive with

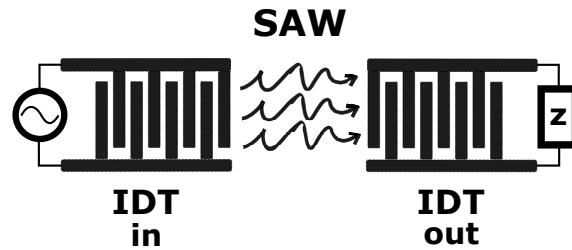


**Figure 4.2:** *Image of a typical delay line SAW sensor system*

any bio-chemical species. As it is possible to add different sensing layers to a SAW sensor after it has been fabricated, this approach makes the SAW sensor system flexible since it can be used with a variety of analytes.

#### 4.4.1 Different SAW sensor configurations

There are several different approaches on how to best place the IDTs to generate SAWs in a sensor application. Some of these will be described below.

##### 4.4.1.1 Delay line

One configuration commonly used for SAW sensors is the so-called delay line, illustrated in Figure 4.2. It consists of two IDTs placed a finite distance apart from one another. The first IDT generates a SAW that, with some time delay, reaches the other IDT with a phase shift and generates an output electrical signal [4, 6, 61]. If this configuration is to be used in a chemical or bio-chemical sensor, there will often be a sensing layer placed between the two IDTs, as was described earlier.

The design of delay lines means that there is a possibility to put some object in the area between the IDTs. If that is the case, the phase  $\phi$  will be a function of the frequency, meaning that an object on the surface will cause a change in wave velocity. The phase dependence of the frequency is a result of the different diffraction indices of the materials on the delay line. This is explained by Snell's law.

The IDTs that make up the delay line configuration is made by depositing a stack of different metals on the piezoelectric substrate. The deposited layers on the substrate have two primary functions. The first is to guide the acoustic wave and to decrease the energy loss the wave might experience [62]. The second function is how the layer might be functionalised to better suit the intended use of the sensor, for instance depositing a layer of  $\text{SiO}_2$  to promote lipid adhesion.

Using delay line configurations in sensors is connected with some disadvantages. These include that it is not possible to easily detect resonant frequency, due to the length the wave front have to travel between the IDTs, these devices suffer from high energy losses, and they can be hard to incorporate in a compact system.

#### 4.4.1.2 SAW Resonator

In an attempt to get past some of the disadvantages with using a delay line configuration, Hohmann et al. [63] presents an alternate approach, consisting of a two-port SAW resonator. Compared to the delay line configuration, the IDTs in the SAW resonator configuration are placed closer together making the "delay line" space smaller and both IDTs have reflectors on the side opposite to the spacing.

Devices built with the SAW resonator configuration also have distinct transmission resonances making detection of the resonance frequency comparatively easy [63]. This can be compared to the delay lines, which do not have an easily defined resonance frequency.

However, in using this approach the IDTs are still at some risk of being short-circuited by the liquid conductivity and the transmission losses are large [19, 63], although not as large as it is for the delay lines.

#### 4.4.1.3 One-port and two-port SAW resonators

It is most common to use two-port resonators for SAW sensing purposes, as was used in [63]. This design has one port on the electronic interface for the input signal and another port for the output signal. This leads to a limitation in how small the electronic interface can get, as there is inevitably a minimum of two cables or ports per resonator. A one-port setup, as the one that is demonstrated in [64], uses the same port for both input signal and output signal, eliminating some of the bulk while at the same time making the device more compact. In general, the one-port approach has several advantages: it is more robust than the two-port approach, it is easier to incorporate in other electronic interfaces, and the one-port approach eliminated the need for much of the post processing of data.

### 4.4.2 Detection mechanisms

When a SAW sensor is used for in-liquid sensing, the main mechanism for sensing is the shift in wave velocity and phase caused by changes to the mass deposited on the sensor surface. This type of detection mechanism is called mass loading and is the most commonly used detection mechanism in chemical and bio-chemical SAW sensors today. It is at the same time possible to use SAW sensors to detect other properties in a sample, such as the viscoelastic properties of the sample. Some of the basic theory behind these detection mechanisms are outlined below.

#### 4.4.2.1 Mass loading

The mass change on the surface of the sensor might be a result of a chemical reaction between the analyte and the functionalised sensing layer, but it might as well be a

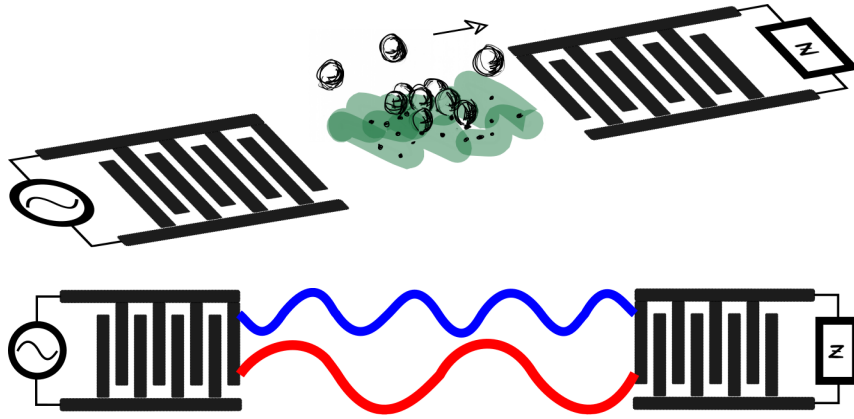


**Figure 4.3:** An illustration of the principle mass loading on a delay line SAW-sensor. The top image shows a (functionalised) lipid bilayer deposited on the SAW-device with functionalised nanoparticles binding to the lipid bilayer. The bottom image shows how the SAW is affected by the mass loading caused by the deposited materials: the blue wave is before mass deposition, and the red wave after the mass deposition where the frequency and phase of the wave has been shifted.

result of a sorptive interaction (adsorption or absorption) between the analyte and the sensor layer [6]. The formulation of equations 4.1, 4.2, 4.3, 4.4 are taken from [6].

The velocity shift in SAW caused by mass loading on the sensor is described in Equation 4.1:

$$\frac{\Delta v}{v_0} = -c_m f_0 \rho_s, \quad (4.1)$$

here  $v$  is the velocity,  $f$  the frequency,  $c_m$  the mass sensitivity factor, and  $\rho_s$  is the surface mass density. The equation describes how a change in the surface mass (or surface mass density) causes a change in the SAW velocity. The mass sensitivity factor is defined as:

$$c_m = \frac{\pi v_0}{2} \left( \frac{v_{x0}^2}{\omega P} + \frac{v_{y0}^2}{\omega P} + \frac{v_{z0}^2}{\omega P} \right) \quad (4.2)$$

where  $P$  is defined as the acoustic power. A more general description of the frequency shift caused by mass loading is found in Equation 4.3,

$$\Delta f_m = \Delta f_0 = -\kappa S_m \Delta m_A. \quad (4.3)$$

In which  $\Delta f_0$  is the frequency shift,  $\kappa$  a geometric factor for the fraction of active device area being perturbed,  $S_m$  a device specific constant, and  $\Delta m_A$  the change in  $\frac{\text{mass}}{\text{area}}$  on the device surface.

The shift in SAW velocity ( $v$ ), resonant frequency ( $f$ ), and phase ( $\Phi$ ) are connected by the following equation:

$$\frac{\Delta v}{v_0} = \frac{\Delta f}{f_0} = \frac{\Delta \Phi}{\Phi_0}. \quad (4.4)$$

#### 4.4.2.2 Viscoelastic properties

If the SAW sensor is designed for SAW that are not completely damped by the liquid on the sensor it is possible to both use the sensor in liquid and to measure the viscoelastic properties of the liquid sample. Depending on what the sample consist of, this can be an important factor to measure. For instance, blood coagulation can be measured by monitoring changes in the blood sample's density, as is done in [13].

The wave velocity of waves travelling in a fluid is strongly dependent on the density of that fluid. Since frequency and wave velocity are connected according to  $f = \frac{v}{\lambda}$ , a shift in the wave velocity will cause a shift in the resonant frequency as well. This frequency shift can be measured and read-out in the same way as the frequency shift caused by mass loading (for instance, by particles on the sensor). The sensor response to the frequency shift is proportional to the square root of the product density and viscosity:  $\sqrt{\rho\eta}$ . [6]

#### 4.4.3 Read-outs

Most SAW devices operates in the radio frequency (RF) range. This means that any measurements needs to be made by a device which can operate on those frequencies, such as a network analyzer.

The ability to operate on a wide range of frequencies, ranging from MHz to the GHz range, is typical of network analyzers. Normally, a measurement in a network analyzer is made by sending a sinusoidal wave generated by the network analyzer through the device under test (DUT) and the response is then measured by the same network analyzer. The vector network analyzer (VNA) measures both the amplitude and phase of the incident and reflected waves in the VNA. In addition, a VNA can be used to characterise both one- and two-port systems. [65]

The parameter that is most commonly used when characterising SAW devices is the scattering parameters, also known as S-parameters [9]. The S-parameters describes the relationship between the input- and the output-voltage (or current) of the VNA [66]. In other words, the S-parameters describe how the device under test

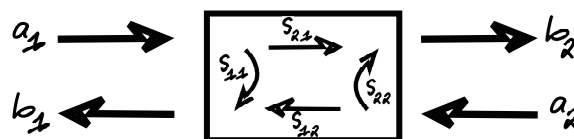


**Figure 4.4:** Incident and reflected signals and scattering parameters in linear two-port circuit.

affects the input signal, making it possible to characterise the device.

In Figure 4.4, a 2-port circuit is illustrated, with port 1 on the left side and port 2 on the right side. In the figure,  $a_i$  is the incident signal and  $b_i$  the reflected signal.  $a_i$  and  $b_i$  are both normalised so their square corresponds to their power. [9]

For a linear circuit, as the one in Figure 4.4 the relationship between the input and the output signals can be described in the following way:

$$\begin{bmatrix} b_1 \\ b_2 \end{bmatrix} = \begin{bmatrix} S_{11} & S_{12} \\ S_{21} & S_{22} \end{bmatrix} \begin{bmatrix} a_1 \\ a_2 \end{bmatrix}, \quad (4.5)$$

where  $S_{ij}$  are the different scattering parameters. As is illustrated in Figure 4.4,  $S_{11}$  and  $S_{22}$  describes how the signal is reflected at port 1 and 2, respectively. They are therefore referred to as the reflection coefficients and sometimes denoted  $\Gamma$ .  $S_{12}$  and  $S_{21}$  describes how the signal is transmitted between port 1 and 2, and are known as the transmission coefficients and denoted  $T$ . [9]

Equation 4.5 can be simplified as SAW devices show reciprocity [9], meaning that the device properties are unchanged if the in- and output ports are exchanged, leading to  $S_{12} = S_{21}$ .

In addition, the S-parameters can also be used to describe the losses in the system.  $-20\log|\Gamma|$  is the return loss and  $-20\log|T|$  the insertion loss. [9]

If a DUT is connected to a transmission line with specific impedance  $R_0 = G_0^{-1}$ , the reflection  $\Gamma$  can be measured at the point  $L$  (the length of the transmission line) in order to take the phase delay caused by propagation of the signal into account. The expression for  $\Gamma$  is then<sup>1</sup>:

$$\Gamma = \Gamma_0 e^{-2j\beta_0 L}, \quad (4.6)$$

with  $\beta_0$  as the wave number of the signal. The wave number is a function of the frequency of the electromagnetic wave that is the signal in the transmission line.

If the expression for admittance  $Y$  is set to be  $Y = G + jB$  (the real part  $G$  is the conductance and the imaginary part  $B$  the susceptance), the expression for  $\Gamma$  can be rewritten as,

$$|\Gamma|^2 = 1 - \frac{4GG_0}{(G + G_0)^2 + B^2}. \quad (4.7)$$

Assuming that  $G_0 \gg G, |B|$ , the expression can be simplified to

$$-20\log|\Gamma| \cong \frac{40G}{G_0}, \quad (4.8)$$

meaning that the return loss is directly related to the radiation conductance of the IDT [9].

---

<sup>1</sup>The following is described in detail in [9, p.69]

# 5

## Method

In this chapter the complete process of fabricating the SAW sensor is described, starting with the design and ending with the sensor characterisation. In Figure 5.1, the order of the different steps is outlined. The SAW device is fabricated separately from the microfluidic device in two parallel processes: the SAW device is made using lift-off lithography, while the microfluidic device is made with soft lithography. The two parts are then bonded together in the final fabrication step, thus forming the complete sensor.

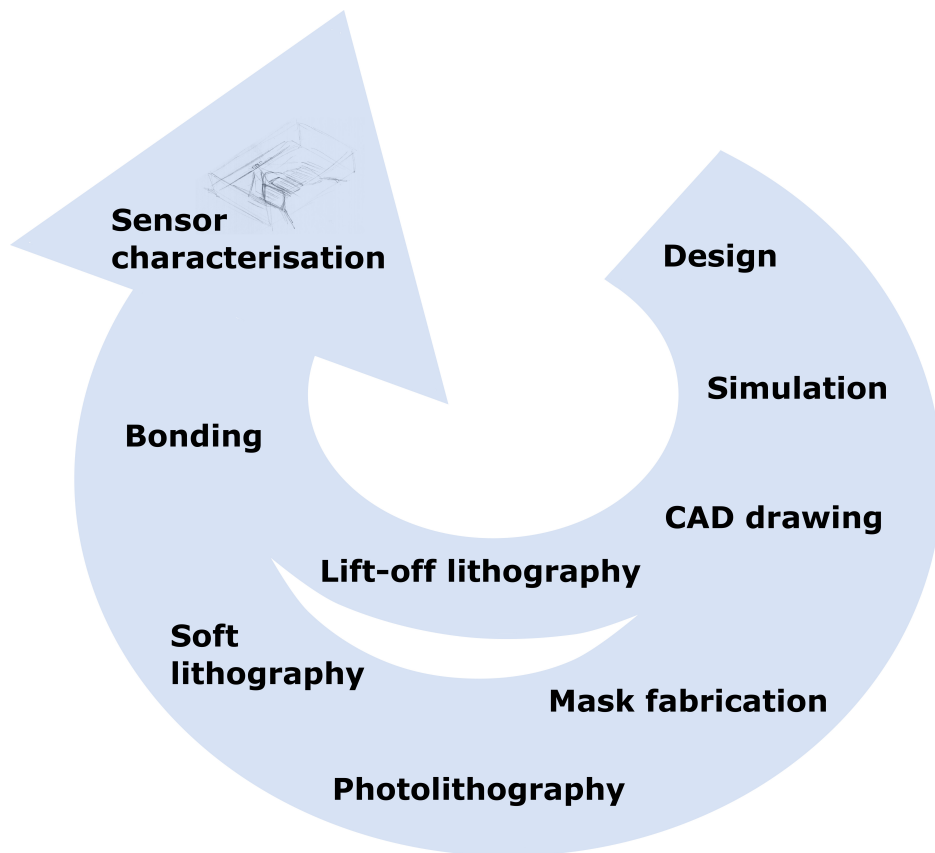


**Figure 5.1:** *The steps in the complete SAW device fabrication process.*

## 5.1 Design

The first step of the fabrication process is to design the parts of the device.

### 5.1.1 Simulation

Before a specific design is decided on, the different options will have to be evaluated by simulations, as to decide on the ideal design option without having to fabricate several different versions of the same design.

The equations describing the fluid flow and the wave motion are all partial differential equations (PDE). Systems of PDEs are complex and difficult to solve analytically. To approximate a solution to these types of PDE systems, they are reformulated to form systems of algebraic equations on discrete elements in the finite element method (FEM) [67]. The area or the object where the physical phenomena are happening is divided into smaller, finite elements. The system of finite elements are called a mesh. The finite elements can be made larger or smaller depending on what level of detail the system needs to be solved for. The points where the finite elements meet are called nodes. The values of the nodes are determined either by a boundary condition, or by subsequent calculations.

COMSOL Multiphysics was used for the simulations. It is based on finite element analysis (FEA) and contains packages for simulations of several different physical phenomena at the same time, allowing for concurrent simulations of the different phenomena happening on the device, in much the same way they would occur in reality [68].

The results of the simulation of the shear displacement caused by two different types of surface acoustic waves on the surface of a piezoelectric substrate are found in Figure 5.2.

### 5.1.2 Drawing

The next step of the design process is to draw the complete design in a format that can be used by the software in the equipment in the later process steps. It is also important to consider and take the shrinking ratio into account. PDMS shrinks about 1% to 2% when it cures [69], which means that the PDMS design needs to be 1% to 2% larger than the desired size of the finished device.

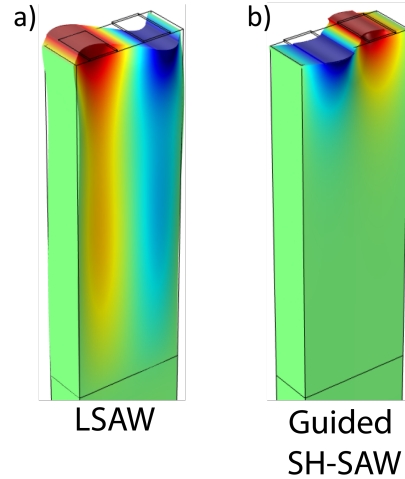


**Figure 5.2:** A typical COMSOL simulation image of shear displacement. a) LSAW on a free surface, b) SH-SAW on a surface guided by a periodic gold grating [8].

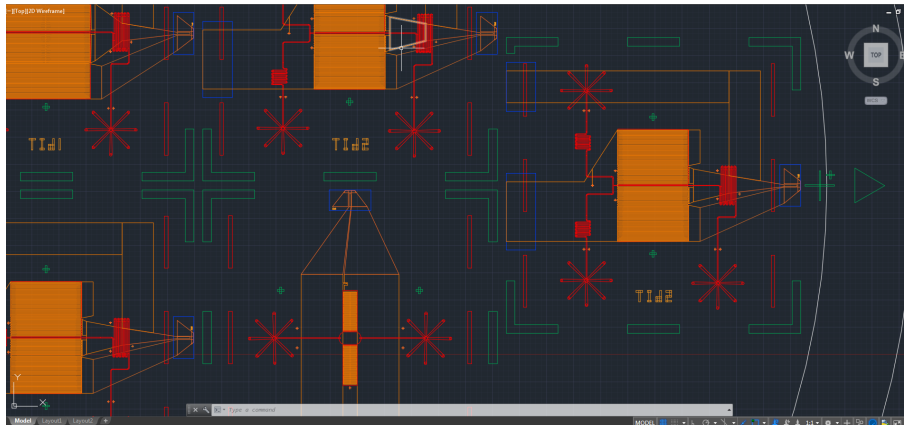


**Figure 5.3:** A portion of an AutoCAD drawing of particle concentration devices placed on a wafer, including all parts of the devices. The different colours denotes different layers in the drawing, and also different parts of the design.

Figure 5.3 shows a part of an AutoCAD drawing of several particle concentration devices. The different colours are used to illustrate different layers in the design, where some of them will make up the microfluidic circuits (red) and others are the IDTs in the SAW devices (orange). Other parts of the drawing are alignment or cut marks that are necessary, but do not really form part of the finished device. As a note on the size of the devices and the other structures in Figure 5.3 it can be said that the red microfluidic channels are  $50\ \mu\text{m}$  wide.

## 5.2 Device fabrication

The SAW device and the mold of the microfluidic device are both made using microfabrication, different techniques used to fabricate on the micrometer range [70], at the Chalmers's Nanofabrication Laboratory (MC2).

Many of the techniques used in micro- and nanofabrication were developed for use in microelectronics, such as integrated circuits. These by now well-established fabrication techniques can also be used for other purposes than only microelectronics, as is done in this project.

The two types of lithographies presented here are used to fabricate two different parts of the finished device. The additive lift-off lithography process is used to place stacks of metal thin-films on a piezoelectric substrate to form the IDTs and contacts of the sensor. The SU-8 based photolithography process is used to fabricate a mould to be used in the soft lithography process. Uncured PDMS will then be poured over the mould and after it has cured, will form the microfluidic part of the sensor device.

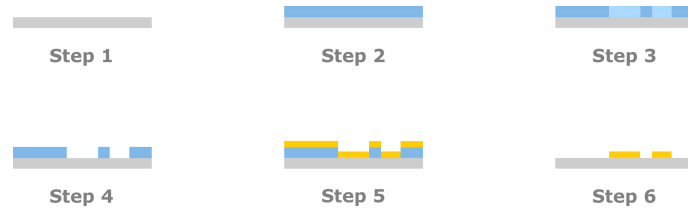


**Figure 5.4:** *The process steps in a standard lift-off fabrication process.*

### 5.2.1 Lift-off lithography

A process based on lift-off lithography is used in this project to fabricate the SAW sensor device.

Lift-off lithography is a process which consist of depositing an additional layer on a substrate by using a temporary layer as a means to transfer the pattern. The temporary layer is later removed, leaving only desired pattern made up from the additional layer on the substrate. One version of this process is illustrated in Figure 5.4. The process in the figure consist of coating the substrate with a photoresist (step 2), in which a pattern is then formed (step 3). The pattern can be made by photolithography. The resist is developed, forming openings in the resist (step 4). A metal thin-film (the additional layer) is deposited on the substrate, but it is only deposited directly on the substrate in the openings made earlier (step 5) [71,72]. To achieve reproducible results using lift-off, it is crucial that the deposited metal films do not cover the side walls of the photoresist, meaning that the directional deposition of thin-films achievable by evaporation is the only valid deposition option [71]. As a final step, the unwanted metal thin-film is removed from the substrate by dissolving the underlying photoresist (step 6). This final step is what makes up the lift-off portion of this process.

The properties of the photoresist is another important process factor. The profile of the developed photoresist (undercut, vertical, or overcut) will need to be taken into consideration, as well as the pattern to be made and the thin-film deposition method.

The most important steps of the lift-off based process used in this project is illustrated in Figure 5.5. The first step, as in any microfabrication process, is to prepare the substrate surface by removing any contamination. These contaminations can be ionic, organic, or a native oxide layer on the substrate material, all of which might need to be removed [70]. The risk is otherwise that the adhesion of any additional layers is compromised and of process failure. In this specific process, the cleaning of the substrate (Y-cut X-propagation LiNbO<sub>3</sub>, a synthetic piezoelectric crystal) is done by cleaning it in an O<sub>2</sub>-plasma (60 W, 30 s) followed by submerging the wafer in a remover bath containing mr-Rem 400 [73] and sonicate for 10 minutes, followed by similar immersions in isopropanol (IPA) and in deionized water. When using Y-cut LiNbO<sub>3</sub> the native oxide is not needed to be removed. Lastly, the wafer is rinsed in water a final time and blow-dried with N<sub>2</sub>.

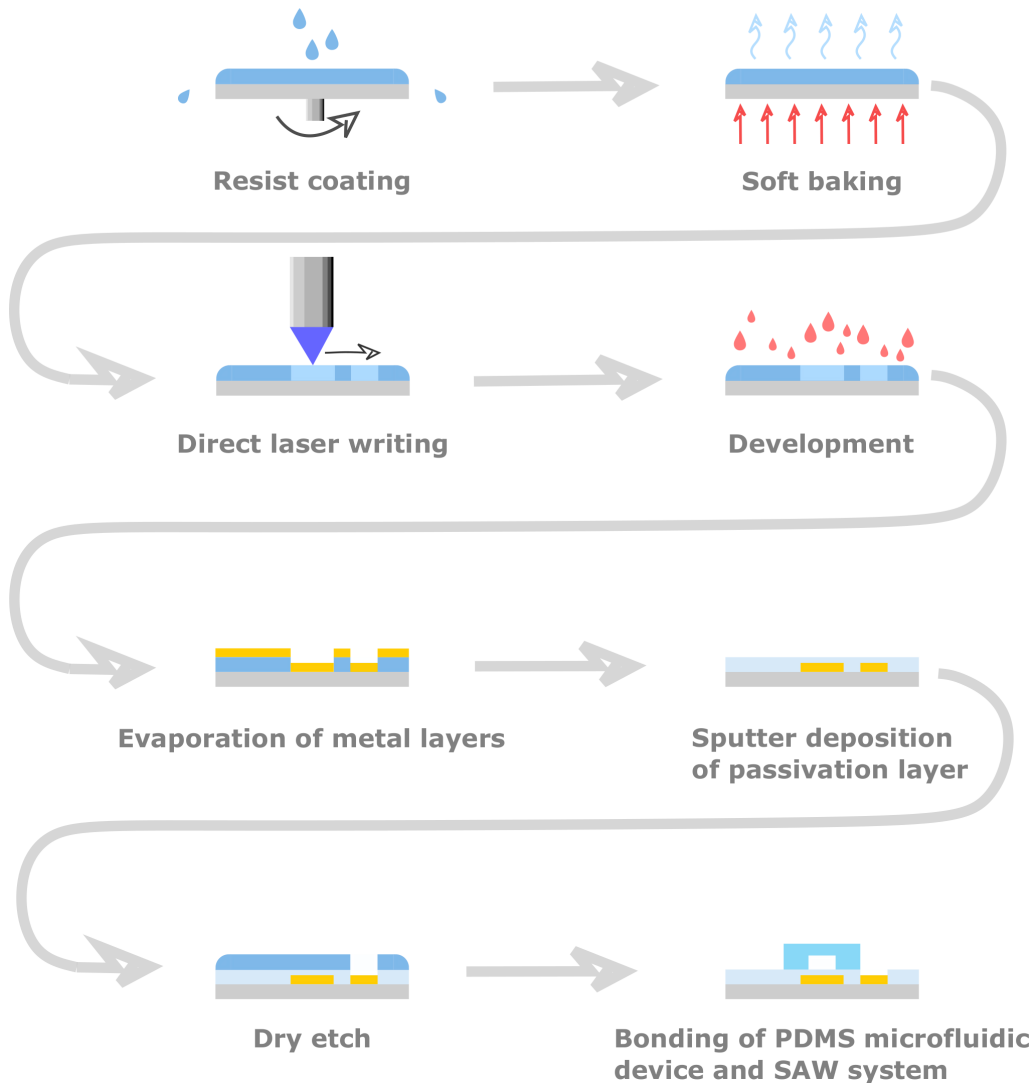


**Figure 5.5:** Schematic of the lift-off lithography based process

The next step is to apply a thin HMDS (hexamethyldisilazane) layer to the wafer to promote better resist adhesion. The HMDS forms a monolayer on water-free surfaces by binding its Si-atom to the oxygen on oxidised surfaces [74], making the surface hydrophobic. The wafer is heated to 110 °C before applying the HMDS. This is to make sure that the wafer and the HMDS hotplate both have same temperature. The HMDS is applied in a so-called bubbler, allowing for the application of only a very thin layer in a water-free atmosphere [74].

A layer of the positive image-reversal AZ5214E resist [75] is spin-coated on the wafer to a thickness of 1.5  $\mu\text{m}$ , as illustrated in the first step in Figure 5.5. In this case, image-reversal refers to the process of reversing the mask pattern on the wafer, by exposing the area outside the pattern. When the photoresist is baked in a later process step, the chemical bonds in the exposed photoresist are broken. In a positive photoresist, the parts which are exposed become soluble in developer, leaving openings in the resist after development [76]. The AZ5214E resist is developed for

lift-off processes requiring the resist to have an undercut. After spin-coating, the substrate is soft baked at 110 °C to evaporate the solvents in the resist.

The resist is exposed and the pattern is made using direct laser writer (Heidelberg Instruments DWL 2000) at  $\lambda = 405$  nm. Unlike photoexposure, which exposes the photoresist through openings in a photomask (more on this in Section 5.2.2), direct laser writing consist of a laser beam which scans the substrate line by line and produces a pattern by exposing the resist pixel by pixel. This is illustrated in the third image in Figure 5.5.

Next, the substrate is reverse-baked (to reverse the pattern) at 125 °C, to break the chemical bonds in the resist in the exposed areas, making them soluble [75]. The substrate us then flood exposed, that is, exposed to UV-light without a photomask, at  $\lambda = 365$  nm in the Suss semi-automated mask aligner MA 6 to add more energy to the reactions in the resist to break the bonds in the exposed areas and to aid the curing process in the unexposed areas. The AZ5214E resist is exposed like a positive resist in this process, but behaves like a negative resist with extra features.

The resist is developed in developer AZ351B [77], mixed with deionized water at a ratio of 1:5, and the exposed parts of the resist are dissolved, forming the pattern in the resist, seen in the fourth image in Figure 5.5. The last remnants of the resist and the HDMS primer are removed by a descum process (plasma ashing) on O<sub>2</sub>-plasma at 50 W.

The next step is illustrated in the fifth image in Figure 5.5, where a 300 nm stack of metal thin-films have been deposited on the substrate to make up IDTs and contacts. The stack (25 nm Ti, 260 nm Au, and 25 nm Ti) are evaporated in turn using the Lesker PVD 225 e-beam evaporator (also e-beam physical vapour deposition, EBPVD). The target metals are bombarded by an e-beam in vacuum, whereupon they vaporise, then solidifies again, covering everything within the line-of-sight in the vacuum chamber [78].

Once the metal stack has been deposited on the substrate, it is time for the lift-off, where the AZ5214E resist and the metal thin-film on top of it are removed, leaving only the metal stack in the desired pattern of IDTs and contacts, as is seen in Figure 5.4. This is done by immerse the substrate in acetone overnight, allowing the acetone to dissolve the resist completely. Another approach is to immerse the substrate in acetone but to sonicate and warm it to 65 °C, which speeds up the process.

A 100 nm layer of SiO<sub>2</sub> is sputtered on top of the substrate to passivate the surface and improve the bond to the PDMS in the microfluidic device (see Section 5.2.2). The FHR MS 150 Sputter is used for this, and as for the evaporation this is another PVD technique. Unlike the evaporator, the target atoms are ejected from the bulk material after being hit by ions (Ar<sup>+</sup>) from a plasma [70]. As this happens in vacuum, the target atoms then travel to the substrate, where they are deposited. If a gas, such as oxygen or nitrogen, is allowed in the chamber, the released target atoms can react with the gases, forming oxides or nitrides on the substrate surface [70].

To deposit a layer of  $\text{SiO}_2$ , the target material silicon is hit by ions in an oxygen atmosphere. The result will look something like the sixth image in Figure 5.5.

Now the substrate has been completely covered by an insulating  $\text{SiO}_2$  layer, preventing short-circuits but also preventing contact with external wires connecting the device to a vector network analyzer (VNA). Part of the contacts needs to be opened up so the device can be connected to a VNA, which is done by etching away the  $\text{SiO}_2$  layer where the contact openings will be. This is done by, once again, covering the substrate with a positive resist, by spinning a  $1.2\ \mu\text{m}$  layer of AZ1512 [79], which is soft baked to evaporate the solvents in the resist at  $100\ ^\circ\text{C}$ . The resist is exposed by direct laser writing at  $405\ \text{nm}$ , only on the parts where the contact openings will be. The resist is developed in MF-CD-26 [80], dissolving the exposed part of the resist. The unprotected  $\text{SiO}_2$ -layer is removed by reactive-ion etching using  $\text{NF}_3$ -plasma ( $50\ \text{W}$ ,  $30\ \text{s}$ ) in Oxford Plasmalab 100 Dry etch ICP. The resist is removed with mr-Rem 400 and following the first cleaning step in this process.

The SAW devices are now ready be bonded to the microfluidic devices.

## 5.2.2 Photolithography

A microfluidic device is used to deliver fluid sample to the SAW-device in an efficient way. This device is fabricated using soft lithography, which will be described further on in this thesis, by pouring a polymer on a mould. The mould is made by fabricating permanent structures on a wafer by photolithography. The resulting device from this process step will not make up a permanent part in the finished sensor device, but the microfluidic delivery system cannot be fabricated without it. The structures in the mould are fabricated in SU-8, an epoxy-based negative permanent photoresist [81], as raised structures on the wafers. The main steps of the photolithography process in this project are illustrated in Figure 5.6.

As with the lift-off lithography, the first step in this process is to clean the substrate ( $4''\ \varnothing 525\ \mu\text{m}$  thick silicon wafer), which is done by immersing the substrate in a buffered oxide etch (BOE) solution, rinsed in water and blow dried with  $\text{N}_2$ . The wafer is spin-coated with SU-8 2035 [81]. The thickness the photoresist is spun down to depends on the design of the microfluidic channels, as the thickness of the SU-8 will determine the height of the channel, typically on the scale of  $50\ \mu\text{m}$ , which can be compared to the thickness of the first resist in the lift-off process:  $1.5\ \mu\text{m}$ . The SU-8 is then pre-baked in two steps, at  $65\ ^\circ\text{C}$  and  $95\ ^\circ\text{C}$  for a total of  $15\ \text{min}$  to make sure the solvents will evaporate in the full thickness of the resist [81].

The exposure is done with UV-light at  $365\ \text{nm}$  through a photomask (Compugraphics, chromium coated soda-lime, dark-field) in the Suss semi-automated mask aligner MA 6. As SU-8 is a negative photoresist, it polymerises when exposed [76] and the dark-field photomask therefore has openings for the pattern. An illustration of the exposure is found in the third step in Figure 5.6.

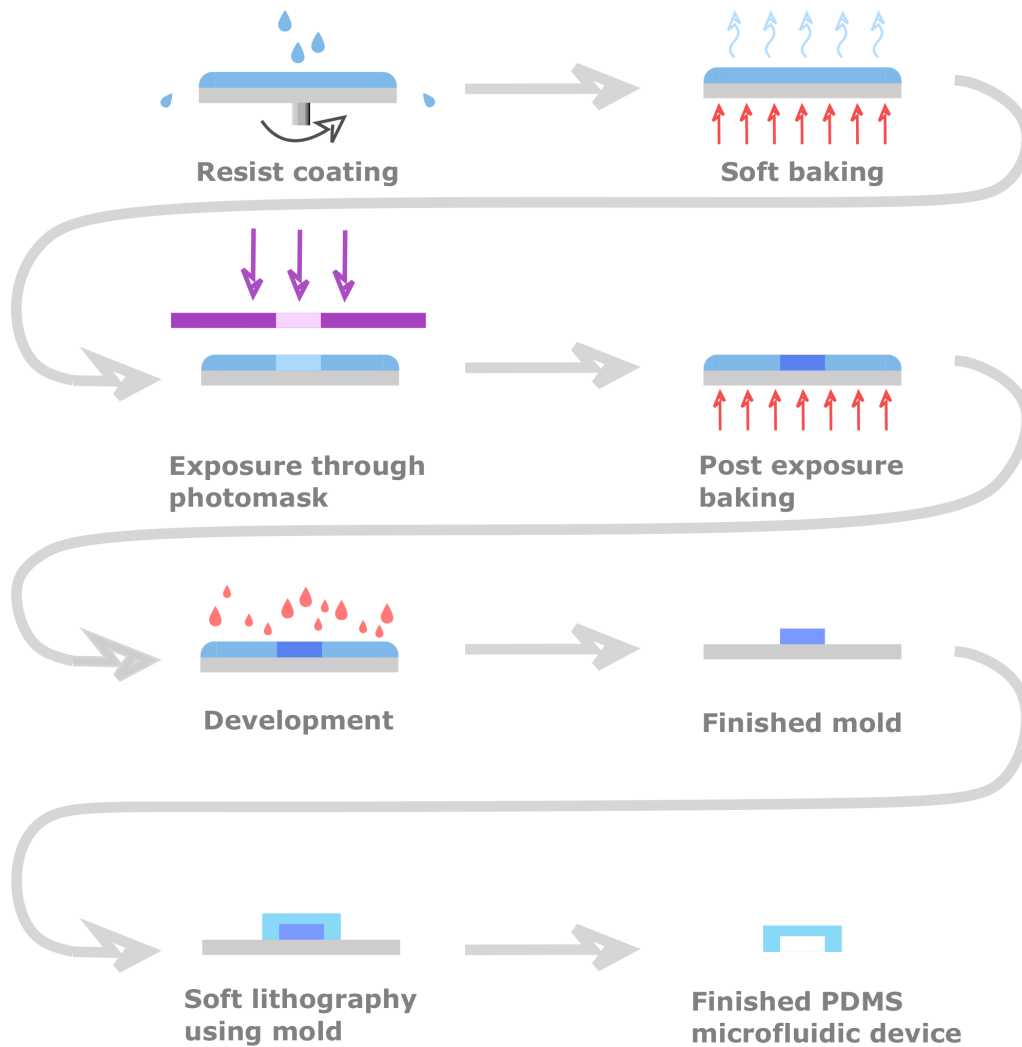


**Figure 5.6:** Schematic of the photolithography process and, in the last three steps, a rough outline of the fabrication of microfluidic PDMS structures.

The next step is the post-exposure bake, which is done in two steps, at 65 °C and 95 °C, to minimise stress in the resist. The purpose of this bake is to add enough energy to the SU-8 so the polymerisation started by the exposure can finish completely.

The SU-8 is developed in mr-Dev 600 developer and rinsed in IPA. To remove any traces of unexposed resist, the substrate is put descummed in an O<sub>2</sub>-plasma etch using the PlasmaTherm Reactive Ion Etcher (RIE). The final step in this photolithography process is to hard-bake the SU-8 by ramping it up to 200 °C and then down to room-temperature. This is done to release any built up stress in the photoresist. Since the SU-8 is hard-baked at a temperature higher than its glass transition temperature, the hard-baking will also smooth out the surface. The device is now a finished master mould, as is seen on the sixth image in Figure 5.6.

Once the mould is finished, the surface needs to be passivated, done by leaving it

in a desiccator with approximately 0.1 mL trichloro(1H,1H,2H,2H-perfluoro-octyl)-silane (Aldrich 448931-10G) overnight, to prevent the PDMS from bonding to the Si-wafer.

### 5.3 Soft lithography

The fabrication techniques used up to this point to make the SU-8 mould have been developed for microelectronics. Soft lithography, on the other hand was developed for applications in chemistry, bio-chemistry, and biology rather than microelectronics, and better suited for those kind of applications [82, 83]. Soft lithography is technically an umbrella term for several different fabrication techniques that all have in common that they make use of some type of soft polymer (often this polymer is polydimethylsiloxane (PDMS)) rather than some type of hard material such as silicon or metals [83, 84].

The specific soft lithography method used in this project to fabricate the microfluidic devices is called *replica molding* [82]. This method consists of a positive patterned master is used as a mould and is cast with an uncured polymer. As the polymer cures, it forms a negative replica of the master. A rough illustration of this process is found in the last three steps in Figure 5.6.

Polydimethylsiloxane (PDMS) is a polymer consisting of a siloxane backbone [-Si-O-Si-] with two methyl groups [-CH<sub>3</sub>] per monomer, as is seen in Figure 5.7a. It has several properties that makes it especially useful as a material for different microfluidic applications: it can be fabricated fast and easily, at a low cost, it is transparent, chemically inert, permeable to gases, and is non-toxic [33, 85, 86]. PDMS has become the dominating building material for microfluidics, especially since the process of soft lithography was introduced in the 1990s by Xia and Whitesides [82], but there are also other materials which can be used in a similar way to PDMS: PMMA (poly(methyl methacrylate)), PC (polycarbonate), cyclic olefin copolymer (COC) [87, 88, 89].

A standard procedure was used to fabricate the microfluidic devices: the base and curing agent of Dow-Corning Sylgard 184 PDMS [90] was mixed at a 10:1 weight-ratio. The mixture was thoroughly stirred and degassed in a vacuum desiccator for 30 minutes, to remove any bubbles in the mixture. After this, the mixed PDMS is poured over the SU-8 mould. The PDMS will be left to cure in an oven at 80 °C for 1 hour. The cured PDMS slab is then removed from the mold, cut into devices along designated cut lines and holes are punched to make fluidic in- and outlets. The microfluidic devices are now ready to be bonded to the SAW-devices, which is described in detail below.

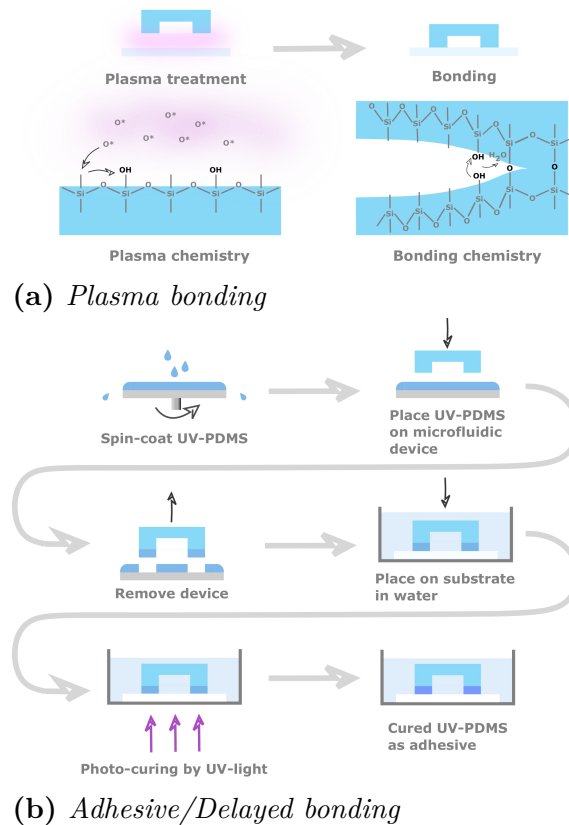


**Figure 5.7:** *PDMS chemical structure and oxygen plasma bonding chemistry*

### 5.3.1 Bonding

An important part of the fabrication process is to bond the microfluidic devices to a substrate. The substrate might function only as a sealing layer, to keep the fluids from escaping or evaporating from the channels in the microfluidic device. The substrate might also be functionalised in some way. There exist an array of different methods to bond microfluidic devices together, either with another device or with a substrate: using the self-adhesive properties of some materials (PDMS in particular) to form a reversible bond with the substrate when it is pressed against the substrate and van der Waals bonds are formed [41, 91], thermal fusion bonding which consists of heating the substrate to a temperature over the glass transition temperature of that particular material [92], fusion bonding and anodic bonding are both used for hard surface materials (for instance glass and Si) [40, 92].

#### 5.3.1.1 Plasma bonding

As PDMS has become almost the dominant material in microfluidics, so has oxygen plasma bonding to seal the channels and bond the device to a substrate. This bonding method has several advantages, maybe the most important being that it does not need any adhesive layer which might clog the channels and it can be performed at comparatively low temperatures.

The plasma bonding procedure is found in Figure 5.7a. Both surfaces are cleaned

from loose particles and the surfaces where the bond will be are activated in an O<sub>2</sub>-plasma chamber (Atto Plasma Chamber, Diener Electronic GmbH) for 45 s at 0.2 mbar, 30 SCCM, 100 W.

Alignment of the microfluidic device and the SAW sensor device was done under a stereo microscope. To allow for adjustment of the alignment, MilliQ (18.2 MΩ) was placed on the SAW sensor surface to keep the two surfaces apart and preventing bonding until the MilliQ has evaporated [93]. The assembled device was left for 30 min until the MilliQ had dried and covalent bonds had formed between the two components. The final step was for the assembled device to be baked at 80 °C for 10 min.

### 5.3.1.2 Adhesive bonding

Most of the mentioned bonding techniques requires the materials to meet some conditions, such as the ability to withstand very high temperatures (thermal fusion bonding) or to possess self-adhesive properties to the substrate material. Needless to say, this is not always the case. Sometimes there is a need to bond materials which are not ideally suited to be bonded together. By using adhesive bonding the requirements on the bonding materials are somewhat lessened. The surfaces of the bonding material can be rougher than what is needed for plasma bonding [40,41,92]. Many different materials have been used as the adhesive layer, see the review by Temiz et al [92] for an overview, for instance both thin layers of uncured PDMS and different UV-curable adhesives have been used as the gluing or adhesive layer. Using flowing adhesives always brings the risk of clogging the microfluidic channels in the process. Adhesive tapes have also been used to seal the channels and bond microfluidic devices to substrates [92].

In case some biological material has been deposited on the substrate before the microfluidics device has been bonded to it, the system needs to be kept in water at all times and at temperatures no higher than 37 °C. This means that the device needs to be bonded in some way that does not involve oxygen plasma or curing in an oven, and it needs to be done in water.

The idea is to use a type of adhesive bonding with a UV-curable PDMS (Shin-Etsu KER-4690) [94] as the adhesive layer (the “glue”). This method is tailored to use with a SLB (supported lipid bilayer) on the sensor surface, and as lipids are not damaged by UV-light, UV-curable PDMS is a valid choice. The process is illustrated in Figure 5.7b, but in short it consists of spinning the UV-PDMS to the desired thickness on a transfer wafer, then stamping down the microfluidic device on the transfer wafer to place a UV-PDMS layer on it, then placing the microfluidic on the substrate surface, exposing the UV-PDMS and finally leaving it to cure. The method of placing uncured UV-PDMS only on the parts of the microfluidic device that does not consist of channels in the way it is done in Figure 5.7b is called “stick-and-stamp” bonding and is described in [95,96].

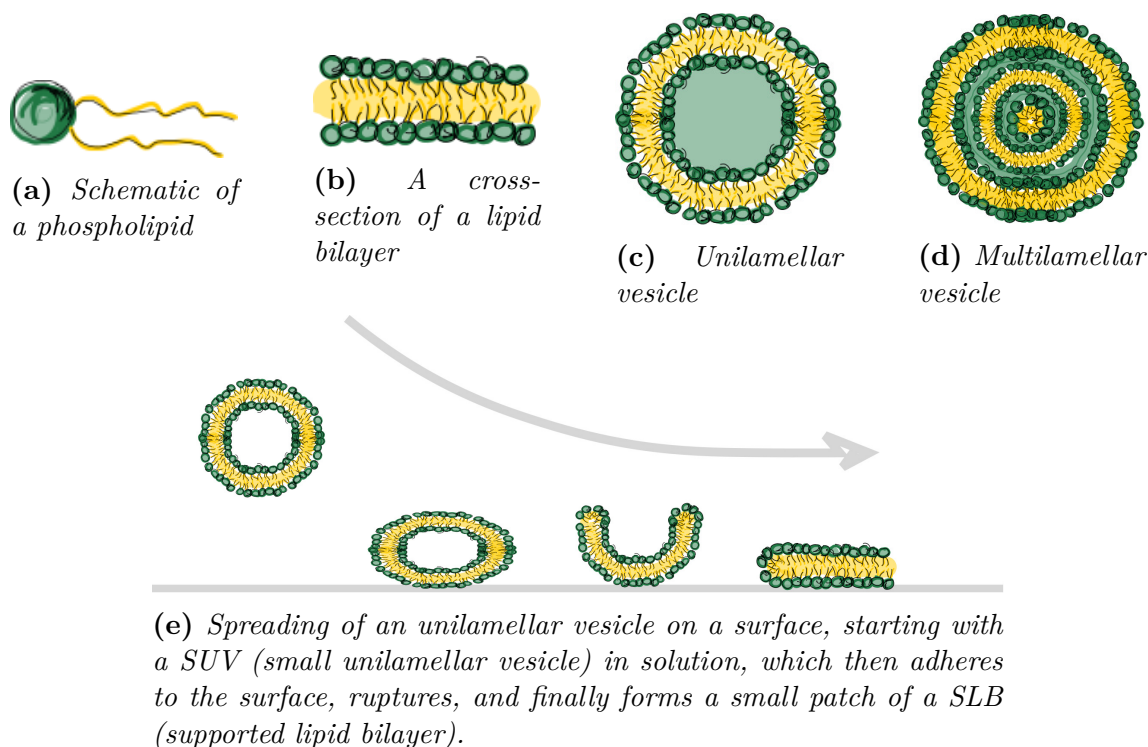


**Figure 5.8:** Schematic of lipids, vesicles and lipid bilayers.

As a first step UV-PDMS is deposited on a glass wafer by spin-coating using spin coater (WS-400BZ-6NPP/LITE, Laurell Technologies Corporation). The UV-PDMS is deposited on the microfluidic device by sticking the microfluidic device on the transfer wafer and then removing it, now with uncured UV-PDMS covering everywhere where there are no channels and the device should bond to the substrate. The microfluidic device is placed on a substrate, which has already been covered by, for instance, a SLB. The UV-PDMS is exposed, in water<sup>1</sup>, by UV-light at 365 nm, which will not damage the SLB. In the final step, before the device can be used, the UV-PDMS is allowed to cure, either for a longer period in room temperature or for a shorter period at elevated temperature in an oven, the exact curing times can be found in [94]. If an SLB or some other biological material has been deposited on the substrate, curing at a higher temperature is of course not possible.

## 5.4 Lipid membrane

Once the sensor device has been finished: the sensor and the microfluidic devices have been fabricated and bonded together, it is ready to be characterised. The characterisation is described in Section 5.5. At times, a supported lipid bilayer (SLB) can be used as either a means to functionalize the sensor surface or when the sensor is used to monitor biomolecule interaction [19]. A SLB is useful as a model to mimic biological membrane and are therefore useful when using this sensor to study some characteristics of the SLB.

<sup>1</sup>It is of course possible to do this type of bonding procedure in air as well.

### 5.4.1 Background

Lipids are a class of biomolecules and are amphiphilic, meaning that they contain both a hydrophilic part and a hydrophobic part. Typically, this corresponds to a hydrophilic head-group, illustrated in Figure 5.8a with the green circle, and a hydrophobic tail, the yellow part in Figure 5.8a, often consisting of two hydrocarbon chains [97].

The importance of lipids lie in the fact that they make up biological membranes, which separate the cell from its surroundings and divide the inside of the cell into compartments [97,98]. This function is something very fundamental and was probably crucial for the early development of life [98].

Not all types of lipids make up membranes, but those that do is the focus of this section, specifically glycerophospholipids (phospholipids), which make up a significant part of the membrane lipids in nature [97,99]. Which types of lipids that form membranes, or other structures, is determined by the stereochemistry of the lipid molecule [97].

Lipids form membranes, or other structures, in the following way: if the lipids are kept in an aqueous environment, they will spontaneously group together by the non-polar hydrophobic tails associating together, forming a lipid bilayer structure, as seen in Figure 5.8b, which keeps the hydrophobic tails separated from the aqueous surroundings on the inside of the structure and the hydrophilic head-groups in contact with the environment on the outside of the lipid bilayer [99]. van der Waals interactions between the hydrocarbon tails of the lipids is what holds them together [41,97].

Lipid bilayers are not rigid, but flexible and in constant motion. This also mean that they can bend, stretch, and rupture in various ways [97]. In nature, lipid bilayers are found in different biomembranes, as already mentioned, and these are more or less spherical in shape. It is most often energetically favourable for lipid bilayers to form different types of enclosures, such as vesicles, as this reduces the energetically unfavourable edge length to a minimum [99]. Vesicles are more or less spherical lipid structures that are formed by lipid bilayers. When they consist of only one layer they are called unilamellar, see Figure 5.8c, but often they consist of several lipid bilayers, making them multilamellar, Figure 5.8d. Artificially made vesicles are also called liposomes.

Vesicles can be used to form lipid bilayers on a surface, so-called supported lipid bilayers (SLBs), by the vesicles adhering to the surface, rupturing, and forming patches of bilayers. These patches will grow as more and more vesicles adheres to the surface, and will eventually form a continuous lipid film [99]. This process is illustrated in Figure 5.8e.

### 5.4.2 Lipid prep

Different lipid mixtures were used for different measurements, but the same general process was used and it is what is described here.

The process from lipids-as-delivered can be divided into three different steps: a) preparation of lipid stock solutions from powders, b) liposome preparation, and c) preparation of small unilamellar vesicles (SUVs). The different steps are described below and is based on the process in [100].

**Lipid stock solutions:** Lipids were bought as powders, from Avanti Polar Lipids, and mixed in different ratios, often mixed with a small portion of dye-labelled lipids, such as Atto 488-DOPE from Atto Tech. Lipid powders were dissolved in chloroform (Sigma-Aldrich) and stock solutions were prepared and diluted, often to a concentration of 10 mg/mL. These now finished lipid stock solutions were stored in glass vessels with teflon sealings, and if not used directly stored at  $-20^{\circ}\text{C}$ .

**Liposome preparation:** To make liposomes form in the lipid stock solution, the chloroform was first removed by rotary evaporating the stock solution using g Büchi Rotavapor R-114. A lipid film was subsequently formed on the bottom of the vessel (such as a test tube or a round flask) where the stock solution was kept. This lipid film is then rehydrated by adding buffer, either PBS buffer (pH 7.4, gibco) or HEPES (7.4 pH) and left overnight to hydrate. Glycerol corresponding to 1 vol% of the total volume of the mixture was then added as a cryoprotectant, after which the mixture was sonicated, yielding predominantly multilamellar vesicles (MLVs). As the liposome preparation now was done, the mixture was aliquoted and stored at  $-20^{\circ}\text{C}$ .

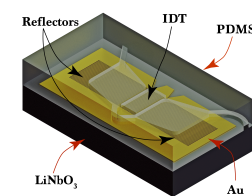
**Preparation of SUVs:** Starting with an already prepared liposome solution of the correct lipid mixture, containing larger MLVs which need to be broken up to form SUVs which can be deposited on a surface and form a SLB. The lipid stock is diluted in the same buffer as the liposomes were prepared in, typically HEPES or PBS, with a lipid:buffer ratio of 1:9. The solution is then sonicated for 10 minutes before it can be extruded, thus breaking up the MLVs into SUVs of a specific size. The extruder is an Avanti Mini Extruder used with Whatman Nucleopore filters with a pore size of  $0.1\ \mu\text{m}$  and a diameter of 19 mm. All parts in the extruder were washed with MilliQ, ethanol, and blow dried with  $\text{N}_2$ -gas before assembly, to remove any traces of old lipids. A minimum of 2 filters were used in the extruder, and a minimum of 11 passes to ensure size uniformity of the SUVs. The SUV lipid solution was then ready to be used in measurements on the sensor.

## 5.5 Sensor characterisation

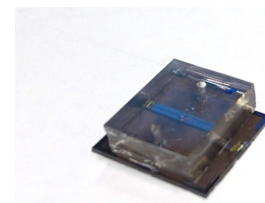
This sensor was designed to utilize technology and material that have already been commercialised for other applications. This is partly the reason for the choice of

basing the sensor design on a SAW resonator rather than the more common two-port delay line setup commonly employed for in-liquid SAW sensors. Another basis for the choice is that the two-port delay line configuration contains too many parameters which might influence the sensor response in addition to strong signal losses when used in liquid.

The finished SAW sensor device is a one-port surface acoustic resonance (SAR) device integrated in a PDMS microfluidic delivery system. A schematic of the sensor device is found in Figure 5.9a. The black portion is the  $\text{LiNbO}_3$  substrate, where Au strips form the SAW resonator. The reflector parts of the resonator are marked out with arrows, as is the IDT. The shaded area shows the PDMS microfluidic system, with the protective air-cavity over the IDT and the sample containers placed over the SAW resonator. A photograph of one finished device is found in Figure 5.9b. The complete PDMS microfluidic delivery system is shown here, with the fluidic in- and outlets. There is a portion of the  $\text{LiNbO}_3$  substrate protruding outside of the PDMS. This is where the electronic contacts (SAW-port) is placed and where the sensor can be connected to the vector network analyser (VNA) that emits the stimulus and detects the sensor response. The complete device in the photo measures around  $15 \text{ mm} \times 15 \text{ mm}$ , with the SAW resonator having a footprint of roughly  $2 \text{ mm}^2$ . The sensor response is measured in the form of the resonance frequency and the magnitude of the conductance peak. These values are obtained from the device conductance, which in turn is derived from the  $S_{11}$  parameters. How this is done can be seen in Equation 4.8.



(a) Schematic of the finished SAW sensor device, from from [21].



(b) Photograph of one finished SAW sensor devices.

**Figure 5.9:** Schematic and photograph of the finished device.

The sensor response is evaluated for different sensor loads. The sensor's ability to detect changes in the viscoelastic properties of solutions is evaluated by loading the sensor with solutions with different (viscosity  $\times$  density) products ( $\rho\eta$ ). To test the sensor's usefulness in bio-chemical measurements, a two-step experiment consisting of coating the sensor surface with a biotin-modified SLB and then loading the sensor with a solution of neutravidin-modified nanoparticles (NPs). The mass loading of the deposited mass was measured. To further evaluate the sensor's performance, the sensor response to SLB transformation caused by  $\text{Ca}^{2+}$  ions was measured.

A photograph of the measurement setup is found in Figure 5.10. The complete setup is placed under a fluorescent microscope. The SAW sensor device is placed on a temperature stage to ensure a controlled temperature during the measurements. The sensor is connected to the VNA (Planar 304/1 3.2 GHz Analyzer, Copper Mountain Technologies) using a set of Picoprobe (Model 40A, GGB Industries Inc.). The

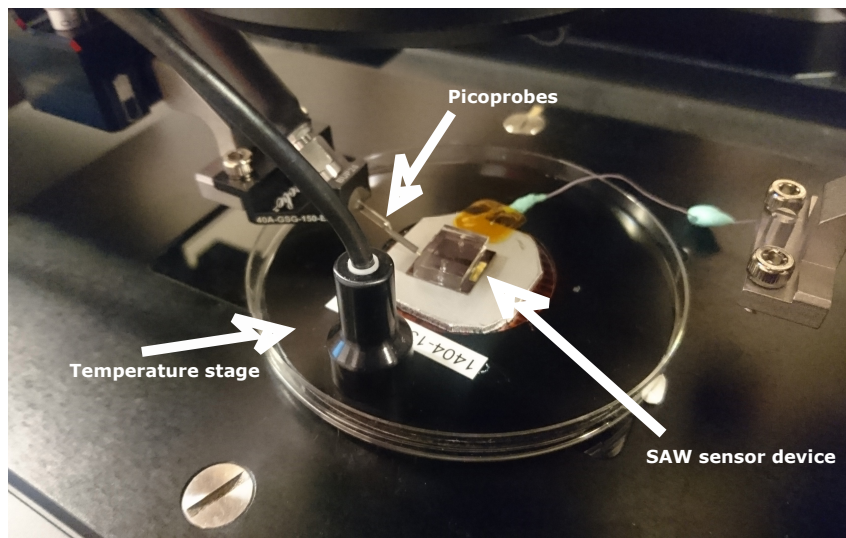


**Figure 5.10:** Photograph of the measurement setup. The setup is placed under a fluorescence microscope on a temperature controlled stage. The SAW sensor device is connected to the VNA by Picoprobes.

sensor device will be loaded with a sample solution of interest, then connected to the VNA and the measurement is made. To measure another sample, the sensor device is disconnected from the VNA, removed from the temperature stage and loaded with the next sample.

Before the sensor device is mounted in the measurement setup and any measurements are made, the setup needs to be calibrated. This is done using a calibration chip with a load of  $50\ \Omega$ . The calibration is done near the resonance frequency of the sensor device for an open circuit, a short-circuited, and for the  $50\ \Omega$  load. The calibration is an additional step, but it will remove the need for some post-processing of data.

The sensor response was evaluated by varying the viscoelastic load on the sensor. This was initially done by loading the sensor with sucrose-PBS solutions containing up to 50% sucrose. A typical measurement consists of measuring the sensor before it is loaded with sample, i.e. containing only air, then measuring the sensor response to MilliQ-water ( $18.2\ \text{M}\Omega$ ), followed by PBS, 10% sucrose in PBS, then by solutions of an increased sucrose content. In a later stage, the sensor response to a varying viscoelastic load was evaluated for MilliQ-glycerol solutions containing up to 50% glycerol. These measurements were time-resolved, measured over a length of time, to estimate the measurement noise. In this case, the sensor would be loaded with MilliQ-water between each glycerol-solution measurement to study the sensor recovery.

The first measurement done to evaluate the sensor's performance for bio-chemical measurements consisted of depositing a biotin-modified SLB on the sensor surface and then loading the sensor with a neutravidin-modified NP solution. This mea-

surement is done in two steps. The first is to measure the sensor response without a load, with buffer (the same buffer as the liposomes were kept in), and finally with a freshly extruded solution of SUVs. The liposome solution was kept in the sensor device for 10 min to allow the liposomes to rupture and spread in the sensor surface, forming a SLB. The excess liposomes were washed away by flushing buffer through the sensor. After this the measurement for the mass loading of the SLB was made. The sensor device was then loaded with a solution of NPs, which were left in the sensor device to allow the neutravidin on the NPs to bind to the biotin on the SLB. The excess NPs were washed away after 10 min by flushing the sensor device with buffer and the measurements were made. These measurements were time-resolved.

The SLB's response to a 5 mmol  $\text{Ca}^{2+}$  solution was measured in a similar way. The sensor response was measured for a null load, buffer, and the SLB after the excess liposomes were washed away. The sensor was loaded with the  $\text{Ca}^{2+}$  solution, which was left in the sensor device for 10 min to allow a reaction to happen between the SLB and the  $\text{Ca}^{2+}$  ions. The  $\text{Ca}^{2+}$  solution was then washed away and the sensor response measured.



# 6

## Results and Discussion

The purpose of this thesis was to use SAW technology to develop, fabricate, and characterise a one-port SAR in-liquid microfluidics integrated sensor. The results of this process are presented in this chapter. In addition, the same technology has also been utilized to fabricate some other types of devices, which are also presented. These findings are also evaluated and discussed.

### 6.1 Results

#### 6.1.1 Sensors

Two different one-port SH-SAW sensors have been developed and characterised. Both are based on the surface acoustic wave resonance (SAR) concept introduced in [8, 101].

Conventionally, a two-port delay line configuration might be used for SH-SAW sensors, with the time delay and phase shift being measured [20]. Unfortunately, this set up is sensitive to significant damping of the SH-SAW when used for in-liquid sensing making it unsuitable for use in chemical or bio-chemical sensing applications. Another option is to use a SH-SAW sensor constructed as a two-port resonator, with a much smaller distance between the two IDTs [63]. This sensor configuration works better for bio-chemical sensing applications than the delay-line approach [63]. The two-port resonator approach is not ideal to be used as an in-liquid sensor, as the consequence of the large transmission losses and that the IDTs can be short-circuited by the liquid conductivity [20].

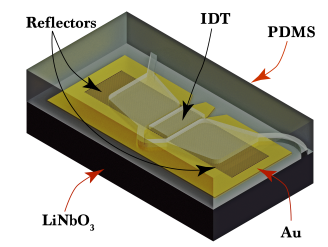


**Figure 6.1:** *Schematic of a one-port SAR microfluidics-integrated device, from [21].*

The sensors in this thesis are based on the SAR concept, which is described in detail in [8]. Both sensors are constructed with a wideband IDT placed at the centre of two reflectors, with no built-in distance between either of them [8]. The IDT emits SH-SAW to the reflectors, which then reflects the waves back to the IDT [8]. The reflectors function as the sensing elements in this setup and the IDT is protected from short-circuiting by the design of the microfluidic delivery system. The

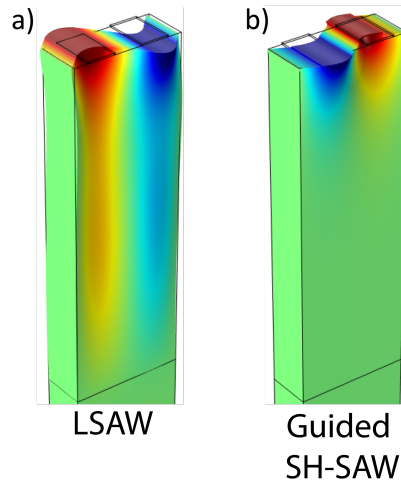


**Figure 6.2:** *FEM simulation of the SAW shear displacement on different substrates. Darker colours indicate larger displacements, with red and blue for positive and negative displacements respectively. (a) LSAW on a free surface on LiNbO<sub>3</sub>, (b) SH-SAW guided by a periodic Au grating on LiNbO<sub>3</sub>. [8]*

delivery system is designed to have a protective air-cavity shielding the IDT from coming into contact with the liquid sample. This approach also makes the IDT/sensor less susceptible to damping in addition to provide more control over the device impedance [20]. Changes in the SH-SAW propagation, such as phase velocity and reflectivity [20], in the reflectors are caused by changes in the mass load or the electric load in this area. The SAR sensor system is illustrated in Figure 6.1.

The piezoelectric substrate material used for these sensors is Y-cut LiNbO<sub>3</sub>. This specific crystal cut can produce both leaky SAW (LSAW) and Rayleigh SAW (RSAW). These different wave types propagate on different axes, the LSAW on the X-axis and the RSAW on the Z-axis [20]. The LSAW propagation direction in particular have an exceptionally high electromechanical coupling coefficient [9], making it possible to construct efficient sensors as most of the energy is converted into LSAW. The RSAW is not suited for in-liquid sensing applications because of its polarization. They can on the other hand be utilized to construct acoustic mixers and other fluid controls for laminar streams in microfluidic circuits.

The LSAW tend to scatter into the bulk of the substrate material. To concentrate the LSAW closer to the substrate surface, making it possible to utilize the energy more efficiently and increase the sensitivity, the strip gratings making up the SAW resonator are made from Au [8]. The Au grating cause the LSAW to slow down, resulting from the poor acoustic velocity in Au, effectively converting the LSAW into surface-guided SH-SAW (Love SAW). A FEM simulation was made using COMSOL to evaluate this and can be found in Figure 6.2.

The first sensor that was fabricated [8] was made up from a 300 nm Ti-Au-Ti metal stack. The strips were  $d = 10\ \mu\text{m}$  wide, which corresponds to an acoustic wavelength  $\lambda = 2d = 20\ \mu\text{m}$  and a resonance frequency  $f_r$  of around 185 MHz. The Ti

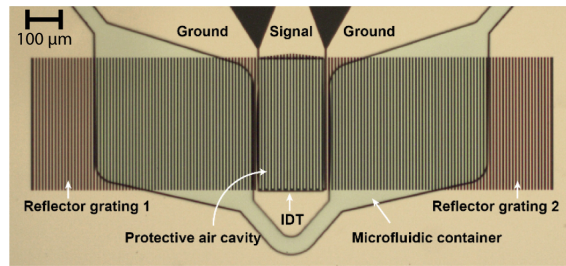


**Figure 6.3:** Optical microscopy image of the SAR sensor without the lateral energy confinement (LEC) design. The SAR sensor is made out of a SAW resonator which has been bonded to the PDMS sample delivery system. The PDMS system has two containers for sample over the resonator and an air cavity about the IDT to protect it from any liquid [8].

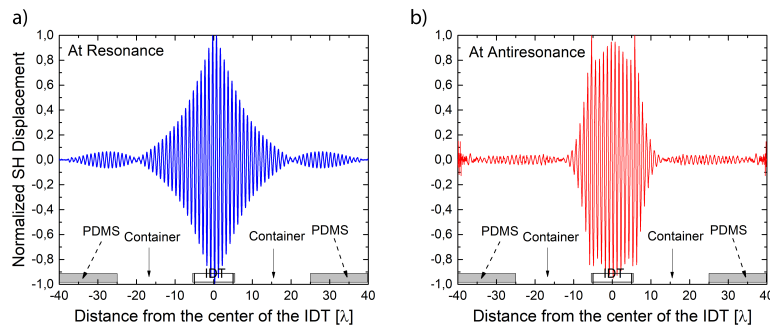


**Figure 6.4:** Simulations of the normalized displacement distributions of SH-SAW at (a) resonance and (b) anti-resonance for  $m=0.5$ . A schematic illustrating where the microfluidic cavities are placed in relation to the the SH-SAW displacements is placed at the bottom of the graph. [101]

in functions both to improve adhesion of the Au on the substrate, and to cap the Au to prevent delamination and improve the adhesion of  $\text{SiO}_2$  to the surface. The Au strips have a metallization ratio  $m = 0.5$ , where  $m = \frac{2w}{p_I}$ . The IDT is made up from 21 Au strips, the reflectors from 69 Au strips each. 49 of each reflector's strips will be overlapping with a microfluidic container and the device aperture is  $40d$ . An image of this sensor is found in Figure 6.3. Graphs describing the SH-SAW distributions of this sensor at resonance and anti-resonance is found in Figure 6.4. It can be seen in Figure 6.4 that the majority of the SH-SAW displacements, i.e. the energy, is located in the IDT both at resonance and anti-resonance.

A FEM simulation of the SH-SAW displacement magnitude of this sensor was made and can be found in Figure 6.5. The resulting simulation, using the same colour as in Figure 6.2, was overlaid with a sketch of the complete SAR sensor.

For the second sensor [101], improvements were made to the resonator design in an attempt to improve the sensitivity of the original SAR-sensor [8]. An area was added to the reflectors close to the IDT to improve the lateral SAW localization in the sensing area. This approach is called *lateral energy confinement* (LEC) [101].

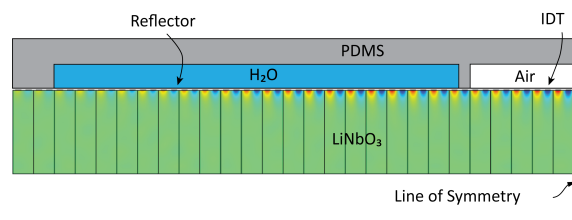


**Figure 6.5:** Schematic combining a FEM simulation of the displacement magnitude of the SH-SAW resonator at resonance and one-half of the SAR-sensor cross section. [8]

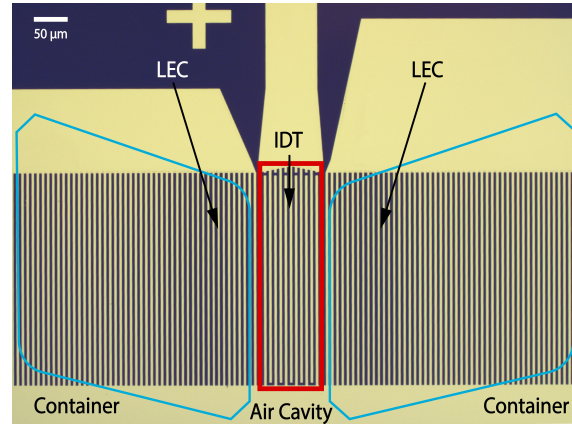


**Figure 6.6:** Optical microscopy image of SAR sensor with lateral energy confinement (LEC) reflector topology. The PDMS sample delivery system is not pictured, but the air cavity is outlined in red and the containers are outlined in blue. [101]

The new design is found in Figure 6.6 and is much the same as the original SAR-sensor and uses the same material and grating pitch, with the addition of a grating area with a different grating (the LEC) on either side of the IDT. The reflectivity in the LECs is lower than in the surrounding reflector, making it possible to concentrate more of the SAW energy in the sensing elements, thus improving sensitivity. The metallization ratio in the reflectors is kept at  $m = 0.5$  as before, except in the LEC regions where it is  $m = 0.4$  and in a transition region between the LEC and the reflectors. The design of the transition from IDT to LEC to reflector can be found in Figure 6.8. The IDTs were kept slightly smaller in this design than in the original SAR-sensor, consisting of 7 pairs of Au strips (14 strips) instead of 21 strips [101]. An image of the simulation of the normalized SH-SAW displacement for the LEC design is found in Figure 6.7 where it is clearly seen that the SH-SAW energy is localised under the microfluidic containers rather than in the IDT at resonance. The SH-SAW energy at anti-resonance is still concentrated in the IDT.

#### 6.1.1.1 Results of experiments: Sensor without LEC

When sample delivery system in the original SAR-sensor was filled with water, a frequency shift of approximately  $-915$  ppm was observed of both the conductance peak and the zero of the admittance. Additionally, the conductance peak magnitude also decreases by about 5%. These shifts are found in Figure 6.9. As can also

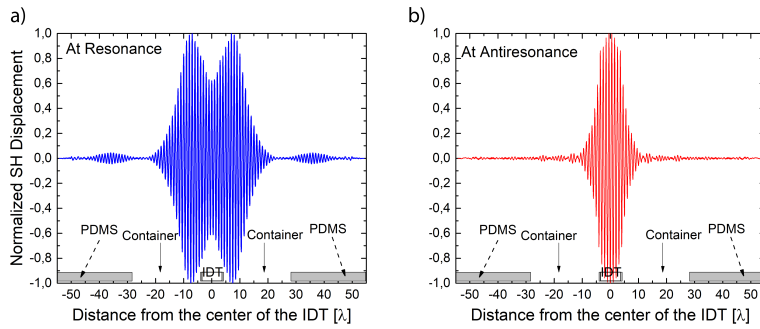


**Figure 6.7:** Simulations of the normalised SH-SAW displacements at (a) resonance and (b) anti-resonance for  $m=0.4$ , i.e. in the LEC overlaid with the layout of the SAR sensor. [101]

**Table 6.1:** SAR sensitivity for different viscous loads, achieved by varying the sucrose-PBS concentrations.

Load	$\Delta f$ (ppm)
Air to MilliQ water	-915
Water to PBS (0% sucrose)	-160
PBS to 20% sucrose	-160
PBS to 40% sucrose	-260
PBS to 50% sucrose	-260

be seen from Figure 6.9, the measured conductance at resonance is approximately  $0.125 \Omega^{-1}$ , corresponding to a low impedance of  $8 \Omega$  at resonance, making it possible to match it to  $50 \Omega$ . Q of the device decrease somewhat when it was loaded with water, from 300 to 250.

The sensor was characterised by varying the (viscosity  $\times$  density) product ( $\rho\eta$ ) by measuring the sensor response to different sucrose and phosphate buffer saline (PBS) solutions. The solutions contained between 0% and 50% sucrose. The frequency shifts of the conductance at resonance are summarised in Table 6.1. The frequency shift from air to PBS was close to  $-1080$  ppm, with an additional shift of  $-450$  ppm for the sucrose solutions. To summarise, the frequency kept shifting downwards with an increased sucrose content in the solutions. The magnitude of the conductance at resonance stayed within 4.5% of the value for PBS even for the 50% sucrose solution. The total damping caused by the solutions on the sensor was in the range of 2%.

One of the intended uses of the SAR-sensor is for chemical and bio-chemical measurements. To evaluate if the sensor can detect biomolecule interactions the following two-step experiment was performed at  $21^\circ \text{C}$ . In the first step, biotin modified supported lipid bilayers (SLBs) were deposited on the sensor area. For the second step, neutravidin-coated nanoparticles (NPs) in aqueous solution were deposited on the sensor area. The neutravidin on the NPs bonded with the biotin in the SLBs by an affinity reaction, in this way increasing the mass load on the sensor. The assay is illustrated in Figure 6.10.

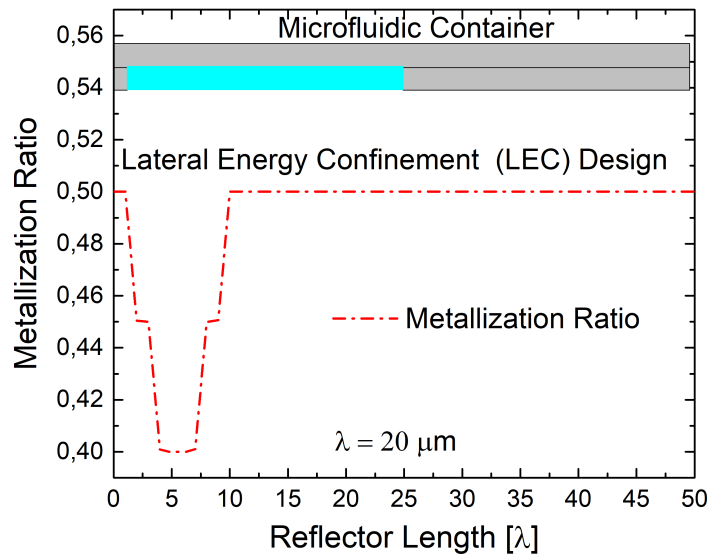


**Figure 6.8:** The top section shows a schematic of part of the delivery system of the SAR-sensor, while the bottom section shows how the metallization ratio varies over the device [101].

SLBs are, as was mentioned earlier, a good model system for biological membrane. In addition, they are also well suited to evaluate sensors owing to the small mass loading they can provide, ease of deposition, and properties which depend on both lipid composition and chemical environment [20].

A typical sensor measurement involving SLBs was outlined in Section 5.5. This two-step experiment is a variation of the one described in Section 5.5. The sensor was initially loaded with MilliQ water (MQW, 18.2 MΩ), which was exchanged for a buffer (PBS or HEPES). The system was then loaded with a suspension of SUVs in PBS, which was left for long enough for the vesicles to rupture and spread on the sensor surface. The excess of liposomes were then washed away by once again loading the sensor with PBS. The last step was to add the solution of NPs in PBS. Every step of this process was monitored by the SAR-sensor system, with shifts of frequency and magnitude of conductance being recorded and summarised in Table 6.2. The same measurements were also made with HEPES instead of PBS, see Table 6.3. The spreading of SLB and the bonding of NPs to SLB was verified by using a membrane-incorporated dye (ATTO-488 with Absorption/Emission at 500/520 nm) in the lipid sample and adding fluorescent latex beads (Absorption/Emission 580/604 nm) to the nanoparticle sample and then image the sensor using fluorescence microscopy, see Figure 6.11.

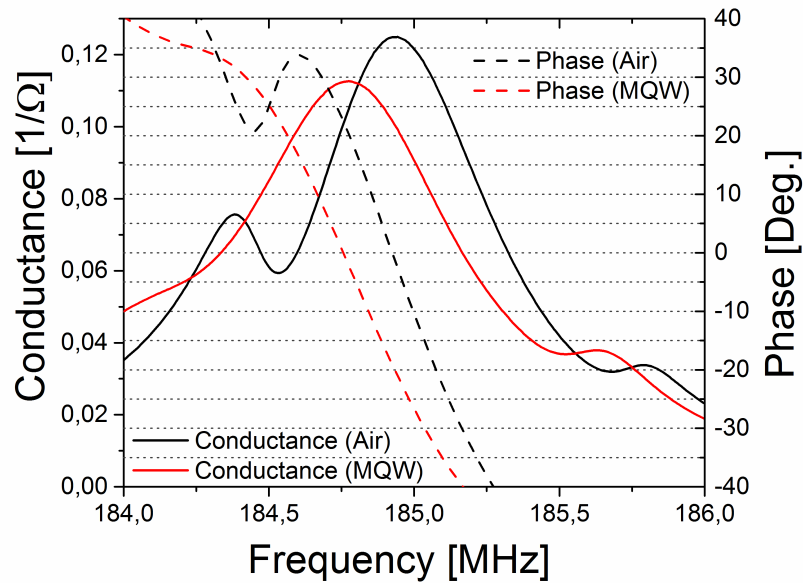


**Figure 6.9:** The phase (dashed graphs) and the conductance (solid graphs) of the SAR-sensor when the microfluidic containers are filled with air (black graphs) or MilliQ-water (MQW) (red graphs). [21]

#### 6.1.1.2 Results of experiments: Sensor with LEC

The performance of the SAR-sensor with LEC under a water load was evaluated by measuring the admittance (the inverse of the conductance) and the resistance in air and in water. The results of these measurements are found in Figure 6.12. The admittance is measured at the resonance frequency and the resistance at the anti-resonance frequency. The shift in the admittance peak under this load was found to be around  $-2200$  ppm, which corresponds to the shift in the conductance peak. The admittance (conductance) peak magnitude decreased by 27 %. At the anti-resonance frequency, the frequency shift of the resistance was around  $-910$  ppm, which is less than half of the same value at resonance.

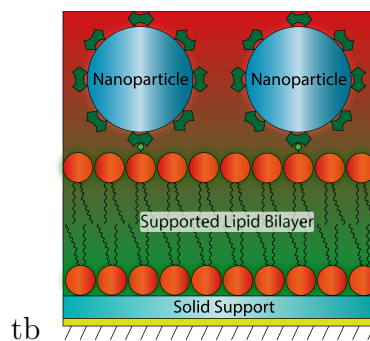


**Figure 6.10:** Schematic of the assay consisting of a supported lipid bilayer with biotin and neutravidin-coated nanoparticles [101].

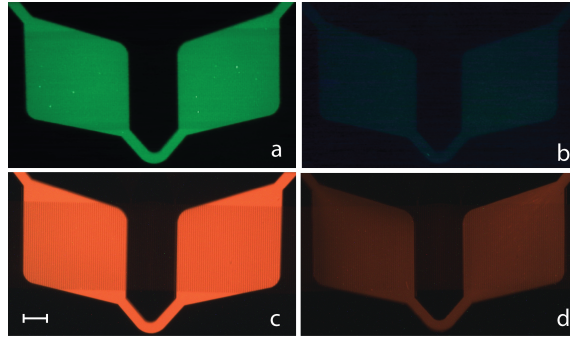


**Figure 6.11:** (a)-(b) Fluorescent microscopy images (ATTO-488) of the sensor loaded with MLV solution before washing (a) and after washing (b). The fluorescence after washing is weak but its presence indicates that the SLB has spread on the sensor surface. (c)-(d) Fluorescence microscopy images (Nile red) of the sensor loaded with NP solution before washing (c) and after washing (d), indicating the presence of NPs. The scale bar is 100  $\mu\text{m}$ . [8]

**Table 6.2:** SAR sensitivity [8] to deposition of an SLB and NPs.

Load	$\Delta f$ (ppm)	$\Delta G$
Air to MilliQ water (MQW)	-915	-5%
MQW to PBS	-160	-1%
PBS to SLB	-65	0%
SLB to SLB/NPs	-90	+2%

The SAR-sensor with LEC was then characterised in the same way as the original SAR-sensor, without LEC. The (viscosity $\times$ density) product  $\rho\eta$  was varied in the same way and the two-step experiment with the SLB-NP biotin-neutravidin affinity assay was repeated for this sensor. Figure 6.13 and in Table 6.4 . The results of the affinity assay experiment are summarised in Table 6.5.

The sensor response to the different loads were also monitored over time, in order to obtain time-resolved data and measure the recovery of the sensor. The time-resolved response for the different viscous loads, using glycerol in MilliQ, is found in Figure 6.14 and for the affinity assay in HEPES in Figure 6.15. It can be clearly seen in Figure 6.14 and that the sensor recovers after each measurement as the frequency recovers to the same approximate level after it has been filled with water after each glycerol solution measurement. The measurements in Figures 6.14 and fig:SAR2-time-viscous makes it possible to estimate the noise level using the Allan deviation  $\sigma_y$ . The Allan deviation was calculated from 200 consecutive measurements with

**Table 6.3:** SAR device sensitivity for different loads of SLB and NPs. Note that the buffer used here was HEPES. [20]

Load	$\Delta f$ (ppm)	$\Delta G$
HEPES to SLB	-65	0%
SLB to SLB/NPs	-90	+2%

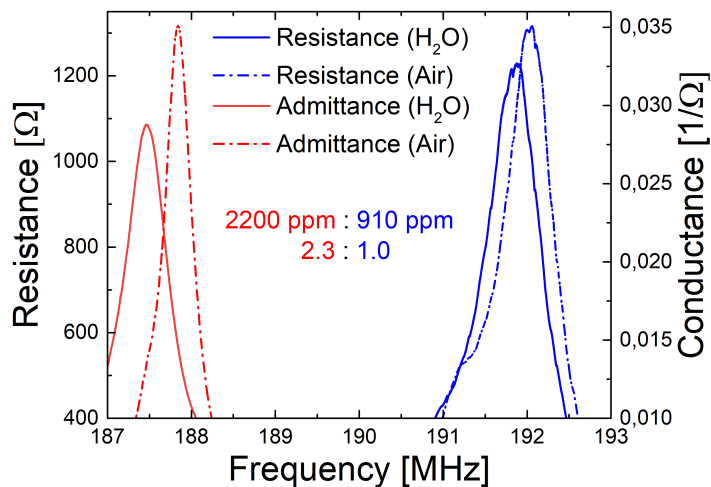


**Figure 6.12:** The performance of the SAR-sensor with LEC under a water load. The admittance (conductance) (red) is measured at resonance and the resistance (blue) at anti-resonance. [101]

**Table 6.4:** SAR sensitivity for different viscous loads for the SAR-sensor with LEC [101].

Load	$\Delta f$ (ppm)
Air to MilliQ water	-2200
Water to PBS (0% sucrose)	-315
PBS to 20% sucrose	-220
PBS to 40% sucrose	-600
PBS to 50% sucrose	-960

$\tau=3$ s for a total of 10 min for each  $\sigma_t$ . The measured magnitudes of the conductance peak were fitted to a 5<sup>th</sup> order polynomial and  $\sigma_t$  was determined from the fitted data.  $\sigma_t$  was determined to be less than 0.5 ppm at resonance frequencies and less than 10 ppm for the conductance peak. These numbers are used to determine the LOD for frequencies ( $\Delta f$ ) to  $3\sigma_t < 1.5$  ppm and LOD for conductance ( $\Delta G$ ) magnitude to  $3\sigma_t < 30$  ppm.

The SAR-sensor was used to measure changes in the SLB caused by the chemical environment.  $\text{Ca}^{2+}$  ions can bind to negatively charged phospholipids [20], which might lead to several different changes in the SLB. One such change would be the formation of nanotubes [102] which would cause some of the lipid material to be removed from the sensor surface, leading to a decrease in the mass loading on the surface and to a frequency shift [20]. Exposure of the SLB to  $\text{Ca}^{2+}$  might increase the rigidity of the SLB.

The SLB was exposed to a 5 mM  $\text{Ca}^{2+}$  after it had been deposited in the sensor surface. The time-resolved sensor response is found in Figure 6.16. The  $\text{Ca}^{2+}$  exposure caused a frequency shift of about +20 ppm together with a conductance peak

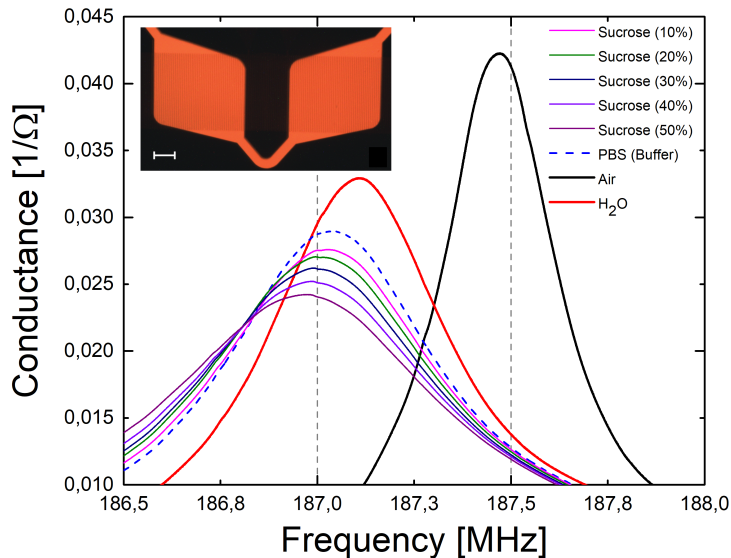


**Figure 6.13:** The performance of the SAR-sensor with LEC under a viscous load. [101]

**Table 6.5:** Mass and conductance sensitivity for different loads in the SLB-NP biotin-neutravidin affinity assay. Note that the buffer used was HEPES, not PBS. [101]

Load	$\Delta f$ (ppm)	$\Delta G$
Air to MilliQ water (MQW)	-2200	-27%
MQW to HEPES	-315	-2%
HEPES to SLB	-130	-2%
SLB to SLB/NPs	-160	+2%

shift of +2% compared to the values of the SLB.

### 6.1.2 Adhesive bonding

A method for bonding microfluidic devices to substrates using UV-curable PDMS in air and in water has been developed and evaluated. The adhesive bonding procedure is in part based on the stick-and-stamp bonding introduced by [95,96].

Different tests were performed to establish some bonding characteristics of the UV-PDMS and to determine the optimal bonding procedure, with focus on the bonding in water. Both PDMS (Dow-Corning Sylgard 184 PDMS) and the UV-PDMS (Shin-Etsu KER-4690) [94] were found to be curable in water. The exposure dose required to photoactivate the catalyst in the UV-PDMS is 2000 mJ/cm<sup>2</sup>. Overexposure will occur at exposure doses over 10000 mJ/cm<sup>2</sup> and will lead to the destruction of the catalyst and the UV-PDMS will not cure. Several tests were made to establish the optimal exposure time in air and in water, with the UV-PDMS used on its own or as an adhesive layer between cured PDMS-pieces and glass substrates. The UV-PDMS

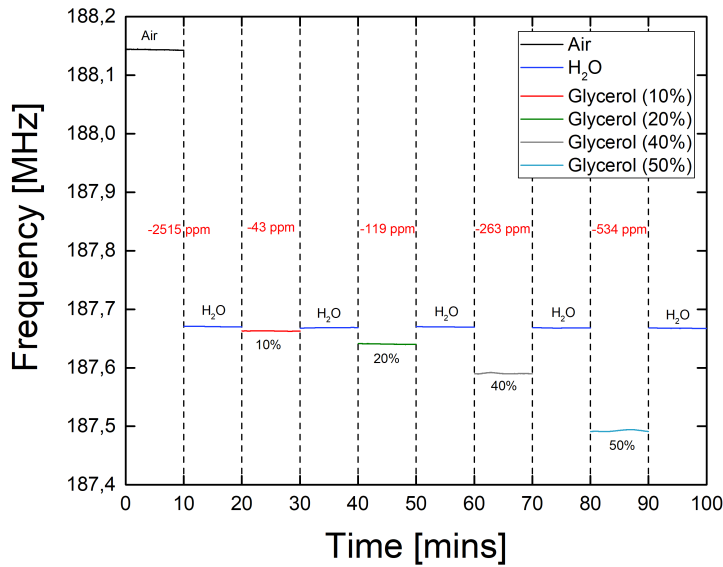


**Figure 6.14:** *The time-resolved response of the SAR-sensor with LEC for varying viscous loads. The different  $\rho\eta$  values were obtained by varying the glycerol content in MilliQ. Frequency shifts between the different loads are indicated in red. [101]*

seems to require different exposure doses depending on the environment it was kept in, as well as depending on whether it was used as an adhesive layer or not. Interestingly, for some exposure times the UV-PDMS seemed to cure to be harder when it was kept in water than in air. The curing behaviour of the UV-PDMS was found to be quite erratic.

Different exposure times were tested in air and water in combination with different curing conditions (at room temperature or at 100 °C for 10 min). The curing and bonding of the UV-PDMS were evaluated 3 h after exposure, the quality of UV-PDMS as an adhesive layer was evaluated by ripping off the PDMS pieces from the glass slides. The samples cured more consistently in this test than before, regardless of whether they were cured at room temperature or at 100 °C. The PDMS pieces that had been bonded to glass slides with UV-PDMS as an adhesive layer were attached well enough to break, i.e. the cured PDMS broke rather than the UV-PDMS layer, when ripped apart.

A few functioning microfluidic devices were bonded to glass slides with UV-PDMS as an adhesive layer, with the aim of determining if the bond was good enough to allow for a mix of water and food dye to be flowed through the channels. This was not successful, as the liquid either leaked through the UV-PDMS bond or because the microfluidic channels had been clogged by UV-PDMS. Another difficulty was that cured PDMS floats in water, causing difficulties to bond them to a glass substrate in water.

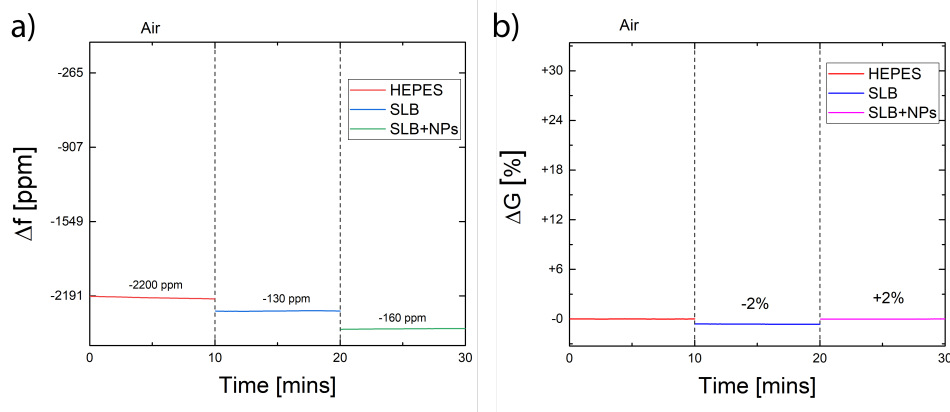


**Figure 6.15:** Time-resolved responses of frequency shift (a) and the peak conductance magnitude shift (b) for the SAR-sensor with LEC for the SLB-deposition and the SLB-NP biotin-neutravidin affinity-assay reaction. [101]

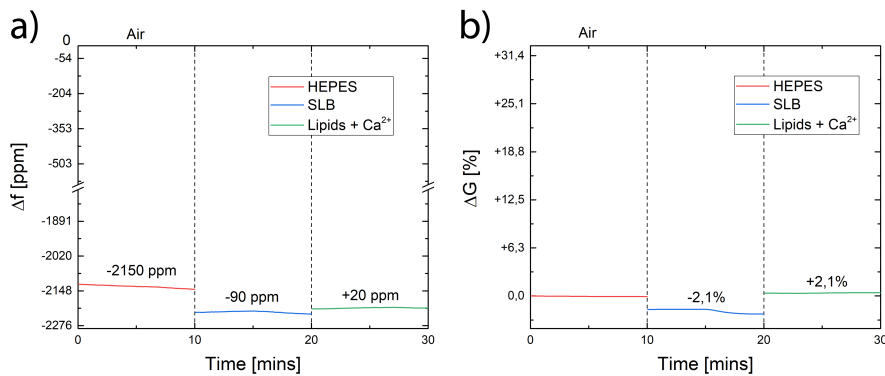


**Figure 6.16:** The time-resolved sensor response of when the SLB is exposed to  $Ca^{2+}$ . (a) the frequency shift and (b) peak conductance magnitude shift. [101]

## 6.2 Discussion

### 6.2.1 Sensors

The sensitivity of the SAR sensor was improved by the addition of the LEC region in the resonator design. This can be seen by comparing the sensitivities of the two different sensors which are found in Table 6.1 for the sensor without LEC and in Table 6.4. The contents of these tables have been combined in Table 6.6 to make the comparison easier.

The addition of the LEC region made the sensor about two times more sensitive, as is seen by comparing the frequency shifts of the two different sensors in Table 6.6. The frequency shift of  $-2200$  ppm between air and water for the sensor is close to the estimated maximal theoretical sensitivity of  $-2100$  ppm [8,101]. These shifts are found in Figure 6.13 for the sensor with LEC. What is also observable in this figure is how the magnitude of the conductance peak decreases with an increased viscosity of the sample. The maximum decrease of the conductance peak is only

**Table 6.6:** *The sensitivity of the SAR sensor with and without LEC. [8, 101]*

Load	SAR-sensor <i>without</i> LEC $\Delta f$ (ppm)	SAR-sensor <i>with</i> LEC $\Delta f$ (ppm)
Air to MilliQ water	-915	-2200
Water to PBS (0% sucrose)	-160	-315
PBS to 20% sucrose	-160	-220
PBS to 40% sucrose	-260	-600
PBS to 50% sucrose	-450	-960

**Table 6.7:** *SAR-sensor sensitivity for SLB-NPs reactions in HEPES [8, 101]*

Load	SAR-sensor <i>without</i> LEC $\Delta f$ (ppm)/ $\Delta G$	SAR-sensor <i>with</i> LEC $\Delta f$ (ppm)/ $\Delta G$
HEPES to SLB	-65/0%	-130/-2%
SLB to SLB/NPs	-90/+2%	-160/+2%

-17% however for the 50% sucrose solution, meaning that the sensor can tolerate viscous damping well [101].

The increased sensitivity in the sensor with LEC stresses the importance of the localisation of the SH-SAW energy in the sensing area to achieve maximal sensitivity. A similar comparison can be made by the sensors' performance in the SLB-NPs measurements. The data from Tables 6.3 and 6.5 into Table 6.7 below. Large frequency shifts were observed when the sensors were loaded with water and buffer, which are found in Table 6.2 and 6.5. The deposition of a SLB on the sensor surface leads to a downshift in frequency for both sensors, see Table 6.7, as well as a downshift in conductance peak magnitude for the sensor with LEC. These shifts can be explained by the fact that the deposited lipid layer increases the mass on the sensor as the viscosity in the direct proximity to the sensor surface. However, for SAW sensors, a frequency downshift is not always correlated with a shift in the conductance peak magnitude [101]. The deposition of the NPs on the SLB caused a further frequency downshift accompanied by a conductance peak upshift. The upshift in  $\Delta G$  could indicate increased rigidity of the SLB.

The response of the SLB after exposure to  $\text{Ca}^{2+}$  was detected by the sensor with LEC and is recorded in Figure 6.16. The  $\text{Ca}^{2+}$  caused a small frequency upshift along with an upshift in the conductance peak magnitude. The frequency response of the sensors to the SLB was a downshift, which might indicate that the mass loading on the sensor surface is decreased. This is in agreement the formation of nanotubes from some of the lipid material in the SLB caused by the addition of  $\text{Ca}^{2+}$ . The upshift in conductance peak magnitude might indicate an increased rigidity of the SLB remaining on the sensor surface, similar to what happened after the NPs

attached to the SLB.

### **6.2.2 Adhesive bonding**

Although the UV-PDMS could cure in and out of water, there were several difficulties with this process. The curing behaviour of the UV-PDMS, both in air and in water, was somewhat erratic. This is especially the case for UV-PDMS when used as an adhesive later between a glass slide and a cured PDMS piece.

Precise alignment of microfluidic PDMS devices was difficult both in air and in water. In both environments this could be caused by the stick-and-stamp bonding procedure, which requires the microfluidic device to be stamped into a spin-coated layer of uncured UV-PDMS and then placed on the substrate without clogging the channels with UV-PDMS. In water, precise alignment was further complicated by the buoyancy of cured PDMS.

# 7

## Conclusion and Outlook

This thesis has described a one-port shear-horizontal surface acoustic wave sensor system with an integrated microfluidic sample delivery system utilizing the concept of surface acoustic resonance (SAR). This sensor system has a resonance frequency of roughly 185 MHz, low impedance at resonance, low susceptibility to viscous damping, and a Q-value of 250 in water. The sensor has been experimentally tested and the results have been evaluated. The sensitivity of the sensor is close to the value that has been theoretically estimated.

Two different iterations of the same sensor have been presented in this thesis. The original resonator was redesigned to include a lateral energy confinement (LEC) region which allows the acoustic energy to be concentrated more precisely in the sensor area, leading to an increased sensitivity of the sensor.

Both sensors were tested with solutions of varying viscosity, to evaluate their performance under a varying viscous load. The response of the sensors to a supported lipid bilayer-nanoparticle (SLB-NP) assay has been recorded to evaluate the sensors' ability to detect mass loading. For the second iteration of the sensor, the ability of the sensor to detect conformational changes to the SLB after the addition of a  $\text{Ca}^{2+}$  solution was assessed.

One possibility for a next step is to develop a device set-up which allows for on-chip sample switching. This combined with the high sensitivity of the sensor would open the possibility to extend the time-resolved study of SLBs to include the measurement of spreading behaviour and reaction dynamics in real time. The present sensor set-up does not allow for on-chip sample switching, making it difficult to load the solution in the sensor and mount it in the VNA in a suitable time frame.

Another possibility would be to evaluate the sensors response to different types of macromolecules and bio-chemical assays.

The design of the sensor combined with the many different applications of SAW technology that already exists makes integrating the two in the same device possible. This has already been done, by integrating electrochemical impedance spectroscopy (EIS) with the SAR sensor as was recently demonstrated in [103], proving that it is possible to have several different sensors in the same SAW device. Another option would be to integrate some type of antenna device in the sensor to enable wireless read-out of the sensor response.

The use of RSAW to manipulate microfluidic fluid flows for mixing, separation, or acoustic trapping could be incorporated on the same chip as the sensor, since both LSAW used for sensing and RSAWs exist on the same Y-cut LiNbO<sub>3</sub> substrate. The RSAW can be used together with the sensor for sample preparation to get one step closer to a fully integrated lab-on-a-chip.

A method for bonding microfluidic devices to substrates in air or in water by using UV-PDMS as an adhesive layer has been developed and evaluated. It was not used in the bonding of the sensor devices. Although this method works, there are several difficulties that need to be addressed. The clogging of the microfluidic channels combined with the difficulties of obtaining a good alignment makes it impractical as a bonding method for microfluidic devices, especially if a precise alignment between the substrate and the microfluidic device is required. Unless the plasma bonding method is unsuitable, it is much easier to use than the adhesive bonding method with UV-PDMS. The covalent bonds obtained from plasma bonding are probably much stronger than the bond between UV-PDMS, substrate, and microfluidic PDMS device. This in combination with an easier bonding procedure makes plasma bonding more useful in many applications than the adhesive bonding procedure.

In conclusion, an acoustic sensor based on the SAR concept has been developed and proved to be sensitive to both the viscoelastic properties of the sample as well as to mass loading on its surface. It has the potential to be integrated with several different SAW and microfluidic technologies, making it one step closer to a fully integrated lab-on-a-chip sensing device.

# Bibliography

- [1] D. Knaack, “Photographic depth of field,” <http://omahamakergroup.org/2014/02/22/photographic-depth-of-field/>, 2014, [Online] Accessed on: 2019-01-15.
- [2] C. Kittel and P. McEuen, *Introduction to Solid State Physics*, 8th ed. Hoboken, N.J: Wiley, 2005.
- [3] E. D. Daniel Royer, *Elastic Waves in Solids I: Free and Guided Propagation*. Springer, 2000, vol. 1.
- [4] C. K. Campbell, *Surface acoustic wave devices for mobile and wireless communications.*, ser. Applications of Modern Acoustics. San Diego: Academic Press, 1998.
- [5] S. Shiokawa and J. Kondoh, “Surface acoustic wave sensors.” *Japanese Journal of Applied Physics, Part 1: Regular Papers and Short Notes and Review Papers*, vol. 43, no. 5 B, pp. 2799–2802, 2004.
- [6] D. Ballantine, R. White, S. Martin, A. Ricco, E. Zellers, G. Frye, and H. Wohltjen, *Acoustic Wave Sensors: Theory, Design, and Physico-Chemical Applications*, 1st ed., ser. Application of Modern Acoustics. San Diego: Academic Press, 1997.
- [7] Wikimedia Commons, “Quartz resonators with front and back electrodes,” <https://commons.wikimedia.org/w/index.php?curid=3500612>, 2008, [Online] Accessed on: 2018-12-10. CC-BY-3.0.
- [8] K. Kustanovich, V. Yantchev, V. Kirejev, G. D. M. Jeffries, T. Lobovkina, and A. Jesorka, “A high-performance lab-on-a-chip liquid sensor employing surface acoustic wave resonance.” *JOURNAL OF MICROMECHANICS AND MICROENGINEERING*, vol. 27, no. 11, 2017.
- [9] K.-y. Hashimoto, *Surface Acoustic Wave Devices in Telecommunications. [electronic resource] : Modelling and Simulation*. Berlin, Heidelberg : Springer Berlin Heidelberg : Imprint: Springer, 2000., 2000.
- [10] Y. V. Gulyaev, “Review of shear surface acoustic waves in solids.” *IEEE Transactions on Ultrasonics, Ferroelectrics and Frequency Control*, no. 4, p. 935, 1998.
- [11] D. Royer and E. Dieulesaint, *Elastic waves in solids II: Generation, Acousto-optic Interaction, Applications*. Springer, 2000, vol. 2.
- [12] X. Ding, P. Li, S.-C. S. Lin, Z. S. Stratton, N. Nama, F. Guo, D. Slotcavage, X. Mao, J. Shi, F. Costanzo, and T. J. Huang, “Surface acoustic wave microfluidics,” *Lab on a Chip - Miniaturisation for Chemistry and Biology*, vol. 13, no. 18, pp. 3626–3649, 2013.

- [13] T. Nagayama, J. Kondoh, T. Oonishi, and K. Hosokawa, “Measurement of Plasma Clotting Using Shear Horizontal Surface Acoustic Wave Sensor.” *JAPANESE JOURNAL OF APPLIED PHYSICS*, vol. 52, no. 7, 2013.
- [14] J. Kondoh, “A liquid-phase sensor using shear horizontal surface acoustic wave devices.” *Electronics & Communications in Japan*, vol. 96, no. 2, pp. 41 – 49, 2013.
- [15] G. C. King, *Vibrations and Waves*. Wiley, 2009.
- [16] A. Hirose and E. Lonngren Karl, *Fundamentals of Wave Phenomena (2nd Edition)*. Institution of Engineering and Technology, 2017.
- [17] S. J. Rupitsch, *Piezoelectric Sensors and Actuators : Fundamentals and Applications.*, ser. Topics in Mining, Metallurgy and Materials Engineering. Springer, 2019.
- [18] D. P. Morgan, *Surface Acoustic Wave Filters : With Applications to Electronic Communications and Signal Processing.*, ser. Studies in Electrical and Electronic Engineering. Academic Press, 2007, vol. 2nd ed.
- [19] K. Kustanovich, *Surface acoustic wave devices for liquid-phase sensing.*, ser. Licentiatuppsatser vid Institutionen för kemi och kemiteknik, Chalmers tekniska högskola: 2017:20. Göteborg : Chalmers University of Technology, 2017., 2017.
- [20] —, *Integration of Surface Acoustic Wave and Microfluidic Technologies for Liquid-Phase Sensing Applications*, ser. Doktorsavhandlingar vid Chalmers tekniska högskola. Ny serie: 4583. Göteborg : Chalmers University of Technology, 2019.
- [21] K. Kustanovich, V. Yantchev, and A. Jesorka, “Design and characterization of surface acoustic wave resonance (sar) system for in-liquid sensing,” in *2017 Joint Conference of the European Frequency and Time Forum and IEEE International Frequency Control Symposium (EFTF/IFCS)*, July 2017, pp. 652–655.
- [22] A. Butterfield and J. E. Szymanski, *A dictionary of electronics and electrical engineering. [electronic resource].*, ser. Oxford quick reference. [Oxford] : Oxford University Press, 2018., 2018.
- [23] K. Nakamura, “Shear-horizontal piezoelectric surface acoustic waves.” *Japanese Journal of Applied Physics, Part 1: Regular Papers and Short Notes and Review Papers*, vol. 46, no. 7 B, pp. 4421–4427, 2007.
- [24] K. Hashimoto and H. Yamaguchi, “Excitation and propagation of shear-horizontal-type surface and bulk acoustic waves,” *IEEE Transactions on Ultrasonics, Ferroelectrics and Frequency Control*, vol. 48, no. 5, pp. 1181–1188, 2001.
- [25] T. Morita, M. Sugimoto, and J. Kondoh, “Measurements of standard-viscosity liquids using shear horizontal surface acoustic wave sensors.” *JAPANESE JOURNAL OF APPLIED PHYSICS*, vol. 48, no. 7, 2009.
- [26] W. Jakubik, “Surface acoustic wave-based gas sensors.” *Thin Solid Films*, vol. 520, no. 3, pp. 986–993, 2011.
- [27] M. Yamaguchi, “Early days of sh-type surface acoustic wave research.” *Japanese Journal of Applied Physics, Part 1: Regular Papers and Short Notes and Review Papers*, vol. 42, no. 5 B, pp. 2909–2917, 2003.

- 
- [28] F. K. Balagadde, L. You, C. L. Hansen, F. H. Arnold, and S. R. Quake, “Long-term monitoring of bacteria undergoing programmed population control in a microchemostat.” *Science*, no. 5731, p. 137, 2005.
- [29] D. Orenstein, “‘Microfluidic’ chips may accelerate biomedical research,” <https://news.stanford.edu/news/2006/january18/fluidics-011806.html>, 2006, [Online] Accessed on: 2019-01-13.
- [30] G. M. Whitesides, “The origins and the future of microfluidics,” *Nature*, vol. 442, no. 7101, pp. 368–373, 2006.
- [31] P. S. Dittrich and A. Manz, “Lab-on-a-chip: microfluidics in drug discovery.” *NATURE REVIEWS DRUG DISCOVERY*, no. 3, p. 210, 2006.
- [32] A. Manz, N. Graber, and H. Widmer, “Miniaturized total chemical analysis systems: A novel concept for chemical sensing,” *Sensors and Actuators B: Chemical*, vol. 1, no. 1-6, pp. 244–248, jan 1990.
- [33] D. E. W. Patabadige, S. Jia, J. Sibbitts, J. Sadeghi, K. Sellens, and C. T. Culbertson, “Micro total analysis systems: Fundamental advances and applications.” *Analytical chemistry*, no. 1, p. 320, 2016.
- [34] W. Jung, J. Han, J.-W. Choi, and C. H. Ahn, “Review article: Point-of-care testing (poc) diagnostic systems using microfluidic lab-on-a-chip technologies.” *Microelectronic Engineering*, vol. 132, no. Micro and Nanofabrication Breakthroughs for Electronics, MEMS and Life Sciences, pp. 46 – 57, 2015.
- [35] D. Mark, S. Haeberle, G. Roth, F. vonStetten, and R. Zengerle, “Microfluidic lab-on-a-chip platforms: requirements, characteristics and applications.” *CHEMICAL SOCIETY REVIEWS*, no. 3, p. 1153, 2010.
- [36] A. Rios, M. Zougagh, and M. Avila, “Review: Miniaturization through lab-on-a-chip: Utopia or reality for routine laboratories? a review.” *Analytica Chimica Acta*, vol. 740, pp. 1 – 11, 2012.
- [37] H. Bruus, *Theoretical microfluidics.*, ser. Oxford master series in physics: 18 Condensed matter physics. Oxford : Oxford University Press, 2008., 2008.
- [38] A. Ghosh and B. Corves, *Introduction to Micromechanisms and Microactuators.*, ser. Mechanisms and Machine Science: 28. New Delhi : Springer India : Imprint: Springer, 2015., 2015.
- [39] J. R. Welty, C. E. Wicks, R. E. Wilson, and G. L. Rorrer, *Fundamentals of Momentum, Heat, and Mass Transfer*, 5th ed. John Wiley & Sons Inc., 2008.
- [40] E. Iannone, *Labs on Chip: Principles, Design and Technology*, 1st ed. CRC Press, 10 2014.
- [41] A. Ainla, *The multifunctional pipette : a microfluidic technology for the biosciences.*, ser. Doktorsavhandlingar vid Chalmers tekniska högskola. Ny serie: 3499. Göteborg : Chalmers University of Technology, 2013.
- [42] J. P. Lafleur, A. Jönsson, S. Senkbeil, and J. P. Kutter, “Recent advances in lab-on-a-chip for biosensing applications.” *Biosensors and Bioelectronics*, vol. 76, no. 30th Anniversary Issue, pp. 213 – 233, 2016.
- [43] F. Lung-Ming, C. Chin-Lung, W. Yao-Nan, and L. Chia-Yen, “Microfluidic mixing: A review.” *International Journal of Molecular Sciences, Vol 12, Iss 5, Pp 3263-3287 (2011)*, no. 5, p. 3263, 2011.

- [44] X. Niu and Y.-K. Lee, “Efficient spatial-temporal chaotic mixing in microchannels.” *JOURNAL OF MICROMECHANICS AND MICROENGINEERING*, no. 3, p. 454, 2003.
- [45] W. Christoph, S. Lukas G., W. Dominik, K. Rafał, L. Ulrich, W. Ernst, R. Joachim O., and W. Achim, “Controllable acoustic mixing of fluids in microchannels for the fabrication of therapeutic nanoparticles.” *Micromachines, Vol 7, Iss 9, p 150 (2016)*, no. 9, p. 150, 2016.
- [46] M. Wiklund, R. Green, and M. Ohlin, “Acoustofluidics 14: Applications of acoustic streaming in microfluidic devices.” *LAB ON A CHIP*, no. 14, p. 2438, 2012. [Online]. Available: <http://proxy.lib.chalmers.se/login?url=http://search.ebscohost.com/login.aspx?direct=true&db=edsbl&AN=RN314203390&lang=sv&site=eds-live&scope=site>
- [47] M. Evander and J. Nilsson, “Acoustofluidics 20: Applications in acoustic trapping.” *LAB ON A CHIP*, no. 22, p. 4667, 2012.
- [48] H. Bruus, “Acoustofluidics 7: The acoustic radiation force on small particles.” *LAB ON A CHIP*, vol. 12, no. 6, pp. 1014 – 1021, 2012.
- [49] I. Nathan, *Sensors, actuators, and their interfaces. [electronic resource] : a multidisciplinary introduction*. Edison, NJ : SciTech Publishing, 2014, ebook.
- [50] T. Kenny, “Sensor fundamentals,” in *Sensor Technology Handbook.*, J. S. Wilson, Ed. Burlington, Mass. : Newnes, cop. 2005., 2005, ch. 1, pp. 1–20, ebook.
- [51] International Union of Pure and Applied Chemistry, “Limit of detection,” in *IUPAC Compendium of Chemical Terminology*, 19 October 2018. [Online]. Available: <https://goldbook.iupac.org/html/L/L03540.html>
- [52] —, “Accuracy,” in *IUPAC Compendium of Chemical Terminology*, 19 October 2018. [Online]. Available: <https://goldbook.iupac.org/html/A/A00060.html>
- [53] B. R. Eggins, *Chemical sensors and biosensors.*, ser. Analytical techniques in the sciences. Chichester ; Hoboken, N.J. : J. Wiley, c2002., 2002, ebook.
- [54] F.-G. Banica, *Chemical sensors and biosensors: fundamentals and applications*, 1st ed. Chichester, West Sussex, United Kingdom: Wiley, 2012, ebook.
- [55] *IEEE Std Std 1139-2008. [electronic resource] : IEEE Standard Definitions of Physical Quantities for Fundamental Frequency and Time Metrology—Random Instabilities*. [S.l.] : IEEE, 2008., 2008.
- [56] R. Durst, K. Toth, D. Thevenot, and G. Wilson, “Electrochemical biosensors: recommended definitions and classification.” 1999.
- [57] International Union of Pure and Applied Chemistry, “Biosensor,” in *IUPAC Compendium of Chemical Terminology*, aCESSED??? [Online]. Available: <https://goldbook.iupac.org/html/B/B00663.html>
- [58] D. O’Hare, “Biosensors and sensor systems,” in *Body Sensor Networks.*, 2nd ed., G.-Z. Yang, Ed. The address of the publisher: London : Springer, 2014, ch. 2, pp. 55–116, ebook.
- [59] R. M. Young H. Lee, “Biosensors,” in *Sensor Technology Handbook.*, J. S. Wilson, Ed. Burlington, Mass. : Newnes, cop. 2005., 2005, ch. 1, pp. 161–180, ebook.

- [60] N. I. of Health, “Nih fact sheet point-of-care diagnostic testing,” online, accessed on 17 October 2018. [Online]. Available: <https://report.nih.gov/nihfactsheets/ViewFactSheet.aspx?csid=112>
- [61] D. B. Go, M. Z. Atashbar, Z. Ramshani, and H.-C. Chang, “Surface acoustic wave devices for chemical sensing and microfluidics: a review and perspective.” *Analytical Methods*, vol. 9, no. 28, p. 4112, 2017.
- [62] K. Länge, B. E. Rapp, and M. Rapp, “Surface acoustic wave biosensors: a review,” *Analytical and Bioanalytical Chemistry*, vol. 391, no. 5, pp. 1509–1519, 2008.
- [63] S. Hohmann, S. Kögel, Y. Brunner, B. Schmiege, C. Ewald, F. Kirschhöfer, G. Brenner-Weiß, and K. Länge, “Surface acoustic wave (saw) resonators for monitoring conditioning film formation.” *Sensors, Vol 15, Iss 5, Pp 11873-11888 (2015)*, no. 5, p. 11873, 2015.
- [64] N. Vu Hoa, P. Oliver, S. Sam, and S. Uwe, “Portable saw impedance sensor using a 1-port resonator approach.” *Proceedings*, no. 4, p. 361, 2017.
- [65] N. Shoaib, *Vector Network Analyzer (VNA) Measurements and Uncertainty Assessment. [electronic resource]*, ser. PoliTO Springer Series. Cham : Springer International Publishing : Imprint: Springer, 2017., 2017.
- [66] R. C.-H. Li, *RF Circuit Design.*, ser. Information and Communication Technology Series. Wiley, 2012, vol. 2nd ed, no. Vol. 102.
- [67] O. C. Zienkiewicz, R. L. Taylor, and J. Z. Zhu, *The finite element method. [electronic resource] : its basis and fundamentals.* Amsterdam : Elsevier, Butterworth-Heinemann, 2013.
- [68] *Introduction to COMSOL Multiphysics*, COMSOL Inc., 2017.
- [69] M. H. Madsen, N. A. Feidenhans'l, P.-E. Hansen, J. Garnaes, and K. Dirscherl, “Accounting for pdms shrinkage when replicating structures.” *JOURNAL OF MICROMECHANICS AND MICROENGINEERING*, vol. 24, no. 12, 2014.
- [70] S. Franssila, *Introduction to microfabrication*, 2nd ed. Chichester, West Sussex [England]: John Wiley & Sons, 2010, [Ebook].
- [71] *Application Notes: Lift-off*, MicroChemicals GmbH, Nicolaus-Otto-Str. 39, 89079 Ulm, [https://www.microchemicals.com/technical\\_information/lift\\_off\\_photoresist.pdf](https://www.microchemicals.com/technical_information/lift_off_photoresist.pdf).
- [72] M. J. Madou, *Fundamentals of microfabrication : the science of miniaturization.* Boca Raton : CRC Press, cop. 2002., 2002.
- [73] *Processing Guidelines Removers mr-Rem 660, mr-Rem 400 and mr-Rem 500*, micro resist technology, Köpenicker Straße 325, 12555 Berlin – Germany, 7 2013.
- [74] *Application Notes: HMDS*, MicroChemicals GmbH, Nicolaus-Otto-Str. 39, 89079 Ulm, [https://www.microchemicals.com/products/adhesion\\_promotion/hmnds.html](https://www.microchemicals.com/products/adhesion_promotion/hmnds.html).
- [75] *Technical Data Sheet AZ 5214 E Photoresist*, Merck Performance Materials GmbH, Rheingaustrasse 190 - 196,D-65203 Wiesbaden Germany, [https://www.microchemicals.com/micro/az\\_5214e.pdf](https://www.microchemicals.com/micro/az_5214e.pdf).
- [76] MicroChem, “Positive vs. negative tone photoresists,” <http://microchem.com/Prod-LithographyOverviewPosNeg.htm>, [Online] Accessed on 2019-02-04.

- [77] *Product Data Sheet: AZ 351B General Purpose Developer*, Clariant GmbH, Rheingaustrasse 190, D-65203 Wiesbaden Germany, [https://www.microchemicals.com/micro/az\\_351b\\_developer.pdf](https://www.microchemicals.com/micro/az_351b_developer.pdf).
- [78] D. M. Mattox, *Handbook of Physical Vapor Deposition (PVD) Processing.*, 2nd ed. Elsevier Science Technology Books, 2010.
- [79] *Technical Data Sheet AZ 1500 Series*, Merck Performance Materials GmbH, Rheingaustrasse 190 - 196, D-65203 Wiesbaden Germany, [https://www.microchemicals.com/micro/az\\_1500\\_series.pdf](https://www.microchemicals.com/micro/az_1500_series.pdf).
- [80] *MICROPOSIT MF CD-26 DEVELOPER*, Shipley, [http://microchem.com/products/images/uploads/MF\\_CD\\_26\\_Data\\_Sheet.pdf](http://microchem.com/products/images/uploads/MF_CD_26_Data_Sheet.pdf).
- [81] *SU-8 2000 Permanent Epoxy Negative Photoresist*, 4th ed., MicroChem, processing guidelines for: SU-8 2025, SU-8 2035, SU-8 2050 and SU-8 2075, Available: url = <http://microchem.com/pdf/SU-82000DataSheet2025thru2075Ver4.pdf>.
- [82] Y. Xia and G. M. Whitesides, "Soft lithography." *Annual Review of Materials Science*, vol. 28, no. 1, p. 153, 1998.
- [83] D. Qin, Y. Xi, and G. M. Whitesides, "Soft lithography for micro- and nanoscale patterning." *Nature Protocols*, no. 3, p. 491, 2010.
- [84] J. A. Rogers and N. Ralph G., "Recent progress in soft lithography." 2005.
- [85] L. Cademartiri and G. A. Ozin, *Concepts of nanochemistry*. Weinheim;Chichester;; Wiley-VCH, 2009.
- [86] S. Seethapathy and T. Górecki, "Review: Applications of polydimethylsiloxane in analytical chemistry: A review." *Analytica Chimica Acta*, vol. 750, no. 750th Anniversary Volume, pp. 48 – 62, 2012.
- [87] Y. Song, D. Cheng, and L. Zhao, *Microfluidics : fundamental, devices and applications*. Weinheim, Germany : Wiley-VCH, 2018., 2018.
- [88] C. S. S. R. Kumar and s. Wiley InterScience (Online, *Microfluidic Devices in Nanotechnology : Fundamental Concepts.*, ser. Microfluidic Devices in Nanotechnology. Wiley, 2010, no. Fundamental concepts.
- [89] C.-W. Tsao and D. L. DeVoe, "Bonding of thermoplastic polymer microfluidics." *Microfluidics and Nanofluidics*, no. 1, p. 1, 2009.
- [90] *SYLGARD™184 Silicone Elastomer*, The Dow Corning Chemical Company, 2017. [Online]. Available: <https://consumer.dow.com/en-us/pdp.sylgard%25e2%2584%25a2%2B184%2Bsilicone%2Belastomer%2Bkit.01064291z.html?tab=overview&id=01064291z>
- [91] K. Anwar, T. Han, and S. Kim, "Reversible sealing techniques for microdevice applications." *Sensors and Actuators, B: Chemical*, vol. 153, no. 2, pp. 301–311, 2011.
- [92] Y. Temiz, R. D. Lovchik, G. V. Kaigala, and E. Delamarche, "Review article: Lab-on-a-chip devices: How to close and plug the lab?." *Microelectronic Engineering*, vol. 132, no. Micro and Nanofabrication Breakthroughs for Electronics, MEMS and Life Sciences, pp. 156 – 175, 2015.
- [93] David C. Duffy, J. Cooper McDonald, , Olivier J. A. Schueller, and G. M. Whitesides, "Rapid Prototyping of Microfluidic Systems in Poly(dimethylsiloxane)," 1998.

- 
- [94] *Processing Guidelines – UV-PDMS KER-4690*, microresist technologies, Berlin, May 2016.
- [95] S. Satyanarayana, R. N. Karnik, and A. Majumdar, “Stamp-and-stick room-temperature bonding technique for microdevices,” *Journal of Microelectromechanical Systems*, vol. 14, no. 2, pp. 392–399, 2005.
- [96] H. Wu, B. Huang, and R. N. Zare, “Construction of microfluidic chips using polydimethylsiloxane for adhesive bonding,” *Lab on a Chip - Miniaturisation for Chemistry and Biology*, vol. 5, no. 12, pp. 1393–1398, 2005.
- [97] D. R. Appling, S. J. Anthony-Cahill, and C. K. Mathews, *Biochemistry : concepts and connections*. Harlow, England : Pearson, 2016., 2016.
- [98] M. Luckey, *Membrane structural biology: with biochemical and biophysical foundations*. New York: Cambridge University Press, 2008.
- [99] I. Gözen, *The self-spreading double bilayer : advances in lipid membrane nanotechnology.*, ser. Doktorsavhandlingar vid Chalmers tekniska högskola. Ny serie: 3494. Göteborg : Chalmers University of Technology, 2013.
- [100] A. Jesorka, N. Stepanyants, H. Zhang, B. Ortmen, B. Hakonen, and O. Orwar, “Generation of phospholipid vesicle-nanotube networks and transport of molecules therein,” *Nature Protocols*, vol. 6, no. 6, pp. 791–805, 2011.
- [101] K. Kustanovich, V. Yantchev, A. Olivefors, B. A. Doosti, T. Lobovkina, and A. Jesorka, “A high-performance lab-on-a-chip liquid sensor employing surface acoustic wave resonance: Part ii,” *Journal of Micromechanics and Microengineering*, 2018. [Online]. Available: <http://iopscience.iop.org/10.1088/1361-6439/aaf411>
- [102] B. Ali Doosti, W. Pezeshkian, D. S. Bruhn, J. H. Ipsen, H. Khandelia, G. D. M. Jeffries, and T. Lobovkina, “Membrane tubulation in lipid vesicles triggered by the local application of calcium ions,” *Langmuir*, vol. 33, no. 41, pp. 11 010–11 017, 2017, pMID: 28910109.
- [103] K. Kustanovich, V. Yantchev, B. A. Doosti, I. Gözen, and A. Jesorka, “A microfluidics-integrated impedance/surface acoustic resonance tandem sensor,” 2019, submitted manuscript.



# A

## Paper I

# A high-performance lab-on-a-chip liquid sensor employing surface acoustic wave resonance: part II

K Kustanovich<sup>✉</sup>, V Yantchev<sup>✉</sup>, A Olivefors, B Ali Doosti<sup>✉</sup>, T Lobovkina and A Jesorka

Biophysical Technology Laboratory, Department of Chemistry & Chemical Engineering, Chalmers University of Technology, Kemivägen 10, Göteborg 412 96, Sweden

E-mail: [ventsi.yantchev@gmail.com](mailto:ventsi.yantchev@gmail.com)

Received 31 July 2018, revised 18 November 2018

Accepted for publication 26 November 2018

Published 3 January 2019



## Abstract

We recently introduced an in-liquid sensing concept based on surface acoustic resonance (SAR) in a lab-on-a-chip resonant device with one electrical port. The 185 MHz one-port SAR sensor has a sensitivity comparable to other surface acoustic wave (SAW) in-liquid sensors, while offering a high quality factor ( $Q$ ) in water, low impedance, and fairly low susceptibility to viscous damping. In this work, we present significant design and performance enhancements of the original sensor presented in part I. A novel ‘lateral energy confinement’ (LEC) design is introduced, where the spatially varying reflectivity of the SAW reflectors enables strong SAW localization inside the sensing domain at resonance. An improvement in mass-sensitivity greater than 100% at resonance is achieved, while the measurement noise stays below 0.5 ppm. Sensing performance was evaluated through real-time measurements of the binding of 40 nm neutravidin-coated SiO<sub>2</sub> nanoparticles to a biotin-labeled lipid bilayer. Two complementary sensing parameters are studied, the shift of resonance frequency and the shift of conductance magnitude at resonance.

Keywords: microfluidics, surface acoustic wave, sensor, resonance, biochemical

(Some figures may appear in colour only in the online journal)

## 1. Introduction

Over the last three decades, electroacoustic (EA) and microfluidic technologies have emerged as versatile complementary components of miniaturized analytical devices. The rapid advance of the lab-on-a-chip concept (i.e. integrated sample preparation and analytical back-end) has further elevated the interest in combining these two technological fields. Lab-on-a-chip systems have several advantages over conventional laboratory techniques used in analytical chemistry and life sciences: the devices are small, low cost and often disposable, capable of multi-step automation, resulting in fast turnaround

and automation. Additionally, they make it possible to reduce the amount of reagent and sample consumption, while maintaining precise control over the environment.

In this context, small, cheap and efficient sensors capable of in-liquid operation are in great demand. The introduction of acoustic wave technology onto lab-on-a-chip platforms provides sensing capability that meets these criteria and offers an extended set of sample preparation functions to be implemented, such as fast fluidic actuation, contact-free particle manipulation, and sorting.

The majority of acoustic-wave biochemical sensors have to be immersed in aqueous solutions in order to deliver the analyte to the sensing surface in a compatible fluid environment. Acoustic sensors that are commonly used in gas-chemical and biochemical applications typically rely on gravimetric analysis—one of the most explored sensing concepts in chemical



Original content from this work may be used under the terms of the [Creative Commons Attribution 3.0 licence](https://creativecommons.org/licenses/by/3.0/). Any further distribution of this work must maintain attribution to the author(s) and the title of the work, journal citation and DOI.

analysis. In this context, an essential requirement on the sensor is that it preserves its functionality when immersed in fluid and reliably detects mass changes due to a specific (bio)chemical reaction on the sensing surface. To supply and confine the analyte to the sensing area and at the same time protect these devices from the liquid environment, a soft polymer microfluidic delivery system is often used [1].

Significant efforts in the field of microfluidics-integrated sensing technology have focused on the development of highly sensitive, label-free, real-time devices based on the thin-film EA technology. Microsystems based on this approach have a particularly strong potential for commercialization, enabled by the fabrication technologies established by the radio frequency (RF) filter industry. Thickness-excited quasi-shear film bulk acoustic resonators (shear-FBARs) have shown the best performance so far [2, 3]. This is currently the only device type that has reached the stage of commercial prototypes. Thin-film S<sub>0</sub>-Lamb waves and their equivalent extensional plate modes have also shown to be promising, since they also rely on the technology originally developed for commercial RF filter manufacturing [4]. However, these approaches are limited by practical considerations concerning process uniformity, device fragility, strong local pressure and temperature sensitivity [3].

So far, the majority of surface acoustic wave (SAW) devices has been used in the telecommunication industries for RF filtering and signal processing applications, but SAW technology is gaining more and more attention in the microfluidics community. Recent research has already demonstrated that SAW technology provides an effective means of controlling, sensing and actuating particles and fluids in lab-on-a-chip systems [1]. Thus, this platform concept is generating increasing attention, and much effort has been put forward to bring the technology to commercial viability, mainly aiming at applications in medical diagnostics.

SAW-based sensors mostly rely on delay-line configurations where the SAW propagates through a comparatively long distance between input and output transducers to accumulate sufficient time delay and phase shift [5, 6]. However, for in-liquid operation, SAW delay line biosensors are characterized by strong signal loss in transmission, and relatively large size. To address these issues, a two-port SAW resonator with smaller distance between the transducers was introduced as an alternative to the delay line concept [7]. Despite all the benefits provided by this approach, the two-port configuration is somewhat problematic when parallelization needs to be considered. For that reason, one-port sensor systems have been developed.

We have earlier proposed the concept of surface acoustic resonance (SAR) by constructing a proof of principle microfluidic sensor in one-port configuration (Part I) [8]. In this work, the reflective gratings of a one-port SAW resonator are employed as mass loading-sensing elements, with the SAW transducer being protected from the measurement environment and acting only as a read-out element. The concept of separate driving and sensing units was for the first time implemented in SAW sensor technology.

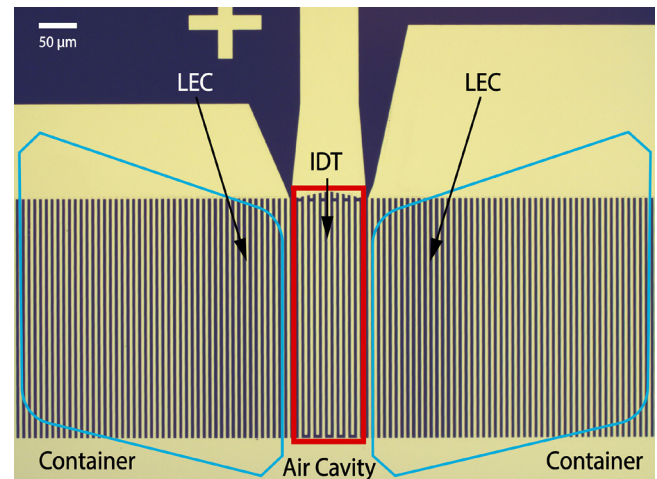


**Figure 1.** SAR sensor employing lateral energy confinement, placed at the bottom of the liquid containers (blue outlines). The outline of the air cavity above the IDT is depicted in red. The LEC regions are highlighted.

Here, we redesigned the topology of the sensor and introduced a ‘lateral energy confinement’ (LEC) to our sensor, enhancing the device sensitivity to approach closer the theoretical limit of the shear SAW. The newly designed sensors are characterized in time-resolved measurements and compared to the proof-of-principle design presented in part I. The microfabrication process remained unchanged; it has been previously presented [8] and is not further elaborated here.

## 2. The ‘LEC’ concept

The enhanced SAR sensor employs the reflective gratings of the one-port SAW resonator as sensing elements, while the transducer is a wide-band interdigital transducer (IDT), placed in-between the reflectors and protected from the liquid by an air cavity. The sensitivity of the SAW resonance is determined primarily by the changes in SAW propagation when propagating under the reflective gratings subjected to viscoelastic load. In our original SAR sensor design (Part I) the SAW energy is being gradually reflected back to the IDT, thus promoting strong SAW localization under the IDT, while outside the transducer the SAW displacement is exponentially decaying. This effect itself is limiting the device sensitivity, since it is determined by the ratio between the kinetic energy at the sensing surface and the total kinetic energy in the system [9]. Typically, an improvement in SAW sensitivity results from better LEC confinement of SAW energy near the surface, achieved through slowing down the wave [8, 10].

We now address the sensitivity limitation imposed by the decaying nature of the SAW inside the sensing area, i.e. reflectors, by introducing a lateral SAW localization through a specially designed SAW energy confinement topology. The concept of the ‘LEC’ design is shown as fabricated in figure 1. It utilizes the same material stack and grating pitch as in our earlier conceptual design presented in Part I [8]. Here, a variation of grating reflectivity is introduced to confine a larger amount of SAW energy in the sensing containers. We establish

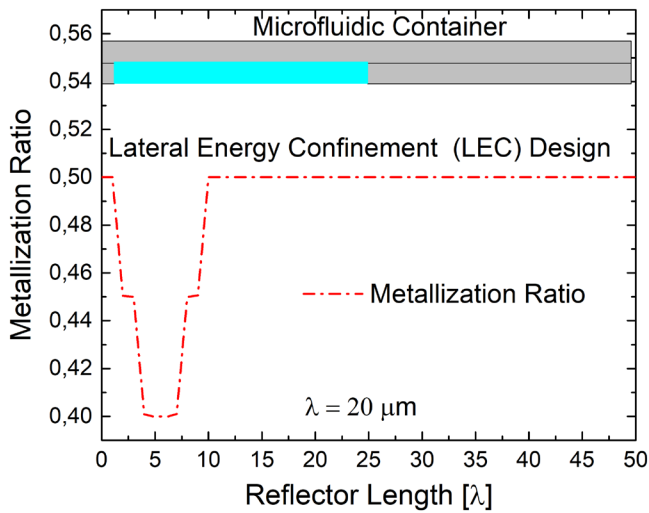


**Figure 2.** Lateral modulation of the mark-to-pitch ratio of the grating strip defining the acoustic wave confinement regions. The top section of the image shows schematically the position of the polymer part of the device, with the light blue part being the liquid-filled container.

a domain of reduced reflectivity just beside the IDT that enables significant amount of SAW energy to be concentrated in the sensing domain at resonance. The reduction of grating reflectivity is achieved through an area characterized by narrower grating strips, i.e. strips with a smaller mark-to-pitch ratio. In figure 2 the specific variation of the mark-to-pitch ratio is shown. In the earlier SAR sensor design, the mark-to-pitch ratio was  $m = 0.5$  for all strips in the reflector grating, while here it narrows locally to  $m = 0.4$  forming two energy localization domains centered at about 5 wavelengths from the IDT ends. The IDT consists of 7 pairs of electrodes for wideband operation, while the device aperture is  $20\lambda$ , with  $\lambda = 20 \mu\text{m}$  at resonance.

A 2D COMSOL Multiphysics® (Version 5.3) frequency response analysis of the proposed SAR device was performed to verify and reveal the fundamentals of the LEC performance. In figure 3, the transversal shear displacement distributions are shown as simulated at resonance for three different designs of the LEC topology. All designs follow the scheme in figure 2 with the difference in the minimum metallization ratio inside the LEC zone, while the smooth acoustic impedance transition to it is provided by two pairs of grating strips with their metallization ratios derived as the mean value of the minimum and maximum metallization ratios.

The applied design scheme promotes energy confinement at the sensing surface within the containers. Lower minimum metallization ratios in the LEC domain ensure greater SAW confinement in the sensing area at the expense of coupling between the IDT and the SAW. The SAR sensor concept relies on both the ability of the IDT to probe sensitivity of the reflector gratings and the ability of the IDT to introduce sufficient energy into the sensing domain. In fact, there has to be a fine balance between these two requirements. For example, a SAR sensor with a very long IDT will have most of its energy under the IDT, and will not be able to sense outside of it. On the other hand, if energy confinement in the reflectors is too

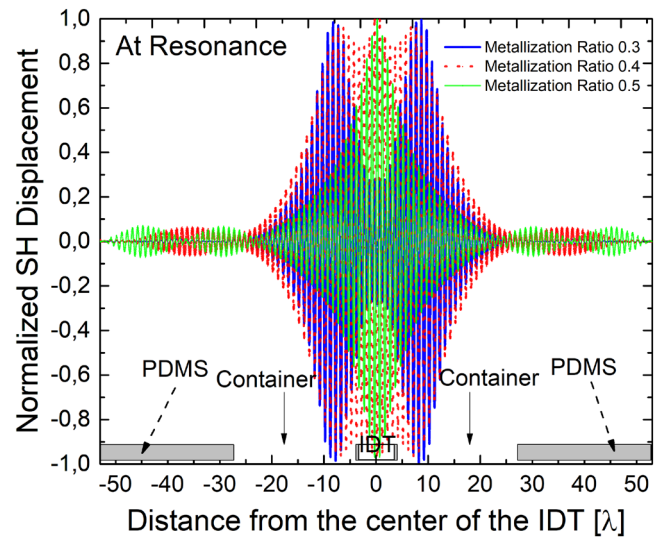


**Figure 3.** Normalized SH-SAW displacement distributions at resonance. The bottom part shows the positions of the microfluidic chip cavities above IDT and reflectors. At  $m = 0.5$ , there is no energy localization. At  $m = 0.4$ , energy localization in containers can be observed, while IDT remains strongly coupled with the system. At  $m = 0.3$ , most of energy is localized in containers, while IDT decouples from the system as can be observed from a low amplitude region next to it.

strong, most of the SAW energy will remain there, and as a result decouple from the IDT. Accordingly, in both extreme cases either the sensitivity or the electrical response of the device become poor.

To further study the optimal LEC design we simulated sensitivity and magnitude of the device response as a function of energy localization in the LEC domain. The sensor response was studied by applying a mass load over the container region of the resonator. We have used shell elements in COMSOL to introduce this mass load as a boundary condition. In figure 4, normalized sensitivity and normalized magnitude of conductance are shown in a comparative manner for the LEC domains with a varying minimum metallization ratio. As expected, the device sensitivity exhibits a maximum determined by the trade-off between the energy confinement in the sensing domain and the IDT coupling to the SAW at resonance. Below a metallization ratio of 0.4, the IDT coupling rapidly decreases, which in turn determines its poorer probing abilities and thus reduced device sensitivity.

By contrast, at antiresonance the energy is confined predominantly under the IDT in all LEC designs, while the SAW amplitude is decaying along the reflector grating (figure 5).

Both modes of operation were compared experimentally with respect to their sensitivity. In figure 6 the conductance around resonance, and the resistance around antiresonance are shown as measured in air and water. The resonance frequency is approximately 188 MHz. A frequency shift of the conductance peak of about  $-2200 \text{ ppm}$  is observed as a result of water loading, accompanied by a 27% decrease of the conductance peak magnitude. Note that the sensitivities demonstrated at resonance in the original design (Part I) were  $-915 \text{ ppm}$  and  $-5\%$ , respectively, while the maximum sensitivity was theoretically estimated to be about  $-2100 \text{ ppm}$  [8].

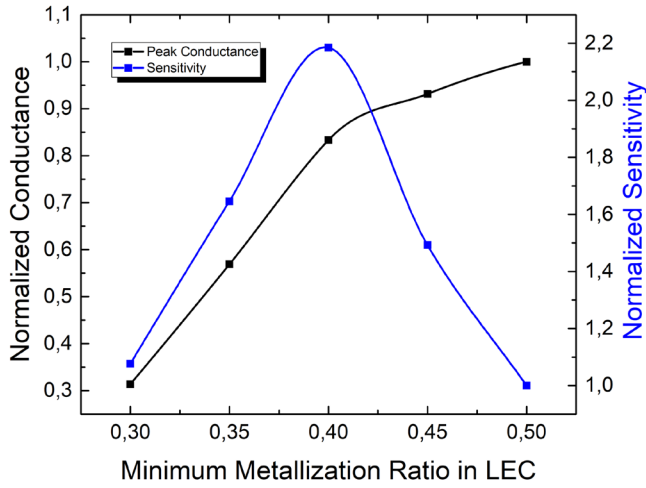


**Figure 4.** Normalized conductance and sensitivity at different metallization ratios.

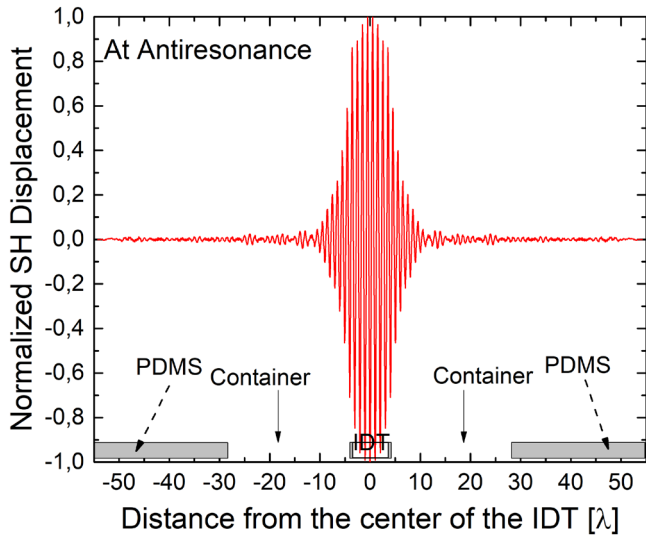


**Figure 5.** Normalized SH-SAW displacement distribution at antiresonance for  $m = 0.4$ . The bottom part shows the positions of the microfluidic chip cavities above IDT and reflectors.

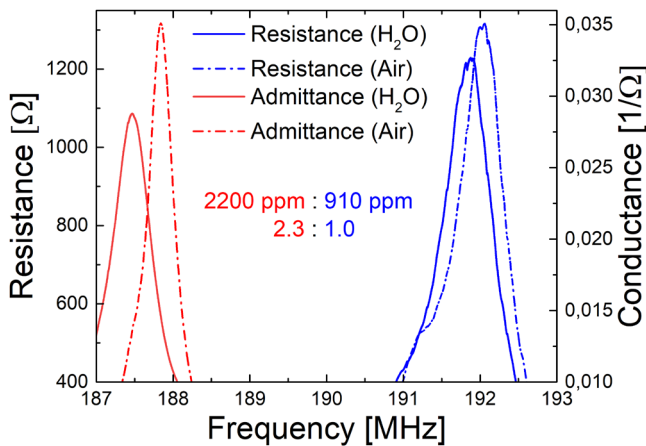


**Figure 6.** SAR sensor performance under water load. Admittance and Resistance are depicted in red and blue, respectively. Dashed lines represent water samples, and solid lines air samples for comparison.

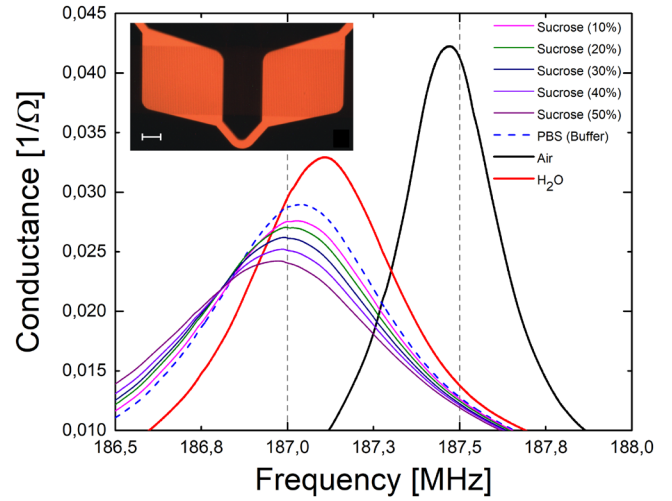


**Figure 7.** SAR sensor performance under viscous load. The colored graphs represent the signals of different sucrose solution loads, the dashed line belongs to the buffer reference (0% sucrose), and the black line is the signal of the empty containers. The inset shows a fluorescence micrograph of the microfluidic chambers and flow channels, loaded with fluorescent nanoparticles. The scale bar represents  $100 \mu\text{m}$ .

**Table 1.** Table of sensor sensitivity under various loads.

Sensor load	Original (part I)	Improved
Air to water	-915 ppm	-2200 ppm
Water to PBS	-160 ppm	-315 ppm
PBS to 20% Sucr.	-160 ppm	-220 ppm
PBS to 40% Sucr.	-260 ppm	-600 ppm
PBS to 50% Sucr.	-450 ppm	-960 ppm

The difference in the measured sensitivities between the original design (Part I) and the LEC design is in excellent agreement with theoretical predictions. Accordingly, the optimized LEC design enables a significant improvement in device sensitivity.

At antiresonance the observed frequency shift of the resistance peak of about  $-910 \text{ ppm}$  determines a sensitivity which is 2.3 times smaller than the sensitivity of the resonance. This again demonstrates the impact of the energy distribution on the device sensitivity.

### 3. Results and discussion

#### 3.1. In-liquid sensor characterization

The SAR sensor has been characterized in an environment with a varying (viscosity  $\times$  density) product ( $\rho\eta$ ) using the Planar 304/1 (Copper Mountain Technologies, USA) vector network analyzer with a set of measurement probes (Picoprobe, Model 40A, GGB Industries Inc., USA). Sucrose solutions of up to 50% content in phosphate buffer saline (PBS) have been evaluated (figure 7). The SAR sensor tolerates the viscous damping well, exhibiting about 17% decrease in conductance peak magnitude for Sucrose-PBS solutions of up to 50%. The observed attenuation is about three times higher than that of the original design (Part I) [8], which is related to the increase

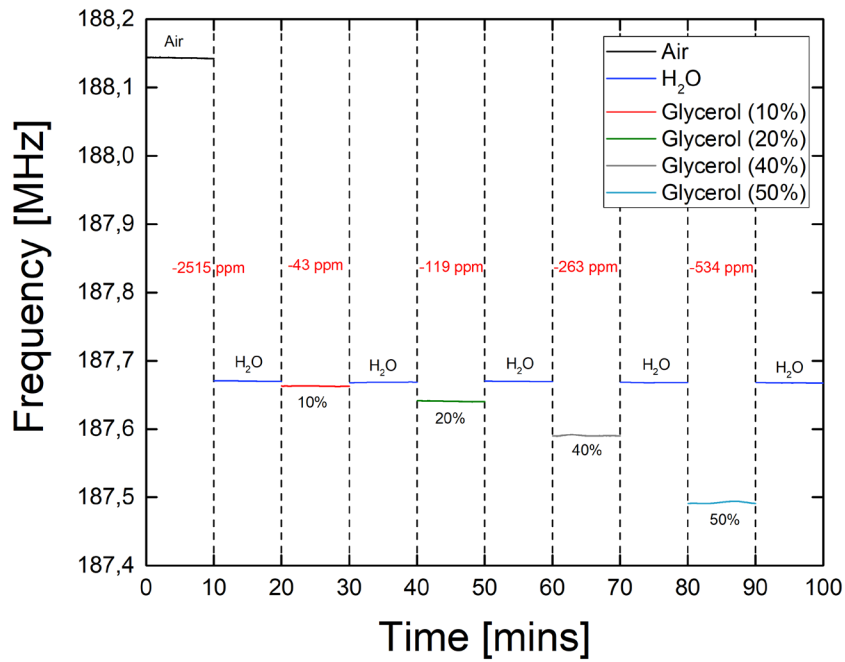


**Figure 8.** Time-resolved response of the SAR sensor under viscous load. The colors encode the signals for air (grey), water (blue) and sucrose loads of different concentrations. Frequency shifts per time step are indicated in red.

in sensitivity demonstrated by the new design. Note that the attenuation is still within acceptable limits, low impedance at resonance is retained. In table 1 the demonstrated frequency sensitivity is presented as compared to the original SAR design (Part I) [8]. An overall two-fold increase in sensitivity is apparent.

These results can be readily compared to the state-of-art in-liquid sensors. The response of the 187 MHz SAR sensor at 40% sucrose corresponds to a square root of the viscosity  $\times$  density product  $(\rho\eta)^{0.5}$  of about 2.3 times the value of PBS ( $\sim 1 \text{ kg} \times \text{m}^{-2} \text{ s}^{-0.5}$ ). For such a variation, a 900 MHz FBAR has demonstrated the same sensitivity of about  $-600 \text{ ppm}$  [11]. The improved SAR sensor design demonstrates a sensitivity comparable to FBAR at an almost 5 times lower frequency. It is noted that the shear wave sensitivity scales with the square root of the operating frequency. On the other hand, the noise levels also increase with frequency, which has an impact on sensor resolution. In addition, high frequency devices are much more susceptible to parasitic effects and instabilities [12].

A SAW delay line, operating at 100 MHz, has demonstrated a frequency shift of about  $-500 \text{ ppm}$ , corresponding to a change of  $(\rho\eta)^{0.5}$  from 1 to 4.35 [13]. The measured 187 MHz SAR sensor response for the same change is about  $-960 \text{ ppm}$  (50% Sucrose solution), which is significantly larger than the effect of frequency scaling ( $f^{0.5} \sim 1.37$  times).

Time-resolved measurements were performed to investigate the sensor recovery and the measurement noise. In figure 8, measurement results of different concentrations of glycerol in water are presented. In this set of measurements, water is used to establish the base sensor response level after each individual measurement of glycerol solution. The results show that, when water is introduced to the sensor containers, the resonant frequency recovers repeatedly to the initial value,

providing a stable baseline. When the sensor is exposed to glycerol solutions, the resonant frequency decreases to a concentration-dependent value, which remains unchanged over the measurement window, indicating sufficient stability of the SAR sensor for practical purposes.

The noise level was calculated using averaging of the Allan deviation  $\sigma$  over 10 min. Each  $\sigma$  was derived from 200 subsequent measurements at 3 s intervals with the VNA at 3 dBm input power. The measured conductances were fitted near resonance to a 5th order polynomial, and the resonance frequencies were subsequently extracted from the polynomial fit of each measurement. Noise levels under load were determined over 10 min to be below 0.5 ppm for resonance frequencies, and below 10 ppm for the conductance peak. This number determines the limit of frequency detection ( $3\sigma < 1.5 \text{ ppm}$ ) and the limit of conductance magnitude detection ( $3\sigma < 30 \text{ ppm}$ ). Further improvement in the limit of frequency detection is possible through an increase of the input power of the VNA used in the measurements, and through ensuring better thermal stability of the physical measurement environment. We also note that despite being from the same batch/wafer, each individual chip has tolerances within a few percent of the nominal value due to a technological drift. These drifts usually exist between different devices and are readily compensated by calibration routines.

### 3.2. Biochemical sensing

For further characterization of the SAR sensor we performed sensing of lipid film-nanoparticle-interactions, using a protocol similar to the one established in part I (figure 9) [8]. We deposited, in a two-step experiment using a microfluidic chamber at 21 °C, a biotin-modified supported lipid bilayer (SLB) over the reflector areas, followed by neutravidin-coated

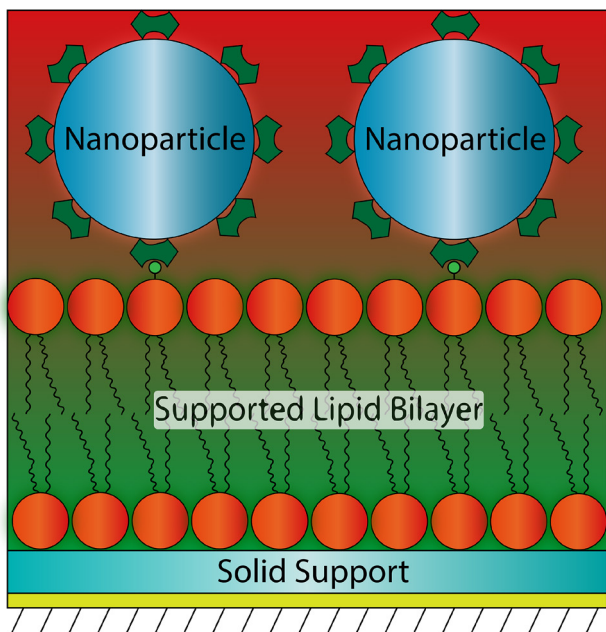


**Figure 9.** Schematic representation (not to scale) of the molecular interactions employed in the neutravidin-biotin-based nanoparticle-lipid bilayer assay. The protein-coated nanoparticles establish an affinity-based association with biotinylated lipids present at 5% (w/w) in the bilayer. Note that the neutravidin has four binding sites for biotin. The solid support is the silicon dioxide top coating of the SAR sensor surface.

nanoparticles (NPs). The SLB membrane is formed in the first step by wetting of the surface with lipid material originating from a multilamellar vesicle (MLV) suspension loaded into the microfluidic containers [8]. Following a washing step, the neutravidin-coated nanoparticles in aqueous suspension are pumped through the chamber across the deposited SLB. NPs bind in this step by an affinity reaction to the biotinylated SLB. We measured over time the change of resonance frequency as well as the change in the amplitude of the conductance at resonance for each step in the deposition experiment (figure 10).

The observed responses are showing the same trends as the measurements of the same system with the sensor design presented in part I. They confirm that frequency and magnitude of conductance can be used as independent complementary parameters of SAR sensor systems. More specifically, the SLB loading results in downshifts in frequency and conductance peak magnitude, while NP loading results in frequency downshift and conductance peak magnitude upshift. Accordingly, SLB deposition represents a mass loading with effect on the viscoelastic properties of the sensor surface, while the reaction with NP contributes to increased rigidity of the bio-layer, as indicated by the increased magnitude of conductance peak.

The measured response of the newly designed SAR sensor shows significantly improved sensitivity compared to the device presented in part I [8]. In table 2 a detailed comparison of the mass sensitivities of both devices is presented. The short-time response (seconds rather than minutes) of the new sensor to changes in loading can potentially also reveal additional information about the involved binding processes and will be investigated in a separate study.

**Table 2.** Comparison of mass sensitivities for different SAR devices.

Design: parameters:	Original (part I) freq./conduct.	Improved freq./conduct.
Air to water	-915 ppm/-5%	-2200 ppm/-27%
Water to buffer	-160 ppm/-1%	-315 ppm/-2%
Water to SLB	-65 ppm/0%	-130 ppm/-2%
SLB to SLB/NPs	-90 ppm/+2%	-160 ppm/+2%

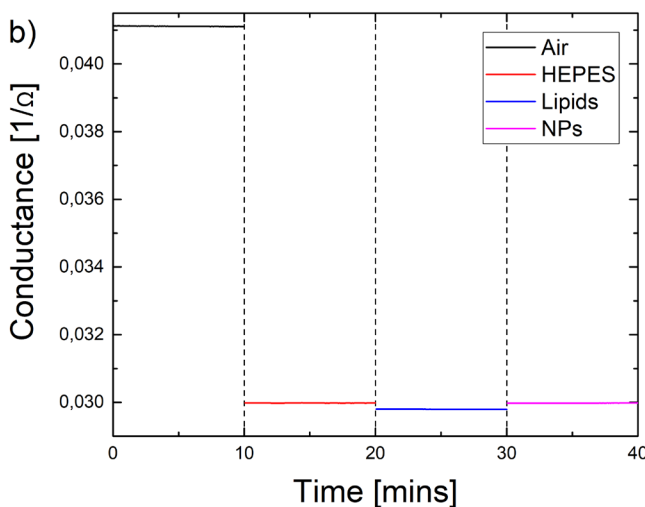
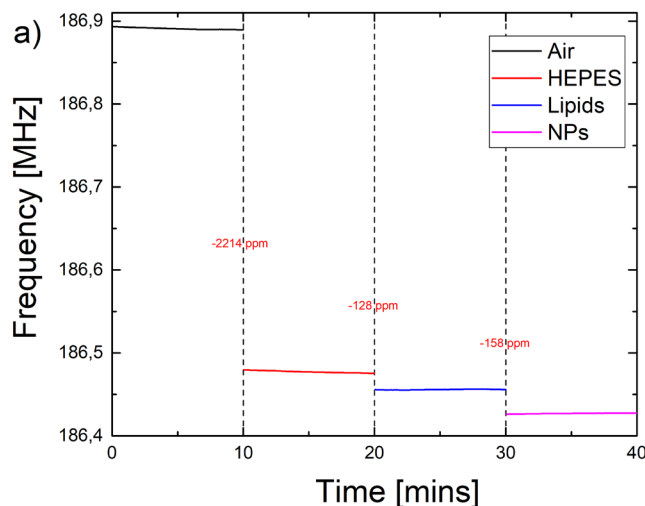


**Figure 10.** Time-resolved response of the SAR sensor subjected to the SLB deposition/affinity reaction sequence; (a) frequency shift (b) peak conductance magnitude shift.

### 3.3. Sensing of SLB transformations

Divalent calcium cations ( $Ca^{2+}$ ) are known to bind to negatively charged phospholipids, such as phosphatidylserine [14], and lead to a tighter packing of molecular lipid films, dehydration of lipids, as well as conformational changes to the lipid headgroups [15]. Generally, the fluidity of the membrane is to some extent reduced. Recent research has also shown that local exposure of lipid membranes in the low-tension regime (excess lipid material) to calcium ion concentrations in the arrange of 1–5 mM leads to a partial transformation of the planar membranes to

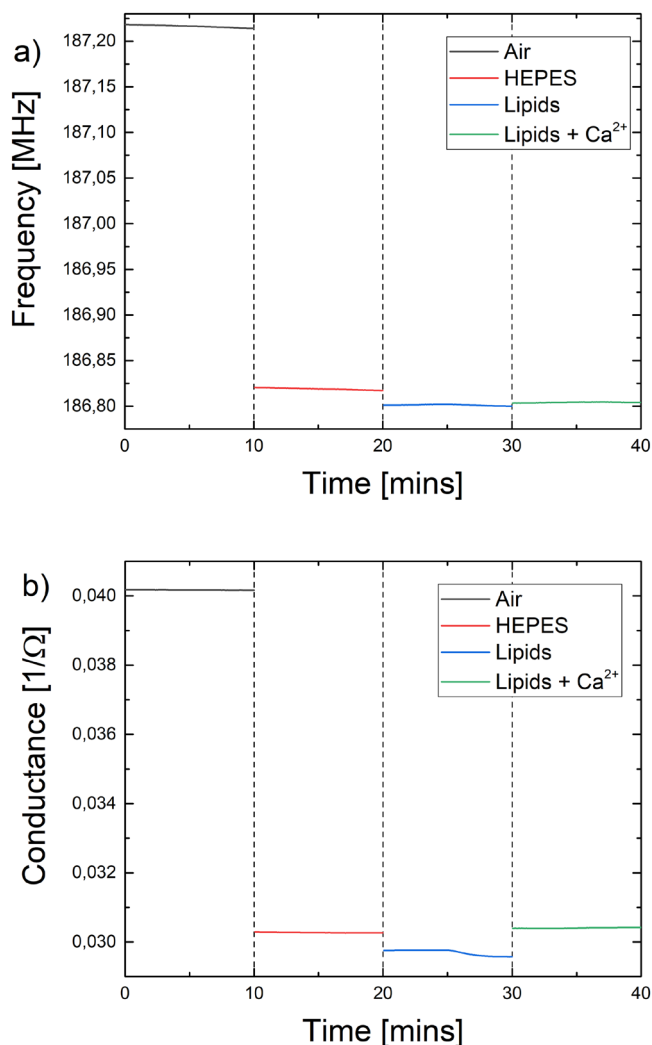


**Figure 11.** Time-resolved response of the SAR sensor subjected to a SLB reaction with  $\text{Ca}^{2+}$ ; (a) frequency shift (b) peak conductance magnitude shift.

nanotubular structures that extend into the aqueous medium but remain attached to the membrane [16]. This transformation, when it occurs on a surface-supported membrane, would effectively lead to a transfer of lipid material from an adhered surface film into the aqueous space above it, where parts of the lipid material float close to the membrane in a loosely connected regime. This should decrease the effective loading, owing to the 40 nm decaying length of the 180 MHz SH-SAW, resulting in a measurable increase in resonance frequency.

For our sensor, the 5 mM  $\text{Ca}^{2+}$  exposure of the SLB is accompanied by a frequency upshift of about 23 ppm, and a simultaneous conductance peak upshift of about 3% (figure 11). We attribute the upshift of both quantities to the above mentioned slightly reduced mass load, but also to increased rigidity of the calcium-rich SLB layer. The comparatively small frequency up-shift can be associated with the slight expected decrease in effective mass loading, while we attribute the up-shift in conductance peak magnitude to decreased losses, i.e. with layer rigidity. At this point we do not have any additional experimental data to verify this hypothetical mechanism, but our measurements provide evidence that the SAR sensor can be potentially useful for the characterization

of transformations of lipid membranes. Note that the length of the tubular protrusions depends on the availability of excess membrane material [16, 17], and can range from a few nanometers to several micrometers. In our case we estimate the range to be only within several tens of nm, as large lipid reservoirs are not available. The deposition of small multilamellar vesicles onto the surface in the first step may, however, provide sufficient excess lipid material to establish the low-tension regime required for tubulation to occur. This can in the future be verified by means of other film deposition methods, which would either lead to a high membrane tension and prevent the formation of tubes, or supply larger quantities of lipids in the form of large or giant multilamellar (onion shell) vesicles.

#### 4. Future trends in SAR sensor design

The design of SAR sensor can further be optimized in view of reducing the temperature sensitivity as well as integration with other functionalities. Here we discuss some straightforward approaches emanating from the specific SAR design.

We measured the temperature coefficient of the resonance frequency to be  $-83 \text{ ppm K}^{-1}$ , while the antiresonance frequency demonstrated a temperature dependence of about  $-72 \text{ ppm K}^{-1}$ . These numbers are typical for the  $\text{LiNbO}_3$  substrate and need to be reduced to improve upon the limit of quantification/detection. It is expected that reducing the temperature coefficient of frequency (TCF) will lead to a further significant reduction in measurement uncertainties. One simple way to achieve this would potentially be the subtraction of resonance from antiresonance frequencies. They exhibit close similarities in thermal response, while the difference in mass-sensitivity is remarkably large. Signal subtraction reduces the thermal sensitivity to  $-11 \text{ ppm K}^{-1}$ , while retaining a significant mass sensitivity. In a measurement environment with 0.1 K temperature tolerance, this translates in to a maximum  $-1.1 \text{ ppm}$  frequency shift, which is comparable to the noise level. More elaborate frequency subtraction techniques can readily eliminate the first order TCF in the sensor response.

Alternatively, the compensation of the thermal drift can be achieved by adding a  $\text{SiO}_2$  layer of about  $0.3\lambda$  thickness [18]. This technique has the additional advantage to electrically decouple the electrodes from the liquid and thus enable a robust SAR sensor design, where the IDT does not need to be separated from the liquid environment by a cavity. Theoretical estimations show that the effect of electrical short-circuiting on the surface of the SAR grating is a frequency downshift of about  $-1000 \text{ ppm}$ , while short-circuiting of the surface of the  $0.3\lambda$  thick  $\text{SiO}_2/\text{Au}$  strips/ $\text{LiNbO}_3$  composite is expected to induce a change of less than 0.3 ppm. Accordingly, SAR sensors with either an electrically screened or open-circuit top surface can be produced without any sacrifice in device performance, while enabling efficient compensation of the SAR thermal drift, and simplifying the microfluidic circuitry.

Last but not least, the new sensor design includes the capability for simultaneous low frequency ( $<1 \text{ MHz}$ ) electrochemical impedance spectroscopy (EIS). On-chip EIS employs the reflector strips in interdigitated split electrode geometry (figure 12). The split electrode topology of the

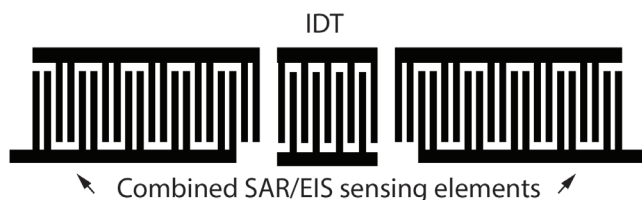


**Figure 12.** Schematic drawing of a suggested electrode configuration for an integrated SAR/EIS sensor.

reflectors is specifically suitable, since the SH-SAW experiences it as a short-circuited grating. Specifically, two neighboring electrodes distributed within a wavelength are connected electrically, therefore the SH-SAW does not induce potential over a pair of connected electrodes at resonance. Moreover, the EIS operates at a frequency where acoustic waves are not excited, thus both functionalities, i.e. acoustic sensing and EIS sensing, can be operated independently. Interdigitated electrodes are a common configuration in EIS sensing [19]. A proposed integration of EIS with SAR device is schematically shown in figure 12.

## 5. Conclusions

A ‘LEC’ design concept for a SAR in-liquid sensor has been demonstrated and its performance experimentally characterized. The acoustic wave confinement led to a sensitivity increase of >100%, which was determined by loading the sensor with a series of solutions of different  $\rho\eta$ . Time-resolved measurements of the sensor response confirmed stable operation with a limit of frequency detection of  $3\sigma < 1.5$  ppm, and the limit of conductance magnitude detection to be below 30 ppm. At anti-resonance, the SAW is strongly localized under the IDT, and exhibits a 2.3 times smaller mass-sensitivity as compared to resonance, while exhibiting similar thermal drift. This can be utilized for further improvement of the noise characteristics by canceling out thermal fluctuations in the measurement.

A microfluidics-enabled biomembrane-nanoparticle assay was further used to demonstrate that the sensor is capable of following multi-step bioaffinity processes in sample volumes of  $\sim 10 \mu\text{l}$ . In the context of 2D fluidic molecular films as sensing layer, the combined evaluation of frequency and conductance can reveal details about structural changes in the sensing layer, as shown for the  $\text{Ca}^{2+}$ -induced transformation of the sensor-surface-supported lipid membrane.

## Acknowledgments

We acknowledge the European Union (Horizon 2020 FET Open research grant, Project ID: 664786) and the Swedish Strategic Research Foundation (SSF).

## ORCID iDs

K Kustanovich  <https://orcid.org/0000-0002-7762-7157>  
 V Yantchev  <https://orcid.org/0000-0002-2696-1649>  
 B Ali Doosti  <https://orcid.org/0000-0001-9149-0751>

## References

- [1] Go D B, Atashbar M Z, Ramshani Z and Chang H C 2017 Surface acoustic wave devices for chemical sensing and microfluidics: a review and perspective *Anal. Methods* **9** 4112–34
- [2] Wingqvist G, Bjurström J, Liljeholm L, Yantchev V and Katardjiev I 2007 Shear mode AlN thin film electro-acoustic resonant sensor operation in viscous media *Sensors Actuators B* **123** 466–73
- [3] Katardjiev I and Yantchev V 2012 Recent developments in thin film electro-acoustic technology for biosensor applications *Vacuum* **86** 520–31
- [4] Mirea T, Yantchev V, Olivares J and Iborra E 2016 Influence of liquid properties on the performance of S-0-mode Lamb wave sensors II: experimental validation *Sensors Actuators B* **229** 331–7
- [5] Gizeli E 2000 Study of the sensitivity of the acoustic waveguide sensor *Anal. Chem.* **72** 5967–72
- [6] Kondoh J 2013 A liquid-phase sensor using shear horizontal surface acoustic wave devices *Electr. Commun. Japan* **96** 41–9
- [7] Hohmann S, Kogel S, Brunner Y, Schmiege B, Ewald C, Kirschhofer F, Brenner-Weiss G and Lange K 2015 Surface acoustic wave (SAW) resonators for monitoring conditioning film formation *Sensors* **15** 11873–88
- [8] Kustanovich K, Yantchev V, Kirejev V, Jeffries G D M, Lobovkina T and Jesorka A 2017 A high-performance lab-on-a-chip liquid sensor employing surface acoustic wave resonance *J. Micromech. Microeng.* **27** 114002
- [9] Wingqvist G, Yantchev V and Katardjiev I 2008 Mass sensitivity of multilayer thin film resonant BAW sensors *Sensors Actuators A* **148** 88–95
- [10] Assouar M B, Kirsch P and Alnot P 2009 New Love wave liquid sensor operating at 2 GHz using an integrated micro-flow channel *Meas. Sci. Technol.* **20** 095203
- [11] Mirea T, Iborra E and Yantchev V 2016 S-0 Lamb wave resonators for in-liquid sensing: promising alternative to shear bulk acoustic wave devices 2016 *European Frequency and Time Forum (EFTF)* (<https://doi.org/10.1109/EFTF.2016.7477807>)
- [12] Vig J R 1991 On acoustic sensor sensitivity *IEEE Trans. Ultrason. Ferroelectr. Freq. Control* **38** 311
- [13] Morita T, Sugimoto M and Kondoh J 2009 Measurements of standard-viscosity liquids using shear horizontal surface acoustic wave sensors *Japan. J. Appl. Phys.* **48** 07GG15
- [14] Sinn C G, Antonietti M and Dimova R 2006 Binding of calcium to phosphatidylcholine-phosphatidylserine membranes *Colloid Surf. A* **282** 410–9
- [15] Melcrova A, Pokorna S, Pullanchery S, Kohagen M, Jurkiewicz P, Hof M, Jungwirth P, Cremer P S and Cwiklik L 2016 The complex nature of calcium cation interactions with phospholipid bilayers *Sci. Rep.* **6** 38035
- [16] Ali Doosti B, Pezeshkian W, Bruhn D S, Ipsen J H, Khandelia H, Jeffries G D M and Lobovkina T 2017 Membrane tubulation in lipid vesicles triggered by the local application of calcium ions *Langmuir* **33** 11010–7
- [17] Gozen I, Billerit C, Dommersnes P, Jesorka A and Orwar O 2011 Calcium-ion-controlled nanoparticle-induced tubulation in supported flat phospholipid vesicles *Soft Matter* **7** 9706–13
- [18] Matsuda S, Miura M, Matsuda T, Ueda M, Satoh Y and Hashimoto K-Y 2010 Investigation of  $\text{SiO}_2$  film properties for zero temperature coefficient of frequency SAW devices 2010 *IEEE Int. Ultrasonics Symp.* pp 633–6
- [19] Lisdat F and Schafer D 2008 The use of electrochemical impedance spectroscopy for biosensing *Anal. Bioanal. Chem.* **391** 1555–67